UNIVERSITY OF CALGARY

Cantilever Effective Tip Radius Estimation through Contact Resonance Atomic Force Microscopy

by

Thomas Mathias

A THESIS

SUBMITTED TO THE FACULTY OF GRADUATE STUDIES

IN PARTIAL FULFILLMENT OF THE REQUIREMENTS FOR THE

DEGREE OF MASTER OF SCIENCE

GRADUATE PROGRAM IN MECHANICAL ENGINEERING

CALGARY, ALBERTA

August, 2023

© Thomas Mathias 2023

Abstract

The mechanical characteristics of materials, particularly those of composite materials, can be mapped spatially and quantified using Contact Resonance Atomic Force Microscopy (CR-AFM). This technique operates by measuring the changes in resonance frequency as an AFM cantilever tip comes into contact with a sample surface. Such frequency shifts are primarily related to contact stiffness, although it can also influence other factors such as viscoelasticity. While several theories aim to connect the modal shape and resonant frequency of the AFM cantilever with contact stiffness, no direct application of these models has been developed to directly transform the resonant frequency into a physical mechanical property measurement. Instead, the majority of experimental studies utilising CR-AFM calibrate the frequency conversion factor relating to contact stiffness using a known reference sample, bypassing the direct use of these cantilever models.

This thesis brings into focus two novel aspects aimed at enhancing and refining the CR-AFM technique: using thermal resonance to monitor the oscillation modes of an AFM cantilever during an experiment and establishing a connection between cantilever dynamics theory and the calibration of CR-AFM data that eliminates the requirement for normalisation to a known sample.

In the first segment of this thesis, cantilever thermal displacement time series data is transformed into frequency space utilising the short-time Fourier transform (STFT) and continuous wavelet transform (CWT). It will be demonstrated that only the STFT calculations are capable of delivering the time-frequency resolution necessary to track AFM modal vibrations, at least currently. The application of the STFT allows for real-time tracking of the contact resonance frequency and Quality factor throughout a force spectroscopy experiment. The ensuing analysis reveals the fluctuations in contact resonance frequency over the course of this experiment.

However, utilising cantilever analytical models to interpret this data using known contact mechanics models resulted in nonphysical estimates. Further studies are underway to reconcile the often problematic assumptions made in contact mechanics for AFM measurements with dynamic, STFT measurements. The experimental findings underscore the reasons why normalisation or calibration of CR-AFM results to samples with known stiffness has been prevalent until now. Despite progress, the comprehensive understanding of the contact mechanics and vibration theory necessary to analyse the dynamics of AFM cantilevers in such experiments remains an open challenge.

Preface

Thank you for taking the time to read over my master thesis entitled "Cantilever Tip Radius Estimation through Contact Resonance Atomic Force Microscopy". This thesis has been written in accordance with the requirements of the Master of Science program in the Mechanical & Manufacturing Engineering department at the University of Calgary. The research and writing of this thesis has been ongoing since the start of my program in September 2021.

Through my master program, I have acquired many new skills and learned lessons that I did not see before starting. I have learnt some of the many skills required to operate and maintain several Atomic Force Microscopes (AFM) along with understanding the physical principles key to their function and use. The acquisition, analysis, and display of data have greatly improved my programming and software skills, particularly with the AFM software along with the programs MATLAB and LabVIEW. Lastly, I have had the great opportunity to present my research at several prestigious and highly regarded research conferences. This includes the internal University of Calgary graduate research seminar along with the 24th Wear of Materials and the 77th Society of Tribological and Lubrication Engineers (STLE) research conference in 2023. The relationships and professional development gained from these conferences has been an amazing experience and definitely some of the highlights of my program.

Acknowledgments

I would like to thank my research supervisor Professor Dr. Philip Egberts for the guidance and help throughout my program. The lessons along with development I have received from Dr. Egberts have been invaluable, and I will incorporate these learnings in future opportunities. I also want to acknowledge the other students and researchers in the Egberts research group for their collaboration and assistance throughout my degree. From helping to set up experiments to great technical discussions, the teamwork of the research group has made the whole process smooth and very enjoyable. I also would like to thank and acknowledge the help and guidance of Professor Dr. John Sader at The California Institute of Technology and Professor Dr. Roland Bennewitz at Saarland University.

To my mother Helen Mathias.

Table of Contents

Abstract . . . . . **ii**
Preface . . . . . **iii**
Acknowledgments . . . . . **iv**
Dedication . . . . . **v**
Table of Contents . . . . . **vi**
List of Tables . . . . . **vii**
List of Figures . . . . . **viii**
List of Terms & Abbreviations . . . . . **xv**
1 Introduction **1**
1.1 General Background 2
1.2 Motivation 3
1.3 Objectives 4
1.4 Organization 5
2 Literature Review **6**
2.1 Static AFM 6
2.2 Dynamic AFM 8
2.3 Cantilever Stiffness Calibration 18
2.4 Contact Mechanics 21
2.5 Colloidal Probes 25
3 Mathematical Background **27**
3.1 Spectral Analysis 27
3.2 Cantilever Dynamics 35
4 Methods **48**
4.1 AFM System 48
4.2 Sample Preparation 51
4.3 Cantilever Preparation 51
4.4 Data Acquisition 52
4.5 Analysis Procedure 54
5 Results - Spectral Analysis **58**
5.1 Short Time Fourier Transform 58
5.2 Comparison of CWT and STFT 61
5.3 Summary 66
6 Results - Cantilever Dynamics **67**

6.1 Cantilever Dynamics . . . 67
6.2 Summary . . . 72
7 Results - Cantilever Effective Tip Radius Estimation . . . 73
7.1 Contact Mechanics . . . 73
7.2 Cantilever Probe Verification . . . 82
7.3 Summary . . . 86
8 Conclusions and Future Work . . . 87
8.1 Spectral Analysis . . . 87
8.2 Cantilever Dynamics . . . 88
8.3 Contact Mechanics . . . 88
8.4 Experimental . . . 89
Bibliography . . . 91
Appendix . . . 96

List of Tables

4.1 Overview of sample materials used in testing. Silicon and HOPG values are taken from the literature [55, 56], while PEO and PDMS values were determined by nanoindentation testing (see Appendix 8.4). 51
4.2 Overview of Cantilever Probes Used in Testing. 52
4.3 Overview of Data loggers used in testing. 52

5.1 Example of STFT frequency resolution at different window sizes. The values at 2^{16} and 2^{20} are highlighted„ as these were the lower and upper bounds of the window sizes used with the STFT. 64

7.1 Summary table of tip radius estimates from contact mechanics fitting. *NA* indicates the fitting did not converge or the fit was very poor. 78
7.2 Summary table showing cantilever radii estimates from the tip-sample indentation tests. . . 80
7.3 Summary table showing cantilever radii estimates from the tip-sample indentation tests for the flat punch assumption. 82
7.4 Contact stiffness estimates from the tip-sample indentation tests. Values found from indentation are consistently higher than those from the cantilever dynamics estimates, although only slightly. 82

1 Summary table of Young's modulus calculations for the PDMS sample. The table shows the max force (F_{max}), indentation (D_{max}) and calculated Young's modulus. The mean Young's modulus was determined to be $0.025 \pm 0.002\ GPa$. 98
2 Summary table of Young's modulus calculations for the PEO sample. The table shows the max force (F_{max}), indentation (D_{max}) and calculated Young's modulus. The mean Young's modulus was determined to be $0.22 \pm 0.03\ GPa$. 98

List of Figures

1.1 Schematic illustrating the key principle utilized in contact resonance AFM. The resonance modes of the cantilever are excited (a) out of contact and (b) in contact. By measuring the frequency shift between free and in contact physical properties of the sample can be estimated. Reproduced with permission from Springer Nature [5]. 2

2.1 Schematic showing the major components and setup in AFM. 7

2.2 Comprehensive topography characterization is achieved by performing more than 50 multi-resolution measurements on each material using stylus profilometry (top section), AFM (middle section) and side-view TEM (bottom section). Representative data from each technique at various magnifications are presented for all four materials. For stylus and AFM, the radius of the scanning tip shown in panels (a4), (b4), (c4), (d4) and (e4) is measured using electron microscopy. Reproduced with permission from IOP Surface Topography: Metrology and Properties (STMP) [9]. 8

2.3 (a) Schematic of a DART experimental setup using two sinusoidal drives with frequencies such that one f_1 is below and the other f_2 is above the contact resonance frequency f_0 of the cantilever. These sine signals are summed together and then used to drive the tip–sample contact. Cantilever tip motion can be excited by either electromechanical interactions (termed the PFM mode, where the tip–sample voltage is modulated) or the acoustic mechanical interactions (termed the AFAM mode, where the physical sample position is modulated). (b) An illustration of the principle of DART. When the resonance frequency changes from f_1 to f_2 the difference in the amplitudes A_1 to A_2 indicates the direction of the frequency shift. Therefore, $A_2 - A_1$ can be used as the error signal in a feedback loop where the excitation frequencies f_1, f_2 are changed in order to maintain $A_2 - A_1 \approx 0$, thereby tracking the resonance frequency. Reproduced with permission from IOP Nanotechnology [13]. 10

2.4 Viscoelastic maps of relative modulus (a) E'/E'_{PP} and (b) E''/E''_{PP} obtained with DART contact scanning for a scan velocity $v = 1\,\mu m/s$. (c) Calculated storage modulus ratio (black) and loss modulus ratio (red) versus υ and pixel acquisition time t_{acq}. Dashed lines indicate bulk predictions from time temperature superposition analysis. Reprinted with permission from Langmuir 2011, 27, 23, 13983-13987 https://doi.org/10.1021/la203434w. Copyright 2011 American Chemical Society [6]. 11

2.5 Nanomechanical maps of a LDPE polymer sample. (a) Young's modulus. (b) Viscosity coefficient. (c) Loss tangent. (d) Retardation time. The bottom panels show the cross-sections obtained across the dashed lines marked in the nanomechanical maps. The blue regions show the values that lie within a 5% window from the average value obtained from the bimodal AM-FM maps. A tip radius of 12 nm has been used to fit the data. Reproduced from Benaglia et al. with permission from the Royal Society of Chemistry [12]. 12

2.6 AFM contact resonance data on mixed cellulose nanoparticle sample. (a) Topography image of first region, (b) frequency map of the 5th eigenmode of the first region, (c) topography image of second region, (d) frequency map of the 5th eigenmode of the second region. The numbered boxes show areas of the sample where data has been extracted for analysis. The arrows in b and d show the location of jumps in resonance frequency in the slow scan direction. Reproduced with permission from Springer Nature [14]. 13
2.7 Full field elastic modulus map of (a) non-exposed and (b) 6 h UV exposed CFRP sample. Reproduced with permission from Springer Nature [19]. 14
2.8 Plot showing the full force distance curve in a force spectroscopy sweep. (1) The approach where the cantilever is out of contact and slowly being brought closer to the surface. (2) The Jump-to-Contact (JTC) point. (3) The cantilever is fully in contact and is being pressed into and out of the sample. (4) The pull-off point when the cantilever jumps out of contact. This test was conducted on a HOPG sample with a Silicon contact probe. 15
2.9 The paths for jump-to-contact and jump-off-contact. In an apparatus of finite stiffness, jump-to-contact and jump-off-contact occur when the force gradient exceeds the spring constant of the cantilever. In a fixed-grips device, jump-to-contact and jump-off-contact occur at the vertical tangents of the force-approach curve. Reproduced with permission from Taylor & Francis Journal of Adhesion. Wu et al. [20]. 16
2.10 Figure 4. Plots of tip radius (a), pull-off force (b), and work of adhesion (c), as a function of distance scanned for the four tips. Reprinted with permission from ACS Nano 2010, 4, 7, 3763–3772 https://doi.org/10.1021/nn100246g. Copyright 2010 American Chemical Society [10]. 18
2.11 Plot showing the three major contact mechanics models; Hertz, DMT, and JKR. 23
2.12 Plot of the Tabor parameter with the two outer limits leading to the DMT and JKR contact models. 24
2.13 Scanning Electron Microscope (SEM) images of a Copper colloid particle used in testing. The Copper particle was glued onto a tip less contact cantilever with a length of 450 (μm) and a width of 50 (μm). Note that particles of this size are so massive that the subsequent cantilever models used are not applicable. For this reason the results from these massive colloid probes are not included in the results. (a) is a side view of the whole cantilever with the Copper particle glued at the end. (b) is zoomed in only on the colloid with the glue at the bottom between the colloid and the cantilever. 26

3.1 (a) Cantilever deflection in force-distance curve. (b) Just before the JTC the cantilever oscillation relaxes and the cantilever deflection down slightly. (c) Fourier transforms of the cantilever deflections in (b). Black line indicate the frequency spectrum before the jump (-2 to 0 ms) while the red line is after the jump to contact (0 to 4ms). (d) Wavelet transform of the deflection data in (b) visualized in a scalogram. The cantilever relaxation just before the jump can be seen here. Reproduced with permission from IOP Nanotechnology 2015 [45]. 30

3.2 An example of the Morlet wavelet (black). The wavelet is formed by a standard sinusoidal wave (red) bounded by a Gaussian envelope (blue). 32
3.3 a) The complex Morlet or Gabor mother wavelet at different shaping factors shown with the corresponding Heisenberg boxes showing the time and frequency uncertainty. b) Time delay and translation transforms that can be applied to a daughter wavelet in the wavelet transform. Reproduced with permission from Beilstein J. Nanotechnology 2010, 1, 172–181. https://doi.org/10.3762/bjnano.1.21, © 2010 rights holder [50]. 33
3.4 Time and frequency scaling for different transforms. a) The Time Domain is shown with the higher possible time resolution. b) The Fourier Domain is shown having the highest possible frequency domain. c) The STFT is shown with a statically windowed time and frequency resolution. d) The Wavelet Transform is shown with a dynamically changing time and frequency resolution. Reproduced with permission from Springer Nature [43]. 34
3.5 Plot of the dispersion relation between normalized frequency (f_n/f_0) and normalized stiffness (k^*/k_c) comparing the point mass model and the spring coupled cantilever (Figure 3.6). Reprinted from U. Rabe, K. Janser, W. Arnold; Vibrations of free and surface-coupled atomic force microscope cantilevers: Theory and experiment. Rev Sci Instrum 1 September 1996; 67 (9): 3281–3293. with the permission of AIP Publishing [4]. 36
3.6 Schematic of the spring-coupled cantilever with the tip-sample contact at the cantilever end. 38
3.7 Boundary conditions of an AFM cantilever with uniform cross section: (a) Clamped-free cantilever, (b) clamped spring-coupled cantilever, (c) clamped-pinned cantilever. Reprinted from U. Rabe, K. Janser, W. Arnold; Vibrations of free and surface-coupled atomic force microscope cantilevers: Theory and experiment. Rev Sci Instrum 1 September 1996; 67 (9): 3281–3293. with the permission of AIP Publishing [4]. 39
3.8 Dispersion relation of normalized frequency (f/f_0) vs normalized stiffness (k^*/k_c) for the 1st mode in Model 1 (Figure 3.6). 40
3.9 Schematic of the spring-coupled cantilever with the tip-sample contact located at the accurate cantilever tip position. 41
3.10 Dispersion relation of normalized frequency (f/f_0) vs normalized stiffness (k^*/k_c) for the 1st mode in Model 2 (Figure 3.9). 43
3.11 Schematic of the spring-coupled cantilever with the tip-sample contact located at the accurate cantilever tip position and including lateral forces. 43
3.12 Dispersion relation of normalized frequency (f/f_0) vs normalized stiffness (k^*/k_c) for the 1st mode in Model 3 (Figure 3.11). 45
3.13 Schematic of simple damped cantilever model adding a dash pot alongside the spring in the contact. 46
3.14 Schematic of damped cantilever model incorporating the tip position and lateral force. . . . 46

4.1 Image of Agilent Keysight 5500 Air AFM scanner and platform. The scanner is suspended on bungee cords and its locked in a steel box. 49
4.2 Image of the Asylum MFP-3D Air AFM scanner (left) and sample platform (right). 49

4.3 Example plot showing a approach portion of a force distance curve. 50
4.4 An example Force-Time series output from the external data logger. The raw signal is in Volts but is converted to Force from calibration. 53
4.5 Flow diagram showing the primary analysis procedure for estimating the cantilever tip radius. 54
4.6 Visualization of the time windowing process done during the STFT analysis. Each dashed red line indicates the boundary between one window and another. The window sizing in this figure is (2^{20}) to emphasize the boundary between time windows. 55
4.7 Example frequency spectrum of the cantilever when out of contact. The first mode to be fit is circled in red with subsequent modes at higher frequencies and lower amplitudes. 55
4.8 An example resonance peak fit using the according to the Lorentz distribution (Equation 3.1). 56

5.1 Cantilever Frequency (f) vs Normal Force (F_N) during the contact portion of a force-distance curve on a HOPG sample. After the large frequency change during the cantilever jump into contact the frequency slightly increases before plateauing with increasing force. 59
5.2 Cantilever Quality Factor (Q) vs Normal Force (F_N) during the contact portion of a force-distance curve on a HOPG sample. The plateauing phenomenon observed with the frequency is seen as well with the quality factor. 59
5.3 Cantilever Quality Factor (Q) vs Normal Force (F_N) during the contact portion of a force-distance curve on a PDMS sample. When compared to more rigid samples this material does not show any consistent trend in quality factor due to the large variability in the frequency peak width. 60
5.4 Example full frequency spectrum of a HOPG sample when the cantilever is out of contact (black) and in contact (red). When in contact the frequency modes shift to a higher frequency, modeled by the cantilever dynamics models, along with a change in the peak shape. In the case of HOPG and other stiff samples the peak becomes sharper resulting in a higher cantilever quality factor. 60
5.5 Example full frequency spectrum of a PDMS sample when the cantilever is out of contact (black) and in contact (red). When in contact the frequency modes shift to a higher frequency, modeled by the cantilever dynamics models, along with a change in the peak shape. In the case of PDMS the peak becomes much more broad along with a lower amplitude. This indicates higher damping and a smaller quality factor. 61
5.6 Frequency fitting results for a force spectroscopy sweep on a HOPG sample. (a) The large erroneous frequency jumps at the jump to contact can be seen along with the steps changes in frequency due to the poor frequency resolution of the CWT at the low frequency of the 1st mode of oscillation. (b) This is a zoomed in image just on the in contact portion. Note that this frequency shift in contact is barely noticeable as this wavelet data set covers just over one millisecond. 62
5.7 Comparison between Fourier (STFT) and wavelet (CWT) transform quality factor (Q) fitting at different wavelet time-bandwidth values. Note the STFT value is constant for a given window size. 63

5.8 Comparison between 1st mode resonance peak for the STFT (Fourier) and CWT (wavelet) transforms. (a) Fitting result from the STFT at a (2^{16}) window size with the fitting outputs being ($f_{STFT} \approx 12.465kHz$, $Q_{STFT} \approx 20.158$). (b) Fitting result for the wavelet transform with a time bandwidth of 120 and 48 voices per octave. The fitting outputs are ($f_{CWT} \approx 12.81kHz$, $Q_{CWT} \approx 7.0265$). 65
5.9 Frequency resolution of CWT as a function of scale size. The CWT frequency resolution has log_2 scaling dependent on (NV) (voices per octave) while the STFT has a constant resolution for a given window size. 66

6.1 Dispersion relation of experimental frequency results laid over analytical models for model 1 (3.6), model 2 (3.9), and model 3 3.11 for a Silicon contact probe on a HOPG sample. 68
6.2 Dispersion relation of experimental frequency results laid over analytical models for model 1 (3.6), model 2 (3.9), and model 3 3.11 for a Diamond coated Silicon contact probe on a Silicon sample. 69
6.3 Dispersion relation of experimental frequency results laid over analytical models for model 1 (3.6), model 2 (3.9), and model 3 3.11 for a Silicon contact probe on a PEO sample. 69
6.4 Dispersion relation of experimental frequency results laid over analytical models for model 1 (3.6), model 2 (3.9), and model 3 3.11 for a Silicon contact probe on a PDMS sample. 70
6.5 Dispersion relation plotting experimental frequency results laid over analytical models for model 1 (3.6), model 2 (3.9), and model 3 (3.11). 71
6.6 Dispersion results of the damped model illustrating the difference between the damping model used (Figure 3.57) and the undamped models. 72

7.1 DMT model fitting results of Silicon Contact Probe on HOPG sample. The Young's modulus used for this fitting was taken to be 20 GPa [55]. 74
7.2 DMT model fitting results of Diamond coated Silicon Contact Probe on Silicon sample. Young's modulus for the silicon sample was taken to be 160 GPa [55, 56]. 75
7.3 JKR model fitting results of Silicon Contact Probe on Polyehtylenoxide (PEO) sample. Young's modulus of the PEO sample was determined to be 0.22 ± 0.03 GPa by nanoindentation testing (Appendix 2). 76
7.4 JKR model fitting results of Silicon Contact Probe on Polydimethylsiloxane (PDMS) sample. Young's modulus of the PDMS sample was determined to be 0.025 ± 0.002 GPa by nanoindentation testing (Appendix 1). 76
7.5 DMT fit of contact stiffness vs normal force for a Silicon probe on a HOPG sample using the damping model shown in Figure 3.57. 77
7.6 Contact mechanics fitting results for a test using a Borosilicate glass colloid probe on a HOPG sample. 78

7.7 Fitting Result from force (F_N) vs sample indentation (D) using the DMT contact mechanics model. Fitting results in a tip radius estimate of ($R \approx 4.33 \pm 0.02\ pm$). Test was conducted using a Silicon contact probe on a freshly cleaved HOPG sample at standard atmospheric conditions. 79
7.8 Fitting Result from force (F_N) vs sample indentation (D) using the JKR contact mechanics model. Fitting results in a tip radius estimate of ($R \approx 47.6 \pm 0.3\ pm$). Test was conducted using a Silicon contact probe on a PEO sample at standard atmospheric conditions. 80
7.9 Fitting Result from force (F_N) vs sample indentation (D) using the flat punch contact model. Fitting results in a tip radius estimate of ($R \approx 0.210 \pm 0.001\ nm$). Test was conducted using a Silicon contact probe on a freshly cleaved HOPG sample at standard atmospheric conditions. 81
7.10 Fitting Result from force (F_N) vs sample indentation (D) using the flat punch contact model. Fitting results in a tip radius estimate of ($R \approx 6.75 \pm 0.04\ nm$). Test was conducted using a Silicon contact probe on a PEO sample at standard atmospheric conditions. 81
7.11 Scanning Electron Microscope (SEM) images of a Platinum coated Silicon contact probe. This probe along with other contact probes was utilised for the force spectroscopy experiments. The radii of the tip for these contact probes are in the range of ($5-25\ nm$) depending on the use of the tip. (a) shows a top view, while (b) is a side view used to calculate the radius. . . . 83
7.12 Scanning Electron Microscope (SEM) images of a Borosilicate Glass colloid probe. Note that the colloid is the large spherical object, while the grey material surrounding it is excess glue from its application. This colloid probe has a radius of ($\approx 9\ \mu m$), and many of the other glass colloids used are close in size to this one shown. (a) is a top view of the colloid, and (b) is a side view. 84
7.13 Calibration grating TGT1 from TipsNano. Spacing of tips is 2.12 μm diagonally and 3.0 μm laterally. 84
7.14 Topography scan of a Borosilicate glass colloid probe on the TGT1 calibration grating. 85
7.15 Average row height profiles from the scan shown in Figure 7.14. 85

1 Elastic unloading curves for several materials obtained in nanoindentation experiments with a Berkovich indenter plotted on linear axes with displacements shifted to a common origin. From Oliver and Pharr [36] 97
2 Example Elastic unloading curves for the PEO sample obtained from nanoindentation experiments with a Berkovich indenter. Slope of curve in red is the linear fit used to determine the Young's modulus of the sample from equation 2.28. 97

List of Terms & Abbreviations

AFM	Atomic Force Microscopy
SEM	Scanning Electron Microscope
TEM	Transmission Electron Microscope
$CR-AFM$	Contact Resonance AFM
PSD	Photosensitive Diode
$UNCD$	Ultra-Nanocrystalline Diamond
$AM-AFM$	Amplitude Modulation AFM
$DART$	Dual AC Resonance Tracking
$LDPE$	Low-Density Polyethylene
CNC	Cellulose Nanocrystal
JTC	Jump-to-Contact
JKR	Johnson-Kendall-Roberts
DMT	Derjaguin-Muller-Toporov
S	Cantilever Sensitivity $(\frac{V}{m})$
q	Cantilever Deflection (m)
D	Sample Indentation (m)
k^*	Contact Stiffness $(\frac{N}{m})$
E	Young's Modulus (Pa)
E^*	Reduced Young's Modulus (Pa)
SHO	Simple Harmonic Oscillator
$STFT$	Short-Time Fourier Transform
FFT	Fast Fourier Transform
CWT	Continuous Wavelet Transform
κ	Lateral Stiffness $(\frac{N}{m})$
G	Shear Modulus (Pa)
G^*	Reduced Shear Modulus (Pa)
ν	Poisson's Ratio
f	Cantilever Frequency (kHz)

f_0	Cantilever Frequency (out of contact) (kHz)
Q	Cantilever Quality Factor
Q_0	Cantilever Quality Factor (out of contact)
k_c	Cantilever Stiffness ($\frac{N}{m}$)
a_c	Contact Radius (m)
δ	Sample Deformation (m)
F_N	Normal Force (N)
F_a	Adhesive Force (N)
μ_T	Tabor Parameter
k_B	Boltzmann Constant ($\frac{J}{K}$)
L	Cantilever Length (m)
L_1	Distance from fixed base to tip of cantilever (m)
ρ_f	Fluid Density ($\frac{kg}{m^3}$)
Re	Reynolds Number
K_0	Zeroth order modified Bessel function of the second kind
K_1	First order modified Bessel function of the second kind
$\Gamma(w)$	Hydrodynamic function
$PDMS$	Polydimethylsiloxane
PEO	Polyethyleneoxide
BSG	Borosilicate Glass

Chapter 1

Introduction

The study of material surfaces and interfaces has been a fascinating scientific endeavour characterised by complexity and a quest for understanding. From the early philosophical contemplations on surfaces and friction by ancient Greek philosophers to the empirical investigations by visionaries like da Vinci and Amontons, humanity has gradually strived to quantify and comprehend the intricacies of direct contact between two surfaces. As the industrial revolution unfolded and progressed into the early 20th century, surface science began to take shape with the emergence of theories attempting to explain the underlying interactions within these contacts.

A significant milestone in this field occurred in 1986 with the invention of the Atomic Force Microscope (AFM) by Binnig, Quate, and Gerber at IBM Zurich [1]. This groundbreaking tool revolutionised the study of surfaces and friction, enabling nanoscale investigations on non-conducting materials. The AFM employs a physical cantilever probe that can interact at a distance or make full contact with a sample surface. By measuring the deflection of the cantilever probe, researchers can gather valuable insights into the forces and material properties present, using well-established solid mechanics theories [2].

Despite the remarkable success and advancement of AFM technology, making it one of the most widely used tools for nanoscale testing and measurements, a significant challenge remains. The precise contact between the cantilever probe tip and the sample surface remains elusive, hidden from detection. This limitation hinders a comprehensive understanding of the interactions occurring within the contact zone [3]. Consequently, novel research initiatives have emerged with the aim of uncovering these hidden interactions through in situ measurements and characterisation.

In this context, the research project summarised in this thesis strives to contribute to the pursuit of in situ measurements by incorporating the dynamics of the cantilever probe and the contact mechanics at the nanoscale. By delving into the behaviour of the cantilever during contact, the goal is to gain deeper insights into the forces and phenomena that arise at the surface interface. This endeavour holds significant promise, as it addresses not only a critical aspect of AFM studies but also paves the way for more accurate measurements and an improved understanding of the complex behaviours exhibited by material surfaces and interfaces.

To overcome the challenge of the buried contact, researchers are exploring new techniques and

approaches that enable the detection and characterisation of these direct interactions. These advances surrounding in situ measurements hold great potential for unraveling the mysteries of surface interactions and opening new avenues for scientific discovery and technological innovation.

1.1 General Background

The focus of this thesis is to investigate the principle of contact resonance measurement and its application in analysing force and stiffness changes. Contact resonance is a technique that estimates changes in force and stiffness by measuring alterations in the oscillation frequency of a cantilever. This method uses theoretical analytical models that connect the cantilever motion to the contact stiffness of the probe sample system [4]. Over the years, these models have evolved from simple rectangular cantilevers to more sophisticated representations incorporating various geometric dimensions and characteristics [3, 4]. Figure 1.1 shows a simple schematic of the physical mechanism of contact resonance, along with the resulting measured frequency and damping changes in the cantilever motion.

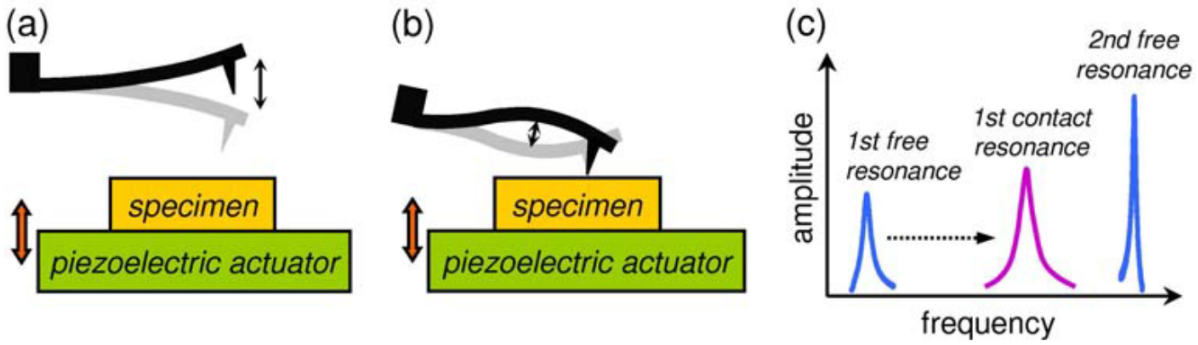


Figure 1.1: Schematic illustrating the key principle utilized in contact resonance AFM. The resonance modes of the cantilever are excited (a) out of contact and (b) in contact. By measuring the frequency shift between free and in contact physical properties of the sample can be estimated. Reproduced with permission from Springer Nature [5].

Currently, the estimation of contact stiffness using these cantilever models follows an indirect approach. This simplification avoids the complexities of mechanical interactions at the contact interface, allowing for easier analysis [6]. However, this approach limits the amount of information that can be obtained about the contact itself.

Therefore, the motivation behind this project stems from the existing limitations of contact resonance approaches. By addressing these limitations, the aim is to develop a more comprehensive understanding of contact mechanics and enhance the accuracy and applicability of contact stiffness estimation. Through this research, the ultimate future goal is to provide a deeper insight into the characteristics of the contact interface and advance the field of contact resonance analysis.

By exploring the relationship between contact resonance and contact mechanics, this thesis aims to uncover valuable insights about the behaviour of the tip during contact. Once understood, the

underlying mechanisms will allow for a more effective interpretation of changes in the cantilever frequency and damping, providing a more granular understanding of the contact characteristics.

1.2 Motivation

As mentioned above, the project is driven by the desire of the AFM community to extract more knowledge and insights directly from experimental data, moving towards more in situ results. The current technique in contact resonance involves comparing a test sample with unknown properties to a reference sample with known properties, allowing the estimation of the test sample Young's modulus. However, challenges arise when quantifying the physical importance of the compared contact stiffness values, as different material classes exhibit varying mechanical responses and properties.

In this referencing method, the contact stiffness of the test sample (k^*_{test}) is determined through the frequency change when in contact, and comparing to the reference sample, the Young's modulus can be estimated. More about this method is discussed in Chapter 2.1 and in Appendix 8.4, specifically the reference equation, and contemporary research results.

To address these challenges, this project aims to directly quantify the contact stiffness calculated from the contact resonance phenomenon and to estimate the physical properties of the contact. While the ultimate goal is to determine the mechanical properties of the contact, this thesis focuses on a more easily verifiable quantity: the effective radius of the cantilever tip when in contact. By leveraging the well-known nature of this parameter, which can be externally verified using techniques such as Scanning Electron Microscopy (SEM) and reverse tip imaging, it becomes possible to gain insights into the mechanical and material properties of the contact.

To achieve these objectives, the project will begin by clearly defining specific research questions or objectives. By doing so, it will provide a more focused direction and framework for the investigation. Additionally, potential limitations and challenges associated with the project will be acknowledged. These may include factors such as measurement uncertainties, sample preparation variations, or experimental constraints.

In addition, the project will discuss the broader impact and applications of its findings. Direct quantification of contact stiffness and estimation of physical properties have the potential to significantly advance material characterisation and nanoscale investigations in the AFM community and related fields. By shedding light on the intricate relationships between contact stiffness and mechanical properties, this research can pave the way for enhanced understanding and manipulation of materials at the nanoscale.

Lastly, while not delving into technical specifics, the project will provide a brief overview of the research methodology. This will include sample preparation, data acquisition approaches, and analysis methods, providing the reader with a general understanding of how the project will be conducted.

1.3 Objectives

This study aims to investigate the behaviour and properties of cantilever systems under various experimental conditions. Through experimental testing and analysis, the research seeks to contribute to our understanding of this field and potentially advance scientific knowledge, technological applications, and practical implementations.

Experimental Testing Objectives

The primary objective of the experimental testing phase is to explore the effects of different experimental conditions by varying the cantilever and sample materials along with the cantilever geometry. By covering a wide range of physical property values modeled by theory, the study aims to gain insight into the behaviour of cantilever systems in various scenarios. Detailed coverage of this experimental setup can be found in Chapter 4, which provides a detailed explanation of the procedures and findings.

Analysis Objectives

The analysis phase of the project consists of three independent sections, each with its own set of objectives and results. These sections are: spectral analysis, cantilever dynamics, and contact mechanics.

Spectral Analysis

The major objective of spectral analysis is to accurately determine the spectral characteristics of the cantilever oscillation, specifically focusing on frequency and damping. To achieve this, the study employs two techniques: the short-time Fourier transform (STFT) and the continuous wavelet transform (CWT). The STFT allows for general time-frequency analysis, while the CWT has potential for a more detailed examination of oscillatory behaviour at very short time scales. These methods will be extensively discussed in Chapters 3.1 and 5, providing a comprehensive understanding of their implementation and the insights they yield.

Cantilever Dynamics

The objective of the cantilever dynamics analysis is two-fold. First, the objective is to validate existing analytical models by comparing their predictions with real physical cantilever probe experiments. By evaluating the performance of different models, the study seeks to identify the most reliable and accurate models for practical applications. Second, the analysis aims to establish the relationship between the different models and contact mechanics. By understanding how models correlate with contact phenomena, the research project aims to optimise their use and gain a deeper understanding of cantilever behaviour in practical AFM testing scenarios.

Contact Mechanics

The final step of the analysis focuses on the mechanics of contact and its connection to the spectral analysis of the cantilever. This objective involves estimating the radius of the tip and comparing this estimate with other well-established tip measurement methods. By relating the spectral analysis results to the conditions at the contact point between the tip and the sample, the study aims to provide valuable insight into contact phenomena. This evaluation not only strengthens the reliability and accuracy of the spectral analysis, but also contributes to our understanding of the contact mechanics in cantilever systems.

By addressing these objectives in both the experimental testing and analysis phases, this study aims to contribute to the understanding of the behaviour and properties of cantilever systems in various experimental conditions. Furthermore, it hopes to pave the way for advances in materials science, technological applications, and practical implementations in relevant fields such as composite materials and biological engineering.

1.4 Organization

Throughout my thesis I have been trained and advised by my supervisor Dr. Philip Egberts in the Mechanical and Manufacturing department in the Schulich School of Engineering at the University of Calgary. The work carried out in this thesis is predominantly done by me, although help was given by Dr. Egberts along with other members of the research group in experimental setup and testing.

Chapter 2

Literature Review

In this chapter, the prior research has been discussed from the invention of the AFM up to recent research conducted on both contact mode and non-contact modes incorporating contact resonance. In addition, the history and developments in the contact mechanics modelling are introduced along with the key connections between the AFM and contact mechanics.

2.1 Static AFM

As mentioned in Chapter 1 the Atomic Force Microscope (AFM) operates by measuring the deflection of the cantilever probe either through direct contact (contact mode) or interacting at a distance (tapping, kelvin probe, etc.). Broadly speaking, AFM testing can be split into two categories, static and dynamic AFM. In essence, static AFM modes are where the sample Z position (see Figure 2.1) remains constant along with any voltage biases. In dynamics AFM these different testing parameters change through the test or scan.

Moving to static AFM testing itself, the cantilever is first brought into contact with the sample. A relatively constant cantilever height is achieved by applying a positive voltage bias as a set point for the machine's Z position through its piezoelectric feedback loop [7]. Scanning of the surface can then be performed by translating the cantilever in the X and Y directions along the sample surface. Any deviations in the surface topography will cause the cantilever deflection to change, which will then shift the laser reflection position vertically on the photosensitive diode (PSD). Additionally, the friction force can be measured by the lateral deflection of the cantilever as it moves along the surface, which causes the laser reflection to translate horizontally. By comparing the trace and retrace (forward and backward) scans of the cantilever probe the net friction force can be determined given the cantilever lateral and normal stiffness values are known. In Figure 2.1 a simple schematic of the AFM setup in contact mode can be seen with the cantilever probe, sample piezoelectric Z position, and the laser reflection on the PSD. Other setups are commonly used in AFM but, for the tests conducted in this thesis, the AFM was primarily used in contact mode.

The most direct application of static AFM scanning in contact mode is the acquisition of surface topography and morphology [8]. In contact mode, the AFM probe physically touches the sample surface

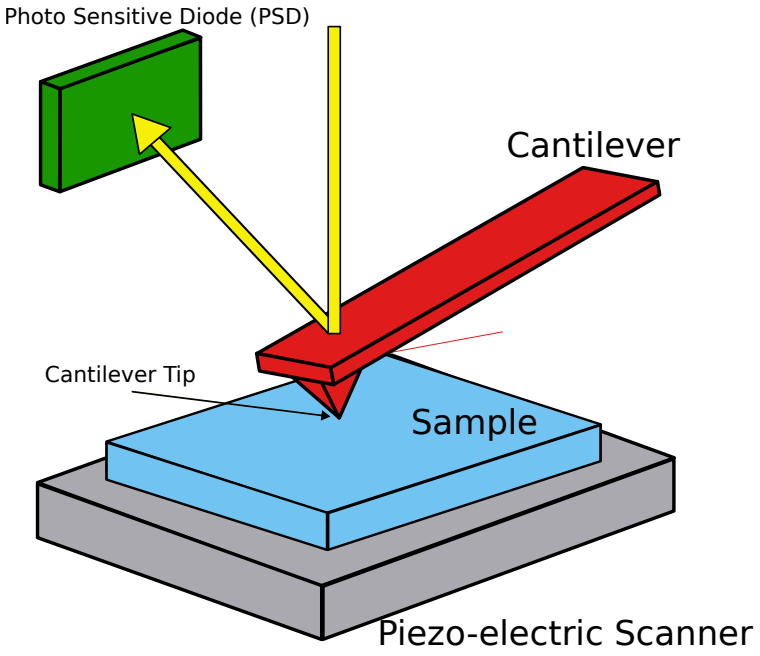


Figure 2.1: Schematic showing the major components and setup in AFM.

while scanning. The probe is attached to a flexible cantilever and, as the probe tip scans the sample, the deflection of the cantilever is monitored. The deflection is used to maintain a constant force between the probe and the sample surface, allowing for accurate imaging of the sample topography.

There are several advantages in using contact mode scanning in AFM compared to other tools such as profilometry or SEM, including very high spatial resolution, versatility in test samples, and fast real-time imaging of surface structures. For a more complete characterisation of a surface, multiple tools may be required, but AFM has proven to be effective for a wide number of use cases [9]. Figure 2.2 showcases the versatility and accuracy of AFM static contact scanning where AFM scans of several materials are shown together with other measurement tools.

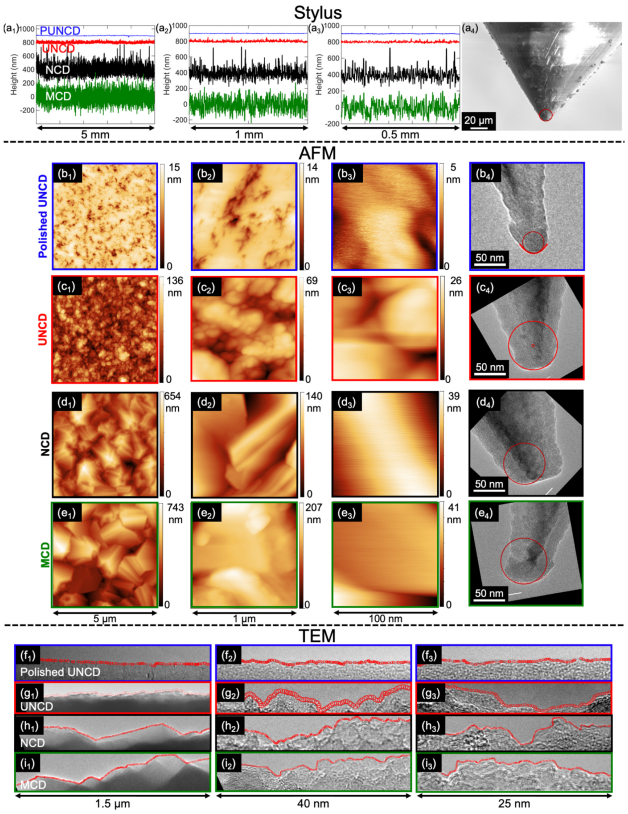


Figure 2.2: Comprehensive topography characterization is achieved by performing more than 50 multi-resolution measurements on each material using stylus profilometry (top section), AFM (middle section) and side-view TEM (bottom section). Representative data from each technique at various magnifications are presented for all four materials. For stylus and AFM, the radius of the scanning tip shown in panels (a4), (b4), (c4), (d4) and (e4) is measured using electron microscopy. Reproduced with permission from IOP Surface Topography: Metrology and Properties (STMP) [9].

Beyond imaging the surface, recent developments in fabrication have allowed specialised sample surfaces to be made, which can also image the probe tip as well. One of such sample materials is ultra-nanocrystalline diamond (UNCD), which is a unique form of diamond with grain sizes in the nanometre range [10]. It has exceptional mechanical, electrical, and chemical properties, making it suitable for various applications. AFM, including contact mode scanning, has been used to investigate UNCD samples and explore their surface characteristics [10]. Such applications include enhanced nanoscale surface roughness analysis of the UNCD surface, mapping the grain size and patterning of the surface, and more precise mechanical characterisation through precision control over the hardness, elasticity, and adhesive properties of the sample [9].

2.2 Dynamic AFM

Since its invention, many advances have been made in the field of AFM, with many focused on new techniques and modes of operation. These different modes aim to measure a different physical property by exploiting a measurable and repeatable phenomenon of either the cantilever or the contact. In the

case of contact resonance AFM (CR-AFM) by measuring the changing frequency and amplitude of the oscillation, knowledge about contact properties can be gained [11].

Contact Resonance AFM

Moving past the basic static AFM setup (Figure 2.1) in dynamic AFM testing, the system continuously changes parameters such as the sample Z-position or voltage set points, altering the cantilever oscillation or electric potential with the sample surface [5]. In the procedure described in this thesis, the main dynamic testing involves performing force spectroscopy tests. In these tests, the position of the sample along the Z axis is varied repeatedly. Moreover, the measurements incorporate the contact resonance phenomenon, although they are based solely on the thermal oscillation of the cantilever without any external forcing applied. Many techniques incorporate the oscillation of the cantilever to extract physical results, such as tapping mode or amplitude modulation AFM (AM-AFM), but this review will focus on the contact resonance technique in particular.

Forced contact resonance, also known as forced oscillation or frequency modulation, involves driving the cantilever at a fixed frequency when in contact with the surface and measuring its response. In this technique, an external force or frequency modulation is applied to the cantilever, typically using a piezoelectric actuator [3, 12]. The resonant frequency and quality factor of the cantilever are determined by analysing its response to the applied force or modulation. Forced contact resonance can provide precise measurements of the mechanical properties of materials. It enables the determination of dynamic mechanical properties, including the elastic modulus and viscoelastic behaviour [6]. This technique is particularly useful for studying materials with complex mechanical properties or heterogeneous surface structures.

The results of research using forced contact resonance techniques have become important in measuring the viscoelastic behaviour of polymers and heterogeneous materials such as composite materials or complex biological samples [11]. In the following Figure 2.3 an example setup for forced contact resonance through Dual AC Resonance Tracking (DART) mode is shown, where viscoelastic measurements can be performed in real time on a sample. In this DART mode, the cantilever is oscillated by piezoelectric crystals at frequencies lower than and higher than the cantilever resonant frequency. When the cantilever frequency changes, the DART tracking can adjust the lower and upper frequencies to track the cantilever frequency in real time [13]. The results of this setup (Figure 2.4) show the relationship between the applied normal force and the change in frequency of the cantilever probe. This, along with the determination of the cantilever damping, through the quality factor, allows researchers to estimate the mechanical and viscoelastic properties of different nanomaterial structures within a complex composite material [6].

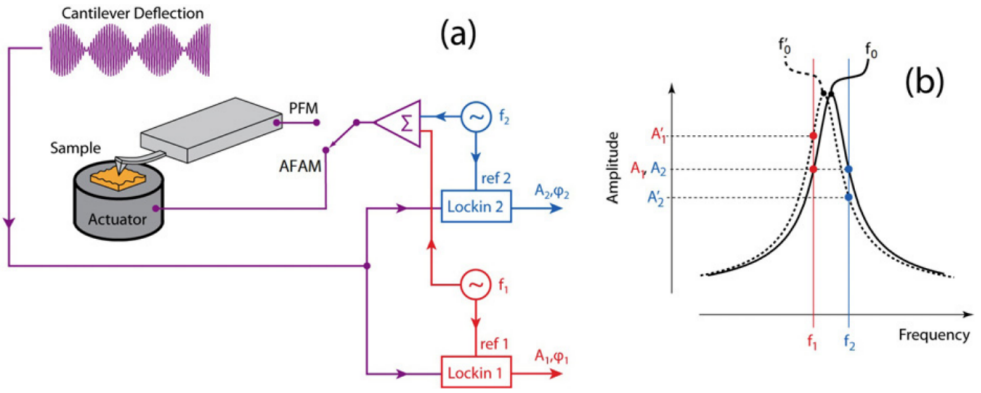


Figure 2.3: (a) Schematic of a DART experimental setup using two sinusoidal drives with frequencies such that one f_1 is below and the other f_2 is above the contact resonance frequency f_0 of the cantilever. These sine signals are summed together and then used to drive the tip–sample contact. Cantilever tip motion can be excited by either electromechanical interactions (termed the PFM mode, where the tip–sample voltage is modulated) or the acoustic mechanical interactions (termed the AFAM mode, where the physical sample position is modulated). (b) An illustration of the principle of DART. When the resonance frequency changes from f_1 to f_2 the difference in the amplitudes A_1 to A_2 indicates the direction of the frequency shift. Therefore, $A_2 - A_1$ can be used as the error signal in a feedback loop where the excitation frequencies f_1, f_2 are changed in order to maintain $A_2 - A_1 \approx 0$, thereby tracking the resonance frequency. Reproduced with permission from IOP Nanotechnology [13].

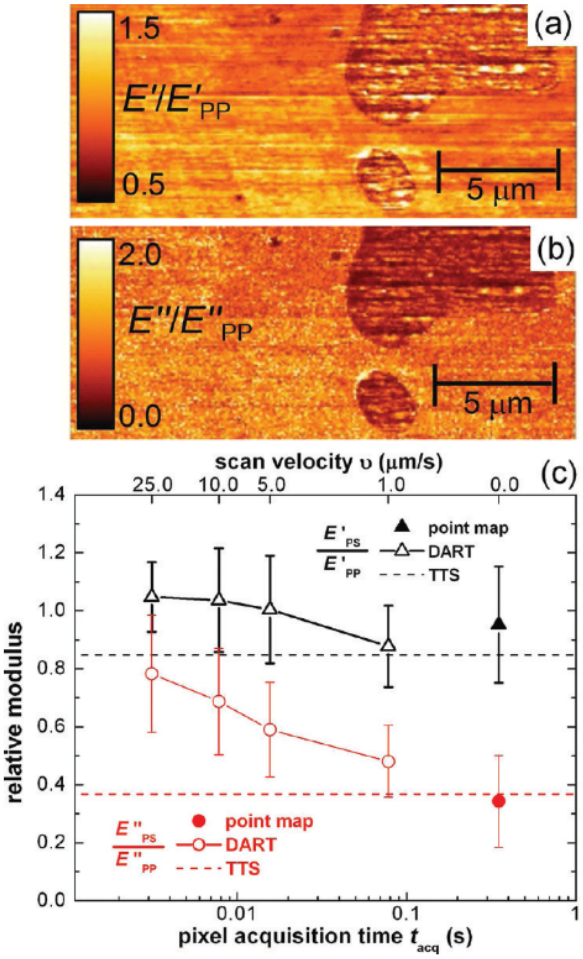


Figure 2.4: Viscoelastic maps of relative modulus (a) E'/E'_{PP} and (b) E''/E''_{PP} obtained with DART contact scanning for a scan velocity $v = 1\ \mu m/s$. (c) Calculated storage modulus ratio (black) and loss modulus ratio (red) versus υ and pixel acquisition time t_{acq}. Dashed lines indicate bulk predictions from time temperature superposition analysis. Reprinted with permission from Langmuir 2011, 27, 23, 13983-13987 https://doi.org/10.1021/la203434w. Copyright 2011 American Chemical Society [6].

This determination of mechanical properties through the contact resonance phenomenon is shown in Figure 2.5 where Young's modulus, viscosity, loss tangent, and retardation time can be estimated for the polymer Low-Density Polyethylene (LDPE).

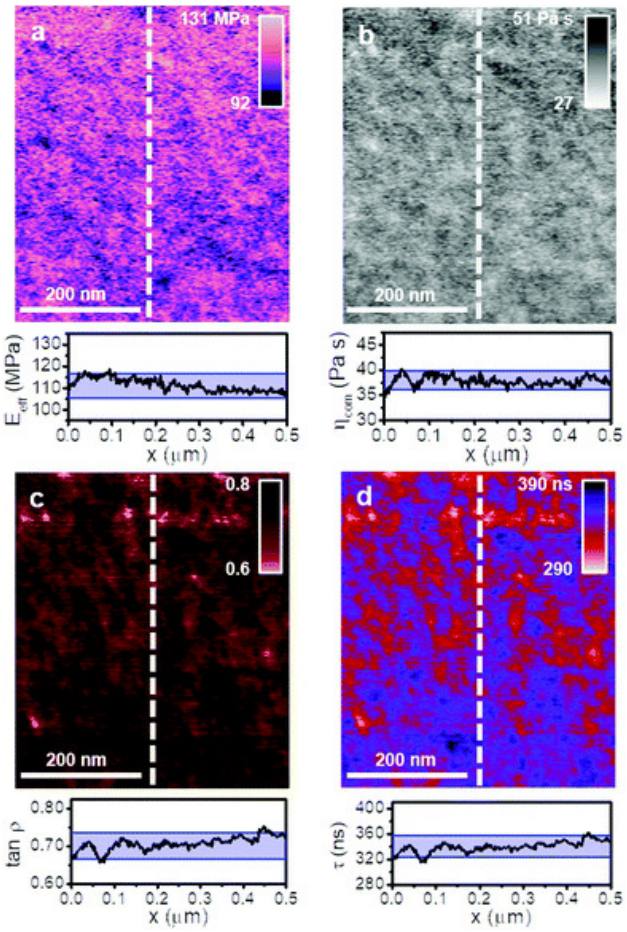


Figure 2.5: Nanomechanical maps of a LDPE polymer sample. (a) Young's modulus. (b) Viscosity coefficient. (c) Loss tangent. (d) Retardation time. The bottom panels show the cross-sections obtained across the dashed lines marked in the nanomechanical maps. The blue regions show the values that lie within a 5% window from the average value obtained from the bimodal AM-FM maps. A tip radius of 12 nm has been used to fit the data. Reproduced from Benaglia et al. with permission from the Royal Society of Chemistry [12].

Examples of this mechanical probing are relevant for materials with heterogeneous structure such as that of a composite material or when nanoparticle additives are incorporated. In the work of Wagner et al. they investigated the differing Young's moduli on different forms of cellulose nanocrystals (CNCs) using the contact resonance technique [14]. In Figure 2.6 the different types of CNCs, tunicate and wood, are highlighted, with the different frequency shifts modelled through the cantilever models to estimate Young's modulus of the nanomaterials. In this study, the analysis was done in the fifth cantilever mode using a lock-in amplifier setup. The choice of using the fifth cantilever mode was due to the fact that the higher modes of oscillation have a more sensitive relationship between a measured frequency change and the change in contact stiffness [5]. This allows for more precise estimation of the mechanical properties of the sample material, which becomes important for small changes such as those seen in the composite material in Figure 2.6.

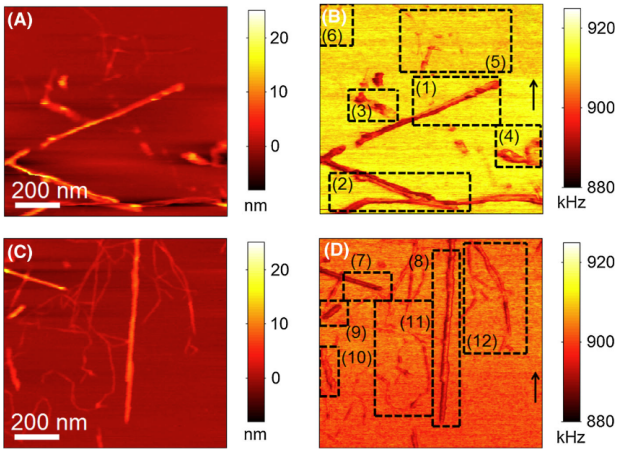


Figure 2.6: AFM contact resonance data on mixed cellulose nanoparticle sample. (a) Topography image of first region, (b) frequency map of the 5th eigenmode of the first region, (c) topography image of second region, (d) frequency map of the 5th eigenmode of the second region. The numbered boxes show areas of the sample where data has been extracted for analysis. The arrows in b and d show the location of jumps in resonance frequency in the slow scan direction. Reproduced with permission from Springer Nature [14].

The results of this study show that the contact resonance method is useful for determining the mechanical properties of differing materials within the same sample, but the accuracy and reliability are not well established, with the major issue being the frequency measured changing with multiple scans. The explanation for this change proposed by the researchers is contamination of CNC particles on the sharp cantilever tip that leads to the effective modulus tending closer to the CNC material [14].

In contrast to these forced techniques, the contact resonance utilised in this thesis is unforced and purely due to thermal oscillations. This technique is relatively new due to the more sensitive electronic equipment and analysis tools required to acquire the thermal signal quickly enough and with low noise [15]. Additionally, accurately fitting to the higher oscillation modes becomes very difficult due to the amplitudes being very small.

The benefit of relying only on thermal oscillations is a simpler experimental setup by not requiring the lock in amplifiers and their modules. This allows AFM machines that would not otherwise be suited for contact resonance experiments to be quickly adapted by simply routing in a fast external data logger. Additionally, analysis can be done quickly with a modern high-end desktop that is able to handle relatively large data sets that even ten years ago would have been very difficult to process. Despite these benefits, the thermal oscillation method has some drawbacks, including reduced accuracy when tracking higher-order modes or a stiff cantilever with higher resonant frequencies. As mentioned above, this method depends on the quality of the data logger used, and any discrepancies in the recording speed and bit resolution of the data logger may give different results even for the same AFM test. This harms the methods repeatability in comparison to the tracking methods where the cantilever is forced, making the oscillation amplitudes larger and much more prominent.

Force Spectroscopy

Force spectroscopy is the most basic and easiest method of performing dynamic AFM. In this test, the cantilever probe is pressed smoothly into and then retracted from the sample at a constant rate. During this process, the cantilever deflects in response to the attractive adhesive force of the sample and the repulsive contact force with the sample. The development of force spectroscopy began as a diagnostic and calibration test in AFM to determine the cantilever sensitivity (Chapter 4.1) but quickly became useful for a variety of tests [16]. An example is to determine the adhesion force (F_a), which can be taken as the pull-off force on the force-distance curve. Through relations such as the Derjaguin approximation, insights into changes in adhesion forces have been explored based on a variety of factors [16].

More recently, the force spectroscopy test has been applied to very soft and delicate biological samples, which has allowed researchers to probe the structure of biological structures and the change in physical properties due to biological processes or environmental changes [17, 18].

As discussed above regarding contact resonance, force spectroscopy is a common method for investigating the variability of mechanical properties in heterogeneous materials. This procedure is done by performing force spectroscopy sweeps over a grid on the sample surface, with a map then being formed through the grid. For example, in Figure 2.7 the results of a force spectroscopy grid test on a carbon fibre composite material are carried out by Mishra et al. [19]. In this work, the Young's modulus of the carbon fibre composite was compared to that of a fresh sample and a sample exposed to ultraviolet (UV) light exposure. By testing on a large grid the effect of UV exposure can be seen depending on the microstructure, with the epoxy resin matrix experiencing much more degradation compared to carbon fibres [19].

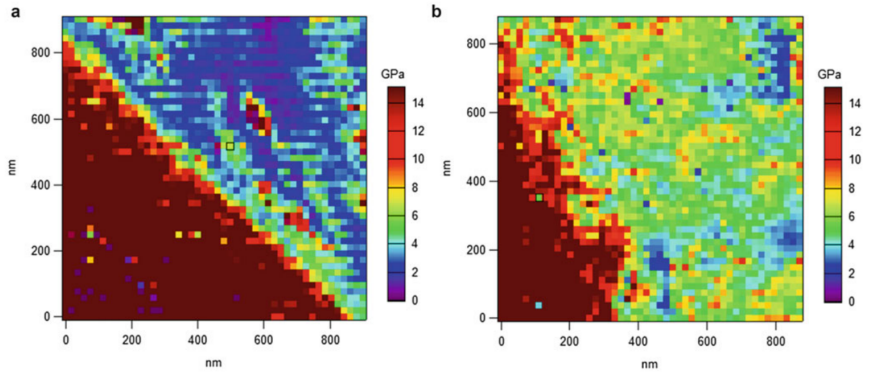


Figure 2.7: Full field elastic modulus map of (a) non-exposed and (b) 6 h UV exposed CFRP sample. Reproduced with permission from Springer Nature [19].

Moving onto the results of force spectroscopy itself, the force-distance curve (Figure 2.8) consists of four main phases, those being:

1. Approach
2. Jump-to-contact (JTC)
3. Contact
4. Pull-off

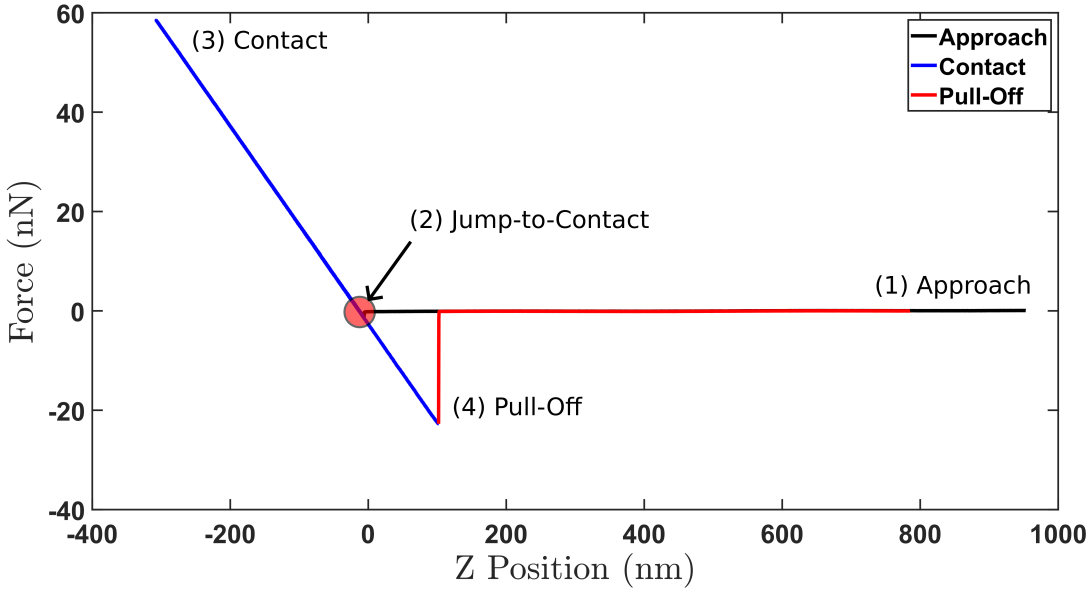


Figure 2.8: Plot showing the full force distance curve in a force spectroscopy sweep. (1) The approach where the cantilever is out of contact and slowly being brought closer to the surface. (2) The Jump-to-Contact (JTC) point. (3) The cantilever is fully in contact and is being pressed into and out of the sample. (4) The pull-off point when the cantilever jumps out of contact. This test was conducted on a HOPG sample with a Silicon contact probe.

Approach

As mentioned in Figure 2.8, the force spectroscopy sweep begins with the cantilever fully out of contact far away from the sample. During the approach, the cantilever is brought closer to the sample by use of the Z-piezoelectric motor. This approach is taken over a relatively small distance ($\pm$ 5μm) and is generally travelled quickly in a few seconds. However, during the force spectroscopy tests conducted in this thesis, the sweeps were generally done at a much slower speed in order to have better time resolution for the changing Z position.

Jump-to-Contact

As the cantilever approaches the sample surface, the long-range adhesive forces between the cantilever and the sample become large enough to deflect the cantilever. This adhesive force starts small but quickly becomes dominant over the natural thermal oscillations of the cantilever. At this point, when the adhesive force becomes much larger than the cantilever reaction force, the cantilever will rapidly be pulled into contact with the surface, generally called Jump-to-Contact (JTC). The critical height at which JTC happens (α_{crit}) depends on several parameters, including the cantilever and sample materials, the stiffness of the cantilever and the environment in which the system is immersed. In an air environment with high relative humidity, the effects of water can greatly increase the adhesive forces, while if immersed in oil or other liquids the adhesive van der Waals forces can be screened out and obscured by the liquid [20]. Through the use of contact mechanics models such as the JKR model, the JTC height can be estimated with high accuracy [20].

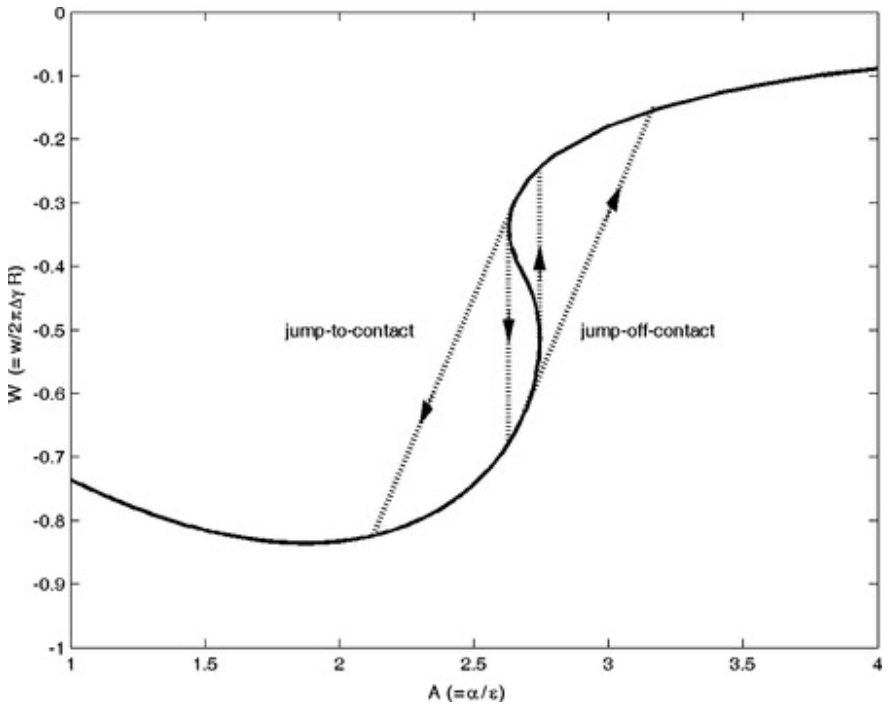


Figure 2.9: The paths for jump-to-contact and jump-off-contact. In an apparatus of finite stiffness, jump-to-contact and jump-off-contact occur when the force gradient exceeds the spring constant of the cantilever. In a fixed-grips device, jump-to-contact and jump-off-contact occur at the vertical tangents of the force-approach curve. Reproduced with permission from Taylor & Francis Journal of Adhesion. Wu et al. [20].

Contact

The third section of the force distance curve is when the cantilever is fully in contact and the tip is first pushed further into the sample and then retracted out. This portion of the curve is when the deflection and Z position change linearly in time, meaning that the cantilever sensitivity can be determined. Another result determined from the contact portion of the curve is the indentation of the sample

(Equation 4.3). This indentation allows for the determination of several factors including Young's modulus through contact mechanics and the determination of the contact stiffness (Chapter 7.1) [21]. This indentation test is a well-established procedure, but certain considerations should be taken depending on the shape of the probe tip and the depth of penetration [22].

Pull-off

Finally, because the cantilever is being pulled from the sample, there is a point where the cantilever would come out of contact if no adhesion was present. In tests where adhesion is present, the cantilever now begins to deflect as the sample is pulled away, but the tip remains in contact. At the point of pull-off, the adhesive forces are equalled by the deflection force, and so the probe tip releases and then rapidly returns to its equilibrium position out of contact. Note that in Figure 2.8 the pull-off force is much larger than the force at the jump to contact. This is due to the adhesive forces becoming stronger once the tip is fully in contact and as the normal force increases [23]. This pull-off force is taken to be the adhesive force (F_a) during the contact mechanic calculations discussed below. This adhesion force has become useful for applications monitoring the wear, size, and shape of the cantilever probe by measuring the pull-off force on scans. From the work of Liu et al. (Figure 2.10) several cantilever probes were scanned and then a force distance curve was performed to measure the adhesion force. Then, through the Derjaguin approximation, the tip radius was estimated and later confirmed through TEM scans and reverse imaging using an ultrananocrystalline diamond sample (UNCD).

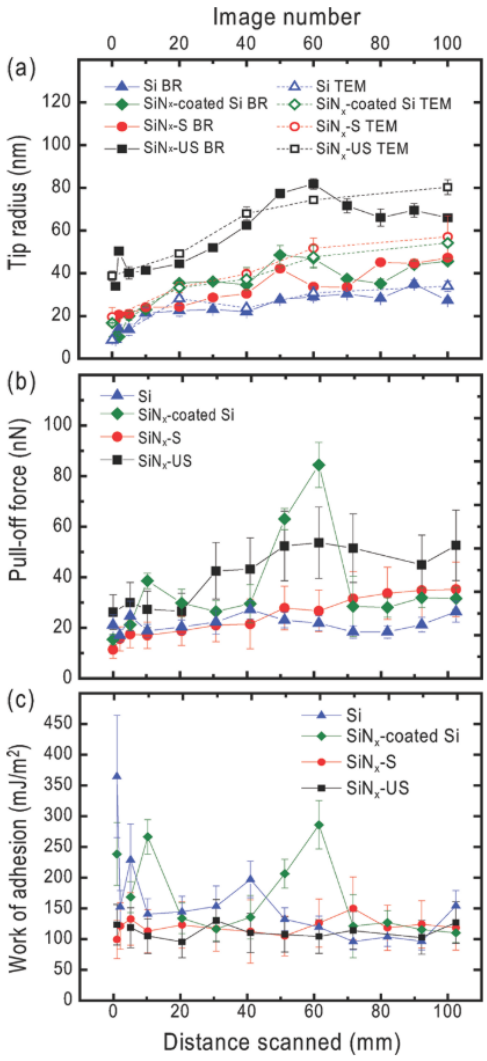


Figure 2.10: Figure 4. Plots of tip radius (a), pull-off force (b), and work of adhesion (c), as a function of distance scanned for the four tips. Reprinted with permission from ACS Nano 2010, 4, 7, 3763–3772 https://doi.org/10.1021/nn100246g. Copyright 2010 American Chemical Society [10].

Incorporating a procedure such as this one is important as the tip size and shape is assumed to be constant across tests but over many scans the probe does undergo wear. In order to accurately measure other mechanical properties careful monitoring of the cantilever probe tip geometry is required.

2.3 Cantilever Stiffness Calibration

Currently, when calibrating the AFM cantilever probe stiffness, two techniques are the most widely used, the thermal noise method [24] and the Sader method [25, 26].

Other methods have been used to determine the stiffness of the cantilever. One such method is the geometric method, by which the stiffness is determined from the dimensions of the cantilever and the Young's modulus of the material [27]. In Equation 2.1 (E) is the Young's modulus, (b) is the cantilever base width, (t) is the cantilever thickness, and (L) is the cantilever length.

$$k_c = \frac{E t^3 b}{4L^3} \tag{2.1}$$

However, the purely geometric method performs poorly due to poor tolerances for the thickness of the cantilever, and compounded by the stiffness scaling to the thickness cubed ($k_c \propto t^3$), the estimated value varies greatly for real manufactured cantilevers. In addition the geometric stiffness assumes the cantilever geometry is constant, while in reality even small deviations in the dimensions can have large impacts on the stiffness [24]. Due to these limitations, most AFM users instead perform a physical calibration to determine each cantilever stiffness value individually.

Thermal Noise Method

Moving on from the largely impractical geometric estimation method, the much improved thermal noise method takes only the cantilever deflection as input. The thermal noise method makes use of the equipartition theorem, where the total kinetic energy of the cantilever is equally shared amongst all degrees of freedom. More specifically, the thermal energy of the first oscillation mode of the cantilever is approximately equal to the mean squared deflection force (Equation 2.2)

$$\frac{1}{2} k_B T = \frac{1}{2} k_c \langle q^2 \rangle \tag{2.2}$$

By simply measuring the natural thermal deflection of the cantilever, the stiffness can be calculated empirically without any knowledge of its geometry or material properties. This method has proven to be accurate and practical and is widely used to calibrate AFM probes. However, all methods have limitations, and the main limitation for the thermal noise method is the accuracy of the AFM hardware. If there is large external noise in the signal, that can introduce errors into the stiffness estimation. Additionally, if the cantilever frequency is very low, it becomes much harder to distinguish the cantilever natural motion from any low-frequency noise present in the system [28].

Sader Method

The final method used to determine the stiffness of the cantilever is the one developed by Dr. John Sader in 1998 [25, 26]. This method works on the basis of the damping of the cantilevers through the Quality factor (Q). As shown in Equation 2.3 the model also incorporates additional damping from the hydrodynamic drag on the cantilever, with $\Gamma_i(\omega_r)$ being the hydrodynamic function.

$$k_c = 0.1906 \rho_f b^2 L Q \Gamma_i(\omega_r) \omega_r^2 \tag{2.3}$$

As with the previously discussed methods, (b) is the width of the cantilever base, (L) is the length of the cantilever, (ρ_f) is the density of the fluid, and (ω_r) is the natural frequency of the cantilever.

When using the Sader method, the frequency spectrum of the cantilever must first be measured. By fitting the Lorentzian distribution to the frequency peak, both the frequency and quality factor can be determined. Then by calculating the Reynolds number of the cantilever based on its frequency, the hydrodynamic drag can be determined (Equation 2.4).

$$Re = \frac{\rho_f \omega b^2}{4\eta} \tag{2.4}$$

The hydrodynamic function used incorporates a correction from the circular case determined analytically (Equation 2.5) for the rectangular cantilever (Equation 2.6). In the circular case, the functions (K_0) and (K_1) are the zeroth and first-order modified Bessel functions of the second kind [26, 29].

$$\Gamma_{circ}(\omega) = 1 + \frac{4i + K_1(-i\sqrt{iRe})}{\sqrt{iRe}\,K_0(-i\sqrt{iRe})} \tag{2.5}$$

$$\Gamma_{rect}(\omega) = \Omega(\omega)\Gamma_{circ}(\omega) \tag{2.6}$$

$$\begin{aligned}\Omega_r(\omega) = (&0.91324 - 0.48274\tau + 0.46842\tau^2 - 0.12886\tau^3 + 0.044055\tau^4 \\ &-0.0035117\tau^5 + 0.00069085\tau^6)(1 - 0.56964\tau + 0.48690\tau^2 - 0.13444\tau^3 \\ &+0.045155\tau^4 - 0.0035862\tau^5 + 0.00069085\tau^6)^{-1}\end{aligned} \tag{2.7}$$

$$\begin{aligned}\Omega_i(\omega) = (&-0.024134 - 0.029256\tau + 0.016294\tau^2 - 0.00010961\tau^3 + 0.000064577\tau^4 \\ &-0.000044510\tau^5)(1 - 0.59702\tau + 0.55182\tau^2 - 0.18357\tau^3 \\ &+0.079156\tau^4 - 0.014369\tau^5 + 0.0028361\tau^6)^{-1}\end{aligned} \tag{2.8}$$

$$\Omega(\omega) = \Omega_r(\omega) + i\Omega_i(\omega) \tag{2.9}$$

$$\tau = \log(Re) \tag{2.10}$$

2.4 Contact Mechanics

In the process of analysing the cantilever response to contact with the surface, one-half of the problem is to understand the response and phenomenon of the tip-sample contact. This requires the inclusion of contact mechanics to connect the contact stiffness of the system (k^*) with the normal force (F_N) and the contact area of the tip (a_c). In this study, the three models of contemporary contact mechanics most applied were considered with those being the Hertz, Derjaguin-Müller-Toporov (DMT), and Johnson-Kendall-Roberts (JKR) models. All three models begin from the same assumptions and only differ in their inclusion and modelling of the adhesive forces between the two surfaces in contact. The main assumptions of the contact models are [30]:

1. The materials are homogeneous
2. Material properties are isotropic in all loading directions
3. The contact is frictionless
4. The stress-strain relationship is completely linear
5. All stresses and strains are fully elastic
6. The surfaces are smooth

Hertz Model

The oldest and simplest contact mechanics model is the Hertz model developed by Heinrich Hertz in 1881 which describes the stress and indentation of two surfaces that contact each other with some force [31].

$$a = \left(\frac{3F_N R_{eff}}{4E*}\right)^{1/3} \tag{2.11}$$

$$\delta = \frac{a_c^2}{R_{eff}} = \left(\frac{9F_N^2}{16R_{eff}E*2}\right)^{1/3} \tag{2.12}$$

$$E^* = \left[\frac{1-\nu_1^2}{E_1} + \frac{1-\nu_2^2}{E_2}\right]^{-1} \tag{2.13}$$

$$R_{eff} = \left[\frac{1}{R_1} + \frac{1}{R_2}\right]^{-1} \tag{2.14}$$

In Equation 2.13 (E_1, E_2) and (ν_1, ν_2) are the Young's moduli and Poisson's ratios for the cantilever and sample materials, while in Equation 2.14 (R_1, R_2) the radius of curvature is the cantilever tip and the sample as well. For a flat surface, Equation 2.14 is simplified to ($R_{eff} = R_{tip}$) since the sample radius is effectively infinite as it is flat.

In the case of the Hertz model, the contact stiffness in the normal direction (k^*) is defined as the change in normal force (F_N) per a change in surface deformation or indentation (δ) (Equation 2.20) [30].

$$k^* = \frac{\partial F_N}{\partial \delta} = 2F_N\sqrt{R_{tip}\delta} = 2aE^* \tag{2.15}$$

In Equation (2.20) the stiffness is not constant and instead increases with increasing load. This is due to the contact area increasing with greater load which results in a greater stress developed in the sample.

Derjaguin-Muller-Toporov (DMT) Model

The Hertz model has been shown to be applicable for many contact cases, but the results lose accuracy when the adhesion forces between the two surfaces become noticeable relative to the normal force applied. This requires the inclusion of adhesive forces in the model. The first and simplest model that implements the adhesive force is the one developed by Derjaguin, Muller, and Toporov (DMT) in 1965 [32] . The main assumption in the DMT model is that the adhesive force acts uniformly throughout the area of contact (a_{DMT}). The result of this assumption is that the adhesion force (F_{ad}) is simply applied as an offset to the normal force in the Hertz model (Equation 2.11)

$$F_{a,DMT} = 2\pi R_{tip} W_{ad} \tag{2.16}$$

$$a_{DMT} = \left(\frac{3(F_N + F_{ad})R_{tip}}{4E*}\right)^{1/3} \tag{2.17}$$

Johnson-Kendall-Roberts (JKR) Model

In the same time period, when the DMT model was being tested, Johnson, Kendall, and Roberts developed a different model that incorporates adhesion, where the adhesive forces are strong relative to the stiffness of the contact. The result of this is that the surface becomes deformed by adhesive forces and much more area comes into contact compared to the Hertz or DMT models [30].

$$F_{a,JKR} = \frac{3}{2}\pi R_{tip} W_{ad} \tag{2.18}$$

$$a_{JKR} = \left[\frac{3R_{tip}}{4E*}\left(F_N + 2F_{ad} + \sqrt{4F_N F_{ad} + 4F_{ad}^2}\right)\right]^{1/3} \tag{2.19}$$

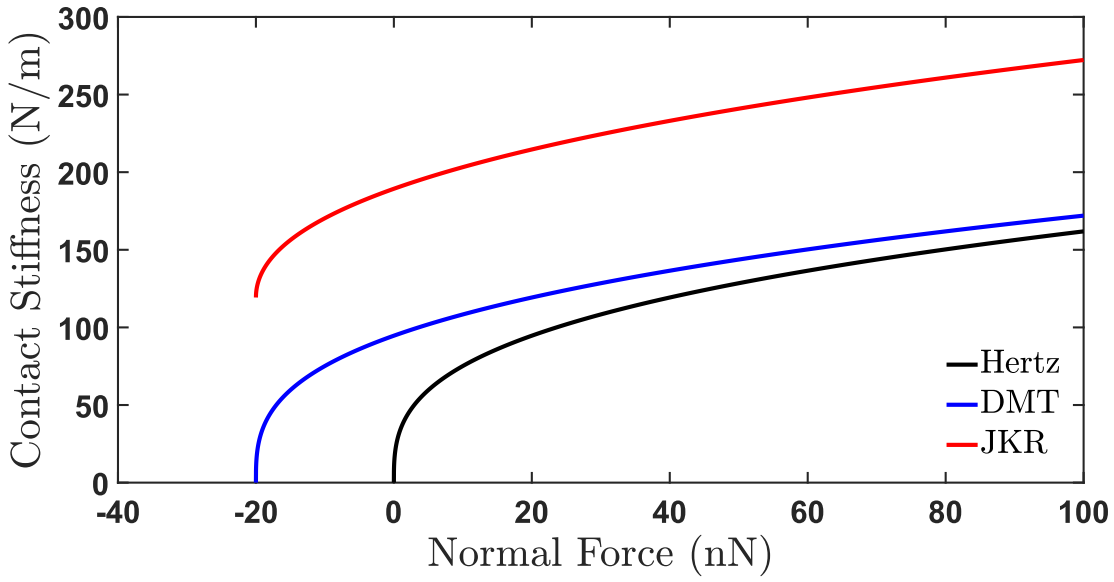


Figure 2.11: Plot showing the three major contact mechanics models; Hertz, DMT, and JKR.

In contact mechanics models, (a) is the radius of contact, (F) is the contact force on the cantilever tip, (F_a) is the adhesive force between the tip and the surface, (E^*) is the effective Young's modulus, and (R) is the radius of the cantilever tip.

$$k^* = 2aE^* \tag{2.20}$$

Vertical contact stiffness (k^*) was included in the contact mechanics model through Hooke's law through Equation 2.20. From Equation 2.20 the contact radius was replaced by ($a = \frac{k^*}{2E^*}$) and the expected contact radius could be estimated for a given set of force and stiffness values. This was done by a nonlinear least squares fit of the contact mechanics models (Equations 2.11,2.17,2.19) converging to a value for the tip radius. In the estimation of the radius of the tip, the adhesive force value (F_a) was taken from the pull-off force in force spectroscopy experiments.

$$R_{Hertz} = \left(\frac{k^*}{2E^*}\right)^3 \left(\frac{4E^*}{3F}\right) \tag{2.21}$$

$$R_{DMT} = \left(\frac{k^*}{2E^*}\right)^3 \left(\frac{4E^*}{3F + F_a}\right) \tag{2.22}$$

$$R_{JKR} = \frac{\left(\frac{k^*}{2E^*}\right)^3 \left(\frac{2E^*}{3}\right)}{\left(F + 2F_a + \sqrt{4FF_a + 4F_a^2}\right)} \tag{2.23}$$

Tabor Parameter

Although both the DMT and the JKR models have uses for modelling adhesive contacts, they are not equally applicable to all surfaces. When they were first developed, researchers considered these models

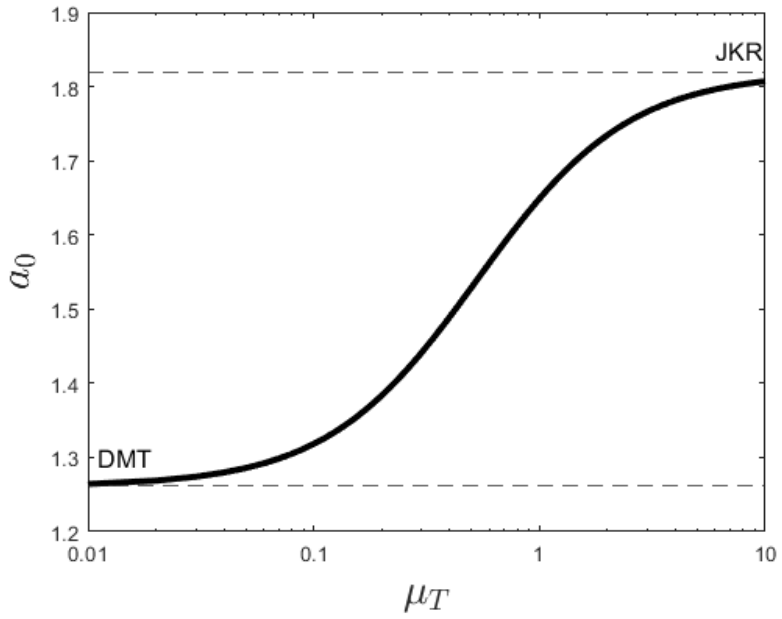


Figure 2.12: Plot of the Tabor parameter with the two outer limits leading to the DMT and JKR contact models.

at odds with each other, where only one could be accurate. However, Tabor and Maugis proved, in fact, that these two models are boundary limits of a larger encompassing model of adhesive contacts, with JKR being the lower limit for surface stiffness and DMT being the upper limit for surface stiffness [33, 34]. In general, Tabor models show that the JKR model is most applicable to soft materials with high adhesion, while the DMT model is applicable to harder materials with lower relative adhesive forces [30]. To quantify the range of contacts applicable between the DMT and JKR models, Tabor developed a dimensionless parameter, the Tabor parameter (μ_T) to characterise any adhesive contact.

$$\mu_T = \left(\frac{R\gamma^2}{E^{*2} z_0^3} \right)^{1/3} \tag{2.24}$$

In Equation 2.24 (z_0) is the equilibrium spacing between the two surfaces. However, this term cannot be accurately measured so the current technique to determine (z_0) is to choose upper and lower limits and then calculate between those. In general the lower limit is taken as the inter-atomic spacing of the sample materials and the upper limit being around 0.5 (nm) [30]. On the lower end the DMT model becomes applicable for values where ($\mu_T \leq 0.1$) while the JKR model is applicable for cases where ($\mu_T \geq 5$) [2]. Any values between 0.1 and 5 give intermediate results in terms of contact radius, deformation, and adhesive force values.

In the results of this thesis the Tabor parameter is not directly included, but its significance is kept in mind. In the analysis of the contact mechanics, the DMT and JKR models are primarily considered because they give the upper and lower bounds for the possible values in an adhesive contact.

Sample Indentation

As mentioned briefly before, one of the applications of contact mechanics in AFM testing is indentation or nano-indentation done through force spectroscopy. The indentation of the tip in the sample is taken as the difference between the cantilever deflection (q) and the position of the sample (Z) ($D = Z - q$). By plotting the normal force (F_N) versus this indentation (D) the mechanical properties of the sample, namely the hardness or Young's modulus, can be estimated. Based on the DMT and JKR models, the force in terms of indentation is described in Equation 2.25 for the DMT case and in Equation 2.26 for JKR.

$$F_N = \frac{4}{3} E^* R^{1/2} D^{3/2} - F_a \tag{2.25}$$

$$D = \frac{2^2}{R} - \frac{4}{3}\sqrt{\frac{a F_a}{R E^*}} \tag{2.26}$$

In Equation 2.26 the term (a) is the contact area under the JKR model shown in Equation 2.19. However, these models discussed all make the assumption of a spherical tip shape where the contact area increases with indentation according to Equations 2.11, 2.17, 2.19. In the case of a flat indenter as first described by the Boussinesq problem solved by Ian Sneddon in 1965, a cylindrical flat punch has the force-indentation relationship modeled in Equation 2.27 [35, 22, 36]. The assumptions of this derivation are that the deformations are infinitesimally small and elastic, the indenter is smooth, and the sample surface is perfectly flat [35].

$$\frac{d F_N}{d D} = \beta \frac{2}{\sqrt{\pi}} \sqrt{A} E^* \tag{2.27}$$

In Equation 2.27 (β) is a shape factor corresponding to the indenter shape (circular = 1) and (A) is the contact area of the indenter where for a circular area $A = \pi R^2$. Different shape factors can be applied for taking into account the precise geometry of the indenter, but this only marginally changes the results with 3.4% and 1.2% change from circular for triangular and square indenters respectively [36]. For a constant contact area using a circular indenter Equation 2.27 can further be simplified down to the result in Equation 2.28.

$$F_N = 2 R E^* D \tag{2.28}$$

Both of these procedures, the spherical case and the flat punch, will be discussed in Chapter 7 when fitting to the experimental data. More information about the flat punch can be found in Appendix 8.4.

2.5 Colloidal Probes

Colloid particle probes are a special subset of cantilever probes in which a small colloid particle is attached to the end of a tip-less cantilever. After the invention of the technique in 1991 by Butt and Ducker, colloid probes have proven to be invaluable for many AFM tests including force testing on soft

biological samples, adhesion testing, and current sensing AFM among others [37, 38, 39]. The broad applicability of colloid probes stems from their variability and advantages over standard silicon probes. Some of these advantages are the wide range of material availability, from soft polymer colloids to hard glass or metal particles, the large variation in the size of the colloid particles, and the ability to change the electrical and chemical properties of the probe-sample contact [39].

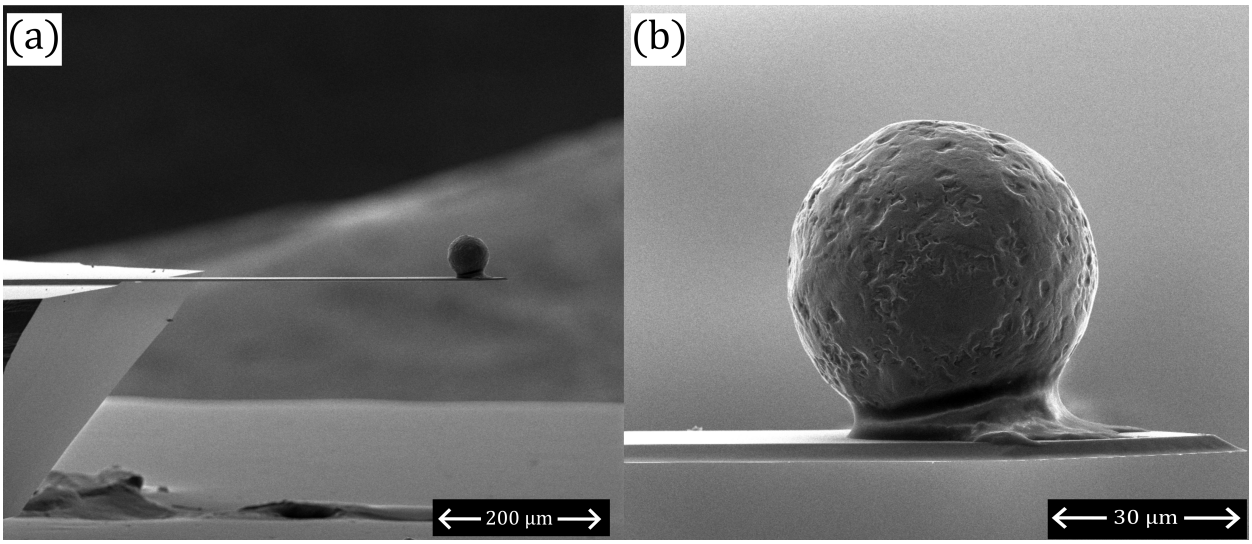


Figure 2.13: Scanning Electron Microscope (SEM) images of a Copper colloid particle used in testing. The Copper particle was glued onto a tip less contact cantilever with a length of 450 (μm) and a width of 50 (μm). Note that particles of this size are so massive that the subsequent cantilever models used are not applicable. For this reason the results from these massive colloid probes are not included in the results. (a) is a side view of the whole cantilever with the Copper particle glued at the end. (b) is zoomed in only on the colloid with the glue at the bottom between the colloid and the cantilever.

When attaching the colloid particle, there are several techniques utilised, with the predominant technique being glue. The colloid probes used in this study used the glue method with details to be discussed later in Chapter 4.3.

As the experimental setup for the tests was discussed (Chapter 4), the use of colloid particle probes was chosen to be included as the colloid probes could help reach a broader set of conditions. The primary uses of the colloid particles are to vary both the size of the contact and the effective hardness of the contact by using different colloid materials.

Chapter 3

Mathematical Background

This chapter describes the mathematical models underpinning cantilever oscillation and dynamics, along with the analytical techniques employed. The project's success hinges on a thorough understanding of the modifications in cantilever oscillations as they approach or come into contact with a surface. In instances where the cantilever tip remains at a significant distance from the surface, the oscillations adopt the nature of a Simple Harmonic Oscillator (SHO). In contrast, when contact is established, the model morphs into the Kelvin-Voigt model, integrating the simple harmonic oscillator (SHO) with the Hertzian contact model [12].

However, this simplified model does not capture every scenario, falling short when the geometric reality of the cantilever and changes in contact stiffness require alterations in the mathematical models. A range of factors merit consideration, including the position of the cantilever tip along its length, the tilt of the cantilever probe within the AFM machine, and the nature of the contact, whether it incorporates lateral forces, and damping.

These variations in cantilever dynamics receive further discussion in Chapter 5, where the data analysis tools utilised remain largely constant across the physical models, underscoring the importance of understanding the nuanced interactions between the cantilever and the surface it encounters.

3.1 Spectral Analysis

The implementation of the spectral analysis was done in order to determine the spectral properties of the cantilever by fitting the thermal resonant peaks of the AFM cantilever in a force curve. These thermal oscillations are modelled through the equipartition theorem [40]. As discussed in Chapter 2.3 according to the equipartition theorem (Equation 2.2), the thermal energy of a system is shared among its various degrees of freedom when in thermal equilibrium. In the case of the cantilever, this has been modeled through a harmonic oscillator, with the stiffness of the cantilever (k_c) represented by a spring [40].

From the mean-square amplitude of the oscillation in Equation 2.2 the spectral density is found and fitted to a Cauchy/Lorentz distribution where some key cantilever parameters can be determined [26].

$$A(f) = \frac{k_B T f_n^3}{\pi Q_n D_n (f^2 - f_n^2)^2 + (\frac{f f_n}{Q_n})^2} \cdot 10^{18} \tag{3.1}$$

In Equation 3.1 for a given oscillation mode (f) is the frequency, (T) is the temperature, ($k_B = 1.3806 * 10^{-23}$ $(m^2 kg s^{-2} K^{-1})$) is Boltzmann's constant, (Q) is the quality factor of the cantilever and (D) is the stiffness of the oscillation mode. The fitting of the cantilever amplitude was done using the non-linear least squares method with the parameters (f), (Q), and (D) being fit.

Fourier Analysis

Almost all frequency analysis begins with Fourier analysis and the Fourier transform. First developed in 1822 by Joseph Fourier to investigate heat transfer, the Fourier transform and analysis method have proven invaluable in fields throughout science and engineering [41]. The main principle behind the transform is to decompose a function or data series from a space or time domain into a function that depends on the spatial or temporal frequency. In terms of time frequencies, an example would be to decompose an acoustic signal in time into frequency, whereby its component frequencies can be found along with their individual amplitudes.

As stated before, the Fourier transform takes any series or function and transforms it into a series of complex sinusoids that when summed together in an inverse transform, recreate the original function. For each calculated frequency, the magnitude gives the amplitude of the sinusoid, and the argument gives the phase offset of that sinusoid [41].

$$X(f) = \int_{-\infty}^{\infty} x(t) e^{-j2\pi f t} \, dt \tag{3.2}$$

The case of a time series or function is given in Equation 3.2 where $X(f)$ is the transformed series, $x(t)$ is the original time series, (f) is a given frequency, and (t) is the time value. This transform is in continuous form, but for a discrete signal, as for the case for a digital signal, a discretised transform must be used instead. The solution to a discretised transform is known as the Fast Fourier Transform (FFT), which has been one of the most important discoveries in modern engineering with countless applications [42].

Short Time Fourier Transform

As stated above, the Fourier transform can only be performed on a whole date series or function, meaning that in the case of time signals, the amplitudes are averaged over the series length. This leads to the limitation that only steady-state signals can be accurately transformed, while time-varying signals must employ a changing analysis method [43]. The short-time Fourier transform (STFT) can overcome this limitation by performing various Fourier transforms along the time signal. The STFT is performed by taking a normal Fourier transform and confining it to a specific time window (Equation 3.4), and then repeating that process over the entire series. As a result, changes in the component frequencies and their magnitudes can be found over time.

In this study, the time window used is a Hanning window, which is the most common windowing function used in the STFT [44]. This windowing function (Equation 3.3) is symmetrical and follows the shape of the cosine function.

$$w(n) = 0.5\left(1-\cos\left(2\pi\frac{n}{N}\right)\right), 0 \leq n \leq N \tag{3.3}$$

$$X_{STFT}(\tau, f) = \int_{-\infty}^{\infty} x(t)g^*(t-\tau)e^{-j2\pi f t}\,dt \tag{3.4}$$

Although the STFT allows for analysis of time-varying signals, one problem is the frequency resolution ($\sigma_{f,STFT}$) across the spectrum is constant, since the time window (N) is constant (Equation 5.2). Because of this limitation to constant time windows and therefore resolution, the newer wavelet transform was also included for testing.

$$\sigma_{f,STFT} = \frac{f_s}{N} \tag{3.5}$$

In use of the STFT the output must be checked to ensure that the transformed spectrum does not have excessive spectral leakage. To quantify this leakage, the (α) parameter introduced by Labuda [28] sets a lower limit to the number of data points required in the resonance peak in order to accurately fit it (Equation 3.6).

$$\alpha = \frac{\pi}{2Q}\frac{f_0}{f_\Delta} \tag{3.6}$$

In equation (3.6) for an effective fit (α) must be at least 6 but ideally it should be larger ($\alpha \gg 1$) with (f_0) being the resonant frequency, (Q) being the quality factor, and (f_Δ) being the frequency resolution. A procedure such as this one discussed to determine the necessary frequency resolution is not currently developed for the wavelet transform.

Wavelet Analysis

The other technique investigated for the spectral analysis is the wavelet transform, which is a much newer and more variable technique when compared to the Fourier transform. The use and application of wavelet analysis to AFM has been growing in recent years, with more interest coming due to its ability to capture transient behaviour and spectral changes that the Fourier methods cannot capture [45]. Beginning in the early 2000s, the wavelet transform has been explored in AFM with advances in computer technology, allowing for use in powerful lab computers. Before that time, the computational requirements were prohibitive for many researchers. Thus far the uses for wavelets in AFM have been qualitative, with the primary application being tracking the change in cantilever modal frequencies when transient behaviour is found. Some examples include the jump-to-contact (JTC) point, pull-off point, and abrupt changes in topography.

For example, when looking at a scalogram of a wavelet transform at the JTC point, the 1st mode of the cantilever gets *dragged* lower and the frequency lowers just before the jump. As shown by [45]

(Figure 3.1) this change in frequency (Δf) can be used to find the tip-sample interaction stiffness and force gradient (k_{ts}) during the jump-to-contact (Equation 3.7). What was found is that just before the attractive forces make the cantilever jump to the surface the tip-sample interaction forces increase, which has the effect of reducing the frequency of oscillation.

$$k_{ts} = k\left(\frac{(f-\Delta f)^2}{f^2} - 1\right) \tag{3.7}$$

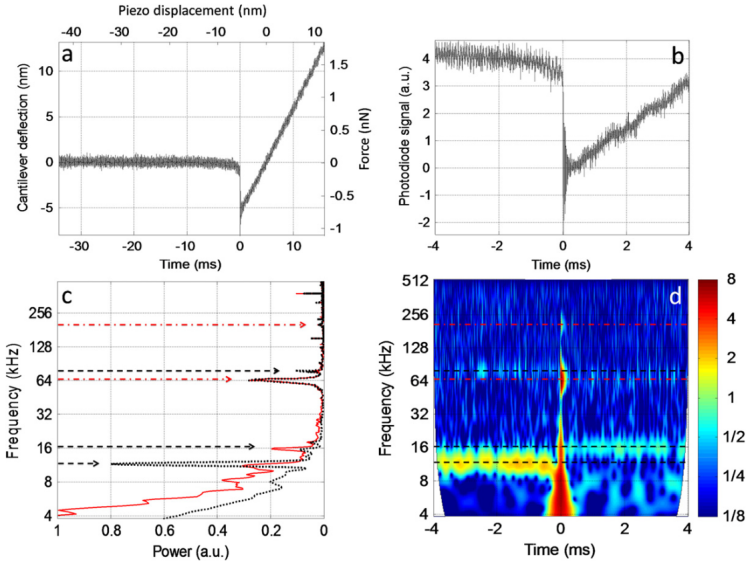


Figure 3.1: (a) Cantilever deflection in force-distance curve. (b) Just before the JTC the cantilever oscillation relaxes and the cantilever deflection down slightly. (c) Fourier transforms of the cantilever deflections in (b). Black line indicate the frequency spectrum before the jump (-2 to 0 ms) while the red line is after the jump to contact (0 to 4ms). (d) Wavelet transform of the deflection data in (b) visualized in a scalogram. The cantilever relaxation just before the jump can be seen here. Reproduced with permission from IOP Nanotechnology 2015 [45].

These results are possible only by using the wavelet transform method as the Fourier or short-time Fourier methods do not have a precise enough time resolution to capture the short-lived frequency shift. The Fourier methods were used to compare the steady-state oscillation frequencies before and after the JTC but not during.

Continuous Wavelet Transform

The wavelet analysis was first developed by building on the Fourier analysis first by Alfred Haar in 1909 and later in the 1930's by Paul Levy [43]. More recently in the 1980's and 90's the wavelet analysis was found to be useful in the frequency analysis for non-stationary systems and fast acquisition times. Even more recently the use of wavelets has started to be applied data analysis for AFM [46].

As mentioned above, the wavelet analysis was built upon the Fourier analysis, but where the Fourier analysis can only be done over the whole time series using sine/cosine curves, the wavelet analysis has

more freedom over the time and analysing function [43]. The major limitation of the Fourier transform (can only be used over the whole time series) can be partially solved by the use of the short-time Fourier transform (STFT). In this STFT the Fourier transform is applied over smaller windowed regions of the time series.

This is seen in equation 3.4 as the STFT is simply the FT equation 3.2 multiplied by the windowing term $g(t)$. This windowing gives the frequency spectrum for the windowed regions which can be applied to time varying signals, which as discussed the Fourier analysis cannot do [47]. However, it is important to note that the size of the window drastically changes the performance of the technique [43]. Short windows give high time resolution (Δt) but poor frequency resolution (Δf), and vice versa. This property is quantified by the Heisenberg inequality (Equation 3.8) of quantum mechanics fame [48].

$$\Delta t \Delta f \geq \frac{1}{4\pi} \tag{3.8}$$

This property has made the STFT useful in many applications with non-stationary systems, but there are still some limitations to the STFT. The biggest limitation is that choosing the windowing time correctly can be difficult and the analysing function is still in the form of sine curves. The wavelet transform method further improves this by being able to change the width of the window as a function of frequency, and the analysis function can be customised to be better tailored for the signal [48].

The wavelet transform (WT) differs from the STFT in that the analysis function is a small wave instead of sine curves [48] denoted by $\Psi(t)$. One of the most common wavelet functions is the Morlet or Gabor wavelet (Figure 3.2, Equation 3.9) which is a complex sine signal bounded by a Gaussian window [48]. The wavelet function in general can be a system of sine curves, but not necessarily. For the Morlet wavelet it is composed of two sine functions applied over a Gaussian window, but there are other wavelet functions that are not sinusoidal and can be other shapes such as square, triangular, or sawtooth functions [48].

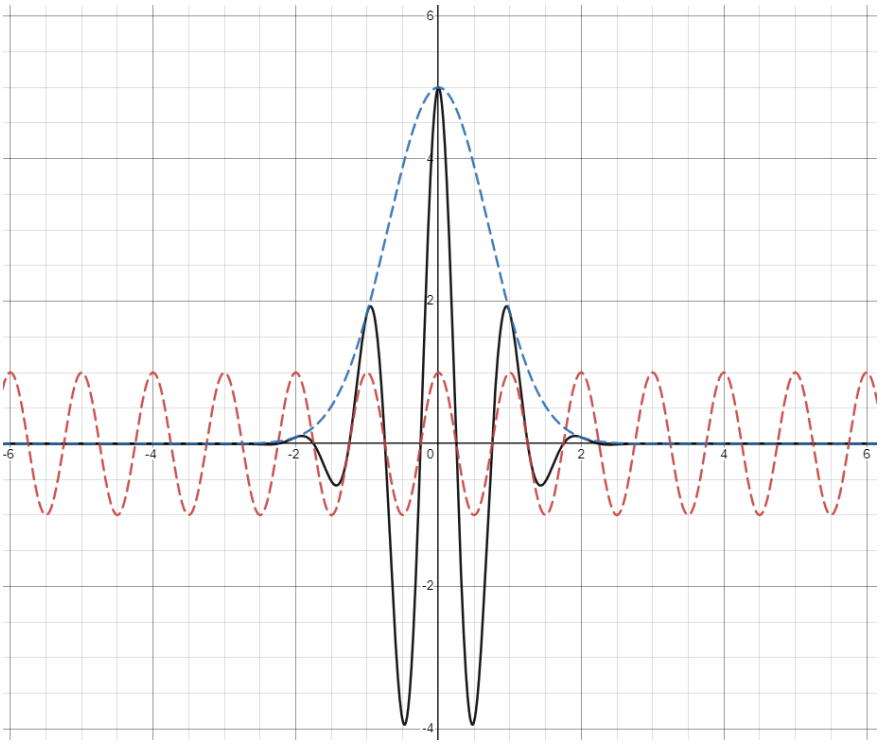


Figure 3.2: An example of the Morlet wavelet (black). The wavelet is formed by a standard sinusoidal wave (red) bounded by a Gaussian envelope (blue).

$$\Psi(t) = \frac{1}{(\sigma^2\pi)^{1/4}} e^{\frac{t^2}{2\sigma^2} + j\eta t} \tag{3.9}$$

In the Morlet wavelet (σ) is the time spread factor and (η) is the centre frequency. This wavelet function $\Psi(t)$, also called the mother wavelet, is then applied to the transform with the included time translation (τ) and the scale parameter (s) [43].

$$X_{WT}(\tau, s) = \frac{1}{\sqrt{|s|}} \int_{-\infty}^{\infty} x(t)\Psi^*\left(\frac{t-\tau}{s}\right) dt \tag{3.10}$$

The mother wavelet function can also be modified throughout the frequency range to better fit the data. These new wavelets, called daughter wavelets, are created through the use of the Gabor shaping factor ($G_s = \sigma\eta$) [49]. The shaping factor alters the time and frequency resolution of the wavelet, which then determines the dimensions of the Heisenberg box as visualised in Figure 3.3. Choosing the correct shaping factor for each time period is paramount to obtain useful results, as throughout the measurement period different frequency resolutions are needed to calculate the frequency resolution (Δf) over the period.

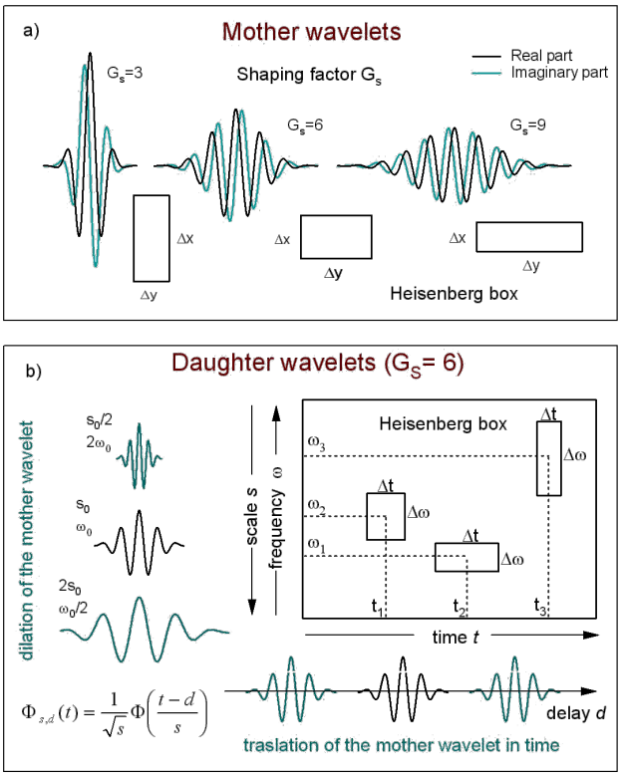


Figure 3.3: a) The complex Morlet or Gabor mother wavelet at different shaping factors shown with the corresponding Heisenberg boxes showing the time and frequency uncertainty. b) Time delay and translation transforms that can be applied to a daughter wavelet in the wavelet transform. Reproduced with permission from Beilstein J. Nanotechnology 2010, 1, 172–181. https://doi.org/10.3762/bjnano.1.21, © 2010 rights holder [50].

The major benefits of using the wavelet transform method is being able to measure non-stationary systems (i.e. changes with time) and that acquisition times can be much faster compared to the time required for the Fourier analysis [50]. Despite these apparent advantages, there are some trade-offs when using wavelets, such as the more computations required for a given data set and the challenges associated with the frequency resolution changing through the frequency spectrum. Some of these trade-offs are discussed along with the results in Chapter 5.

The other major parameter in controlling the wavelet transform is the number of frequency scales or voices per octave. As in music and acoustics, an octave is defined as a doubling of frequency with the number of voices being equal for all octaves. This means that the frequency scaling for the wavelet transform follows a (log_2) scale with more frequency scales for voices at higher frequencies (Equation 3.12). This scaling varies from the STFT where the frequency scales are evenly spaced throughout the spectrum (Fig.3.4) [43].

$$s = 2^{\frac{1}{NV}} \tag{3.11}$$

$$\sigma_{f,CWT} = \frac{S_0(2^{\frac{1}{NV}})^j}{N} \tag{3.12}$$

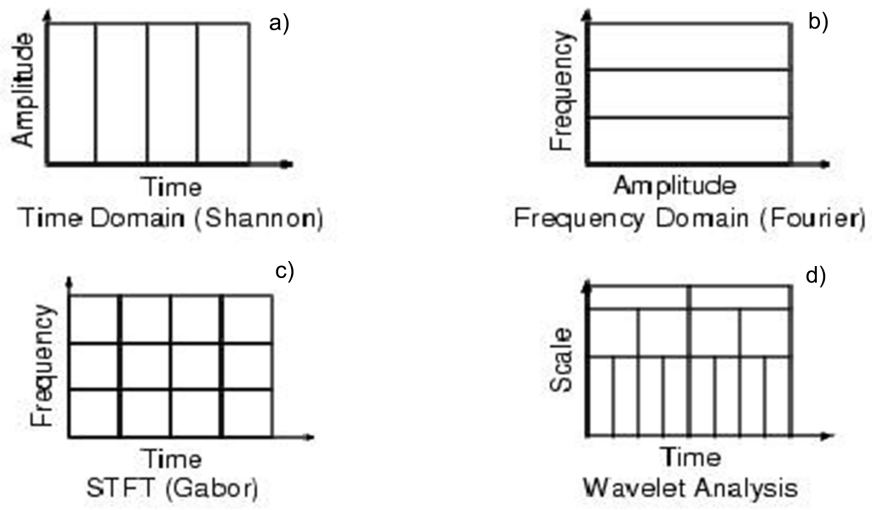


Figure 3.4: Time and frequency scaling for different transforms. a) The Time Domain is shown with the higher possible time resolution. b) The Fourier Domain is shown having the highest possible frequency domain. c) The STFT is shown with a statically windowed time and frequency resolution. d) The Wavelet Transform is shown with a dynamically changing time and frequency resolution. Reproduced with permission from Springer Nature [43].

Where $(S_0 = \frac{\omega'_x}{\pi})$ is the minimum scale size with (ω'_x) being the peak frequency of the signal, (NV) is the number of voices (frequency scales) per octave, (j) is the scale number, and (N) is the length of the signal.

The major benefit of wavelet scaling is that there is greater frequency resolution at high frequencies and better time frequency at low frequencies. This allows the transform to accurately capture both the low and high frequencies while a given STFT window size can fit perfectly for a specific frequency.

This property of the wavelet transform is particularly useful as low frequency components require good time resolution while high frequency components need high frequency resolution. This allows for greater probing into the spectral changes of the time signal through time compared to the Short Time Fourier Transform at a given data sampling rate. However, there are several difficulties when using the Wavelet transform. One major downside is the computational work required to compute the wavelet transform.

When computing the STFT, the process is to perform a Fast Fourier Transform (FFT) on each windowed portion of the time signal. This means that for (N) time windows there are (N) FFT's required. However, for the Wavelet Transform at every time data point for (M) frequency scales there must be (M) convolutions performed. This result means that for a given data set, the wavelet transform will require far more computations [43]. For example on a time series containing 1,000,000 data points, a STFT with a window size of 1,000 points will require $(N_{FFT} = \frac{1{,}000{,}000}{1{,}000} = 1{,}000)$ individual FFT's to be performed while the wavelet transform would require a convolution at every data point $(N_{CWT} = 1{,}000{,}000)$. These extra computations mean that more higher frequency data can be gained from the CWT compared to a single STFT window size but this is traded off with poorer frequency resolution at low frequencies. The results comparing the STFT and CWT techniques will be discussed in Chapter 5.

3.2 Cantilever Dynamics

Departing from the spectral analysis, the cantilever dynamics focuses on modeling the motion of the cantilever and relating the observed frequency to the stiffness of the cantilever and contact. In this section, the outputs of the cantilever models are in terms of frequency (f), quality factor (Q), and stiffness (k^*, k_c). By fitting the Lorentz distribution (Equation 3.1) using the spectral techniques, the raw deflection data can be connected to the cantilever models.

Harmonic Oscillator

Analysing any system generally starts with the most simplified case which can be clearly modelled and verified before moving towards a more realistic but intricate model. In the case of oscillating system, this simplified model is that of an undamped simple harmonic oscillator (SHO). The SHO is visualised by a mass (m) attached to a constant linear spring (k), which is then fixed at one end. Starting from Hooke's law ($F = k\Delta x$) and then applying Newton's second law ($F = ma$) the equation of motion is generated by solving the equation in terms of the position as a function of time $x(t)$ [8].

$$F = ma = m\frac{d^2x}{dt^2} = -k\Delta x \tag{3.13}$$

By solving the above equation 3.13 the equation of motion is as follows, where in the solution (A) is the amplitude of the oscillation, ($\omega = \sqrt{k/m}$) is the resonant frequency of the oscillator, and (ϕ) is the phase of the oscillation.

$$x(t) = A\cos(\omega t + \phi) \tag{3.14}$$

Point Mass Model

When beginning to describe the cantilever motion, the most basic model is the point-mass model where the actual dimensions and geometry of the cantilever are ignored and it is simple modeled as a harmonic oscillator as described above [8]. In this model, the resonant frequency of the harmonic oscillator (ω_0) is taken to be the frequency of the cantilevers first mode when free (out of contact) ($\omega_{1,free}$).

$$\omega_{1,free} = \sqrt{\frac{k_c}{m^*}} \equiv \omega_0 \tag{3.15}$$

Where in equation 3.15 (k_c) is the cantilever stiffness which can be determined through the different methods as discussed in Chapter 2.3. The term (m^*) represents the effective mass which for rectangular cantilevers is calculated in equation 3.16.

$$m^* = \frac{k_c}{\omega_{1,free}^2} = \frac{3\rho_c Lwb}{(\alpha_{1,free}L)^4} \approx \frac{1}{4}m \tag{3.16}$$

Now using the point-mass model, the equation of motion can be generated at the end of the cantilever along its length ($x = L$) when out of contact [8].

$$m^* \ddot{y}(L,t) + m^* \eta_{Air} \dot{y}(L,t) + k_c\, y(L,t) = 0 \tag{3.17}$$

When the cantilever then comes into contact with the surface the resonant frequency shifts due to new tip-sample forces coming into effect [4]. This force adds a second spring stiffness, being the contact stiffness (k^*), which has the following change.

$$\omega = \sqrt{\frac{k^* + k_c}{m^*}} = \omega_0 \sqrt{1 + \frac{k^*}{k_c}} \tag{3.18}$$

From the above equations the point mass model is quite useful for quick and simple characterization of the cantilever probe [8]. However, the point-mass breaks down once the contact stiffness (k^*) approaches the same order of magnitude of the cantilevers stiffness (k_c) [8]. Figure 3.5 shows this breakdown where the point-mass model only remains accurate at very low contact stiffness values.

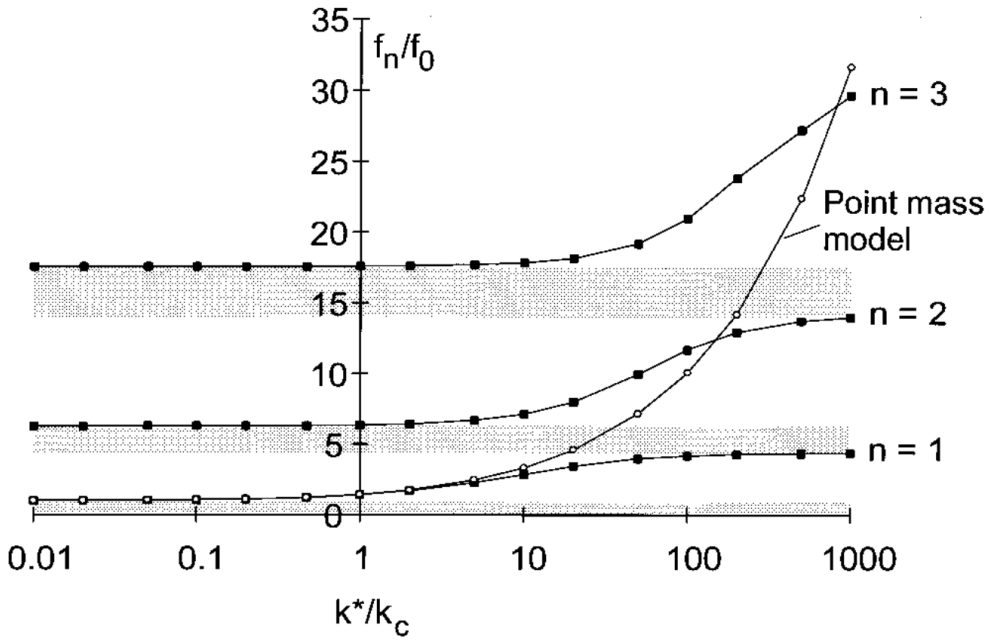


Figure 3.5: Plot of the dispersion relation between normalized frequency (f_n/f_0) and normalized stiffness (k^*/k_c) comparing the point mass model and the spring coupled cantilever (Figure 3.6). Reprinted from U. Rabe, K. Janser, W. Arnold; Vibrations of free and surface-coupled atomic force microscope cantilevers: Theory and experiment. Rev Sci Instrum 1 September 1996; 67 (9): 3281–3293. with the permission of AIP Publishing [4].

Rectangular Cantilever

Moving forward from the basic harmonic oscillator model, once the material and geometric properties of the cantilever are included, a more comprehensive theory is needed. In the case of this thesis, the following cantilever models are all derived from the ubiquitous Euler-Bernoulli beam theory first formulated by Bernard Euler in 1750 [51]. In this theory, the cantilever deflections are estimated by applying linear elastic deformation theory from continuum mechanics.

$$\frac{d^2}{dx^2}\left(EI\frac{d^2y}{dx^2}\right)=q \tag{3.19}$$

Free (Out of Contact) Cantilever

From a theoretical perspective, the analysis of a rectangular cantilever begins with the dynamics of its motion and oscillations depending on the conditions of the system, whether in contact or free. The study of the cantilever motion first begins with the consideration of the cantilever as a Simple Harmonic Oscillator (SHO), with the model being visualised as a simple spring-mass system. By incorporating the elastic deformations of the Euler-Bernoulli beam theory, a simple equation of motion can be generated [8].

$$EI\frac{\partial^4 y}{\partial x^4}+\rho A\frac{\partial^2 y}{\partial t^2}=0 \tag{3.20}$$

Where (E) is the Young's Modulus, (ρ) is the density, $(A=ab, a=width, b=thickness)$ is the cross sectional area of the cantilever, $(I=\frac{ab^3}{12})$ is the moment of inertia for a rectangular cantilever, and (y) is the deflection of the cantilever from its equilibrium at position (x) along the length of the cantilever. $(\frac{\partial y}{\partial x})$ is the slope of the cantilever, $(\frac{\partial^2 y}{\partial x^2})$ is the moment, and $(\frac{\partial^3 y}{\partial x^3})$ is the shear force. A general solution of equation 3.20 in terms of (y) is in the form of Equation 3.21.

$$y(x,t)=(a_1e^{kx}+a_2e^{-kx}+a_3e^{ikx}+a_4e^{-ikx})e^{-iwt} \tag{3.21}$$

With the wave number $(k=\frac{2\pi}{\lambda})$ and the angular frequency $(\omega=2\pi f)$ can be calculated by inserting Equation 3.21 into 3.20 which then gives the dispersion relation for the beam.

$$EIk^3-\rho A\omega^2=0 \tag{3.22}$$

In order to arrive at the final solution of the cantilever the boundary conditions for the end positions of the cantilever must be known. In the case when the cantilever is out of contact the end positions are clamped at the cantilever base and free at the cantilever end. This means at the base of the cantilever $(x=0)$ the forces and deflection are zero while at the end of the cantilever $(x=L)$ these forces can be present.

$$y=0, \frac{\partial y}{\partial x}=0, \text{when } x=0 \tag{3.23}$$

$$\frac{\partial^2 y}{\partial x^2}=0, \frac{\partial^3 y}{\partial x^2}=0, \text{when } x=L \tag{3.24}$$

These boundary conditions are substituted into the general solution (Equation 3.21) and its derivatives and then solved for the coefficients (a_i). The characteristic equation for the free cantilever then comes out to the form found in Equation 3.25.

$$\cos(k_nL)\cosh(k_nL)+1=0 \tag{3.25}$$

This characteristic equation must be fulfilled for any solution of the wave numbers ($k_n L, n = 1, 2, ...$) where (n) is the mode number of the cantilever.

Model 1: Spring-Coupled (In Contact) Cantilever

When the cantilever goes into contact, the boundary conditions at the end of the cantilever ($x = L$) change from free to spring-coupled. This change allows for a reaction force with the surface to be transmitted through the tip ($-k^* y$) that is added to the internal shear forces of the cantilever. This results in a new system configuration that must be solved for as shown in Figure 3.6.

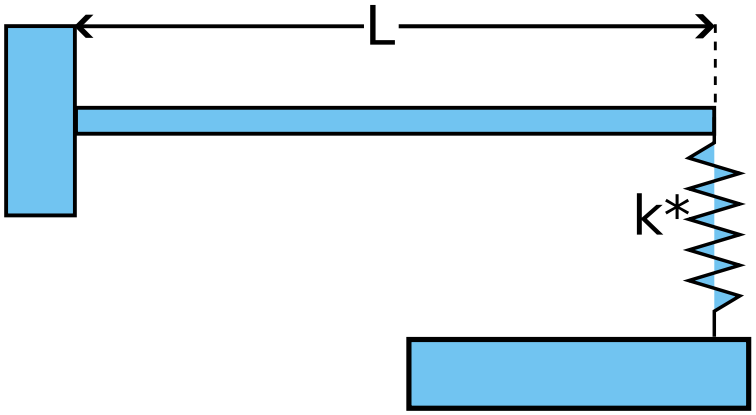


Figure 3.6: Schematic of the spring-coupled cantilever with the tip-sample contact at the cantilever end.

$$k^* = -\frac{\partial F(\delta)}{\partial \delta}\bigg|_{\delta=\delta_e} \tag{3.26}$$

$$EI\frac{\partial^3 y}{\partial x^3} - k^8 y = 0 \tag{3.27}$$

After incorporating the changes to the system discussed above (Equations 3.26,3.27) the new boundary conditions for the cantilever when in contact are those in Equation 3.28.

$$\frac{\partial^2 y}{\partial x^2} = 0, \frac{\partial^3 y}{\partial x^3} = \frac{k^*}{EI} y = \frac{3k^*}{k_c L^3} y, \text{when } x = L \tag{3.28}$$

The solution for the new boundary conditions in equation 3.28 is done using the general solution in the form of Equation 3.29.

$$y(x) = A(\cos(kx) + \cosh(kx)) + B(\cos(kx) - \cosh(kx)) + C(\sin(kx) + \sinh(kx)) + D(\sin(kx) - \sinh(kx)) \tag{3.29}$$

After substituting the general solution and its derivatives into the boundary conditions for the in contact cantilever the characteristic solution is found in Equation 3.30.

$$\sinh(k_n L)\cos(k_n L) - \sin(k_n L)\cosh(k_n L) = \frac{(k_n L)^3 k_c}{3k^*}(1 + \cos(k_n L)\cosh(k_n L) \tag{3.30}$$

Equation 3.30 can now model the whole system when free or in contact with the surface. If the cantilever is out of contact the contact stiffness (k^*) goes to zero and now reduces to equation 3.25 while if the contact approaches the pinned condition ($k^* \to \infty$) the model simplifies down to Equation 3.31

$$\sinh(k_n L)\cos(k_n L) - \sin(k_n L)\cosh(k_n L) = 0 \tag{3.31}$$

By varying the ratio of the contact stiffness to the cantilever stiffness (k^*/k_c) the dispersion of the frequency ratio when in contact vs out of contact (f/f_0) can be calculated analytically (Figure 3.8). In the experimental analysis however, this solution process is reversed. Where the frequency dispersion is calculated through the Fourier analysis and the contact stiffness is estimated through the cantilever models.

The Figure 3.7 shows the possible boundary conditions for the cantilever when in comes into contact. These changes in boundary conditions have the effect of changing the interaction stiffness between the tip and the sample surface, which then alters the natural frequency of the cantilever.

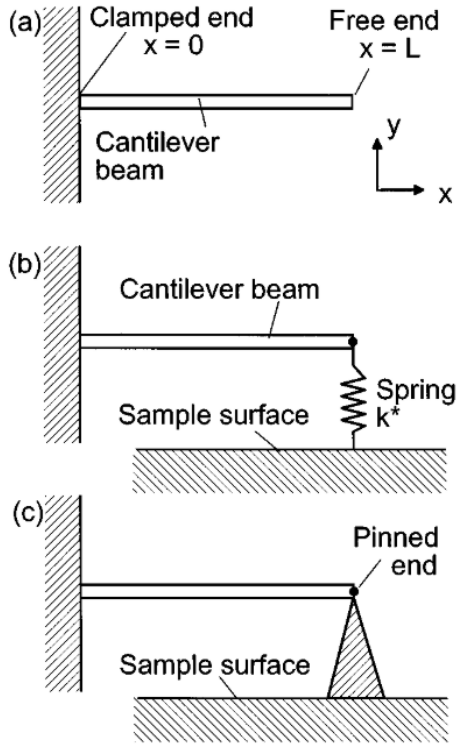


Figure 3.7: Boundary conditions of an AFM cantilever with uniform cross section: (a) Clamped-free cantilever, (b) clamped spring-coupled cantilever, (c) clamped-pinned cantilever. Reprinted from U. Rabe, K. Janser, W. Arnold; Vibrations of free and surface-coupled atomic force microscope cantilevers: Theory and experiment. Rev Sci Instrum 1 September 1996; 67 (9): 3281–3293. with the permission of AIP Publishing [4].

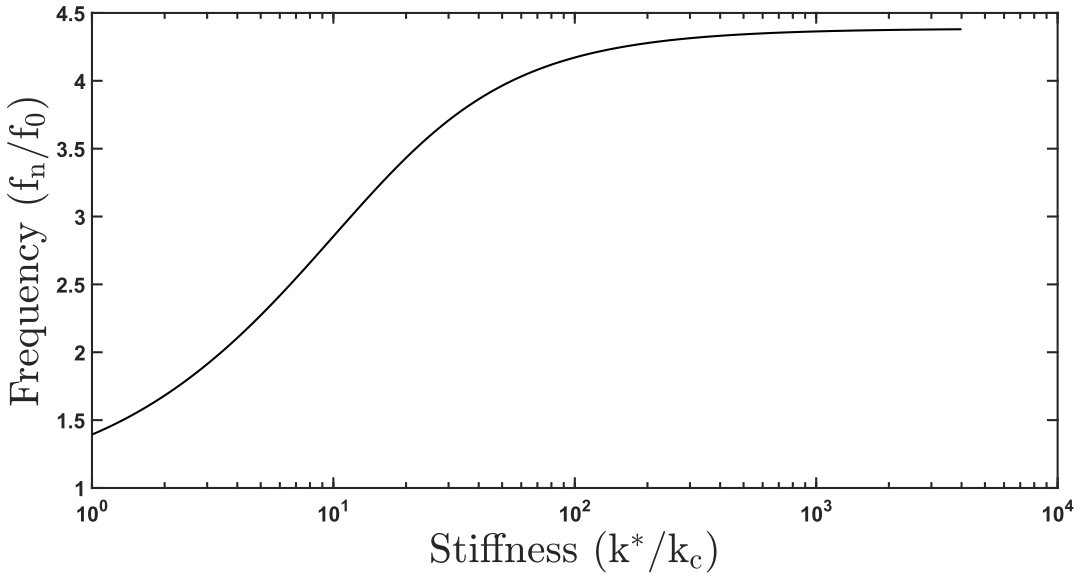


Figure 3.8: Dispersion relation of normalized frequency (f/f_0) vs normalized stiffness (k^*/k_c) for the 1st mode in Model 1 (Figure 3.6).

Model 2: Considering Tip Position

The simple idealised cantilever model should fit for a perfectly rectangular cantilever, but it diverges from the experimentally measured values. This is because this basic model does not take into account the different geometric attributes of the cantilever. The fastest attribute to account for the positioning of the tip along the length of the cantilever. The basic model in 3.30 assumes that the tip is positioned at the end of the cantilever, but in reality the tip is always set back from the end. This position is generally around 5% of the total length of the cantilever, but varies slightly due to manufacturing tolerances [4, 3]. To take this positioning into account, the total cantilever length is divided into two sections. The first section extends from the clamped base ($x = 0$) to the tip of the cantilever ($x = L_1$). The second section extends from the tip of the cantilever ($x' = 0$) to the end ($x' = L'$) with the total length of the cantilever being ($L = L_1 + L'$). In this new set-up the second section begins at the cantilever tip where ($x' = 0$) to simplify the solution process. This updated cnatilever geometry is shown in Figure 3.9.

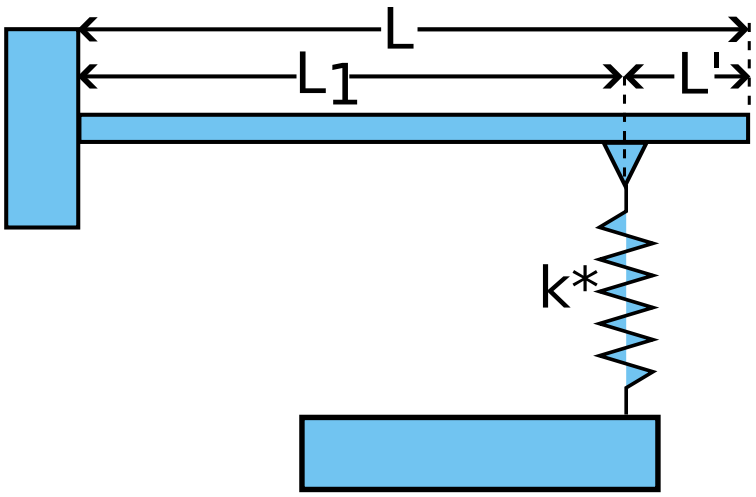


Figure 3.9: Schematic of the spring-coupled cantilever with the tip-sample contact located at the accurate cantilever tip position.

The boundary conditions for the two sections follow closely from the previous cantilever from Equations 3.23 and 3.24. The displacements for the two sections are ($y(x)$) for the first section stretching from the base to the tip and ($y'(x')$) for the second section stretching from the free end of the cantilever to the tip. Similarly to the previous model, the new boundary conditions are as follows.

$$y(x)=0, \frac{\partial y}{\partial x}=0, \text{when } x=0 \tag{3.32}$$

$$\frac{\partial^2 y'}{\partial x'^2}=0, \frac{\partial^3 y'}{\partial x'^3}=0, \text{when } x'=0 \tag{3.33}$$

In Equation 3.32 are the boundary conditions for the clamped base of the cantilever while 3.33 are the boundary conditions for the free end of the cantilever.

The complete system configuration can be solved by solving the two sections separately and then connecting them at the point ($x=L_1=x'=L'$). However, in the current setup with the contact being modelled by a spring, the solution becomes quite lengthy, so the solution can be simplified by solving the boundary case when the contact becomes pinned ($k^* \to \infty$) and then returning to the spring-coupled cantilever. The boundary condition at the tip of the cantilever becomes ($y=y'=0, \text{when } x=L_1=x'=L'$). Now the general solution cab be applied to the two sections of the cantilever as:

$$y(x)=B(\cos(kx)-\cosh(kx))+D(\sin(kx)-\sinh(kx)) \tag{3.34}$$

$$y'(x')=A'(\cos(kx')-\cosh(kx'))+C'(\sin(kx')-\sinh(kx')) \tag{3.35}$$

The general solutions in Equations 3.34 and 3.35 can be rearranged to solve for the unknown solution constants.

$$\frac{B}{D}=-\frac{\sin(kL_1)-\sinh(kL_1)}{\cos(kL_1)-\cosh(kL_1)} \tag{3.36}$$

$$\frac{A'}{C'}=-\frac{\sin(kL')-\sinh(kL')}{\cos(kL')-\cosh(kL')} \tag{3.37}$$

Now to connect the two solutions the boundary cantilever bending and forces must be equal at the tip position. The following conditions satisfy this requirement.

$$\frac{\partial y}{\partial x}(L_1) = \frac{\partial y'}{\partial x'}(L') \tag{3.38}$$

$$\frac{\partial^2 y}{\partial x^2}(L_1) = \frac{\partial^2 y'}{\partial x'^2}(L') \tag{3.39}$$

Note that in Equations 3.34 and 3.35 the third derivatives are not necessarily equal because the forces experienced on either side of the cantilever probe tip can and do differ. However, this can be ignored because any force differentials are supported by the tip in this case or the spring in general. The final solution for the cantilever under the pinned condition can be found by taking the derivatives of the characteristic Equations 3.34 and 3.35 and substituting them into the conditions in Equations 3.38 and 3.39.

$$\begin{aligned}(\cosh(k_n L_1)\sin(k_n L_1) - \sinh(k_n L_1)\cos(k_n L_1)(1+\cos(k_n L')\cosh(k_n L')) \\ -(\cosh(k_n L')\sin(k_n L') - \sinh(k_n L')\cos(k_n L'))(1-\cos(k_n L_1)\cosh(k_n L_1)) = 0\end{aligned} \tag{3.40}$$

To get the general solution for the cantilever when in contact the free case and pinned case need to be coupled together. This coupling factor is taken from the standard cantilever in Equation 3.30 where only now ($L = L_1 + L'$). From Equation 3.30 the coupling factor is $(\frac{(k_n L)^3 k_c}{3k^*}(1+\cos(k_n L)\cosh(k_n L))$, but now an additional constant must be applied, as shown in Equation 3.41.

$$\begin{aligned}(\cosh(k_n L_1)\sin(k_n L_1) - \sinh(k_n L_1)\cos(k_n L_1))(1+\cos(k_n L')\cosh(k_n L')) \\ -(\cosh(k_n L')\sin(k_n L') - \sinh(k_n L')\cos(k_n L'))(1-\cos(k_n L_1)\cosh(k_n L_1)) \\ = A k_n^3 \frac{EI}{k^*}[1+\cos(k_n(l_1+L'))\cosh(k_n(L_1+L'))]\end{aligned} \tag{3.41}$$

Finally the last step is to solve for the constant (A) which is done by taking the distance from the probe tip to the end to zero ($L' \to 0$) and then equating this to the existing solution for a cantilever with the tip at the end (Equation 3.30). The only answer for (A) that equates Equations 3.41 and 3.30 is ($A = -2$), which gives the final general solution for the cantilever set back from the end (Equation 3.42). In Figure 3.10 this updated dispersion relationship is shown. The major difference between this model and the first model is the higher frequency shift observed when approaching the pinned boundary condition.

$$\begin{aligned}-(\cosh(k_n L_1)\sin(k_n L_1) - \sinh(k_n L_1)\cos(k_n L_1))(1+\cos(k_n L')\cosh(k_n L')) \\ -(\cosh(k_n L')\sin(k_n L') - \sinh(k_n L')\cos(k_n L'))(1-\cos(k_n L_1)\cosh(k_n L_1)) \\ = 2k_n^3 \frac{EI}{k^*}[1+\cos(k_n(l_1+L'))\cosh(k_n(L_1+L'))]\end{aligned} \tag{3.42}$$

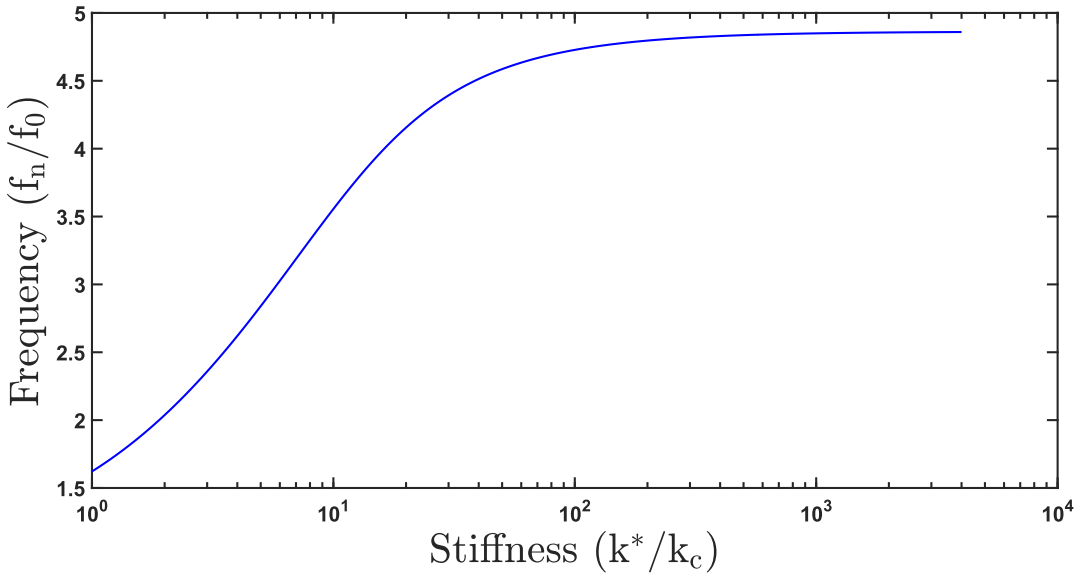


Figure 3.10: Dispersion relation of normalized frequency (f/f_0) vs normalized stiffness (k^*/k_c) for the 1st mode in Model 2 (Figure 3.9).

Model 3: Considering both Vertical & Lateral Forces

The third model considered in this study is one that expands on the previous two models, with the cantilever tip at the end (Equation 3.30) and the cantilever tip being set back from the end (Equation 3.42) [4]. This third model now considers the situation where the cantilever motion is not only vertical, but can also translate laterally as the tip is pressed into the surface. This model is visualised by the schematic shown in Figure 3.11 below.

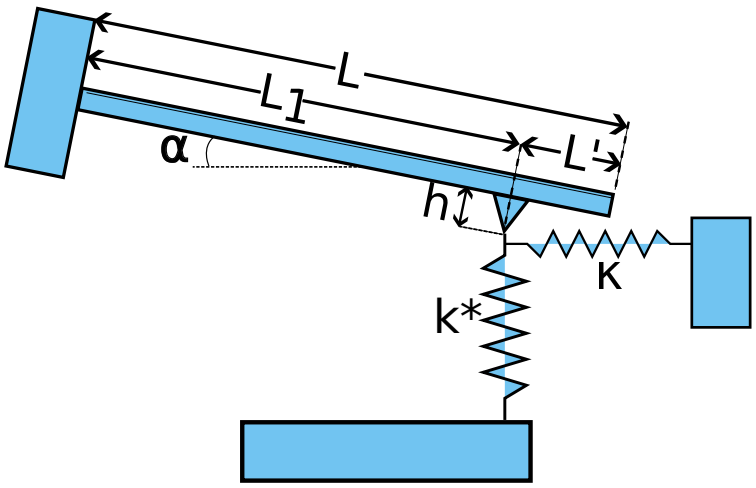


Figure 3.11: Schematic of the spring-coupled cantilever with the tip-sample contact located at the accurate cantilever tip position and including lateral forces.

In this model in addition to the normal contact stiffness spring there is another spring that accounts

for the lateral stiffness of the contact (κ), while also incorporating the angle of the cantilever relative to the horizontal (α). This lateral stiffness depends on the reduced shear modulus of the contact and the contact area ($\kappa = 8G^*a$), but this can also be described in terms of the Young's Modulus (E) and the contact stiffness (k^*) through the below equations 3.43,3.44,3.45 [3, 5].

$$G^* = \left(\frac{2-\nu_1}{G_1} + \frac{2-\nu_2}{G_2}\right)^{-1} \tag{3.43}$$

$$G = \frac{1}{2}\left(\frac{E}{1+\nu}\right) \tag{3.44}$$

$$\kappa = 8G^*a = \frac{8G^*k^*}{2E^*} = \frac{4k^*\left(\frac{2-\nu_1}{\frac{1}{2}\frac{E_1}{1+\nu_1}}\right) + \left(\frac{2-\nu_1}{\frac{1}{2}\frac{E_1}{1+\nu_1}}\right)}{E^*} \tag{3.45}$$

The solution of this model is quite complicated and so has been simplified into a modified quadratic equation (Equation 3.46) with each term incorpating the component characteristic equations (Equations 3.47,3.48,3.49) [5].

$$\frac{k^*}{k_c} = \frac{-B \pm \sqrt{B^2 - 4AC}}{6A} \tag{3.46}$$

$$A = \left(\frac{\kappa}{k^*}\right)\left(\frac{h}{L_1}\right)^2 (1-\cos(x)\cosh(xL_1))(1+\cos(xL')\cosh(xL')) \tag{3.47}$$

$$B = B_1 + B_2 + B_3 \tag{3.48}$$

$$C = 2(xL_1)^4(1+\cos(xL_1)\cosh(xL_1)) \tag{3.49}$$

$$\begin{aligned} B_1 = \left(\frac{h}{L_1}\right)^2 (xL_1)^3(\sin^2(\alpha) + \frac{\kappa}{k_c}\cos^2(\alpha)) \\ [(1+\cos(xL')\cosh(xL'))(\sin(xL_1)\cosh(nL_1)+\cos(xL_1)\sinh(xL_1)) \\ -(1-\cos(nL_1)\cosh(nL_1))(\sin(xL')\cosh(xL')+\cos(xL')\sinh(xL'))] \end{aligned} \tag{3.50}$$

$$\begin{aligned} B_2 = 2\left(\frac{h}{L_1}\right)(xL_1)^2\left(\frac{\kappa}{k_c}\cos(\alpha)sin(\alpha)\right) \\ [(1+\cos(xL')\cosh(xL'))(\sin(xL_1)\sinh(nL_1)) \\ +(1-\cos(nL_1)\cosh(nL_1))(\sin(xL')\sinh(xL'))] \end{aligned} \tag{3.51}$$

$$\begin{aligned} B_3 = (xL_1)\left(\cos^2(\alpha) + \frac{\kappa}{k_c}\sin^2(\alpha)\right) \\ [(1+\cos(xL')\cosh(xL'))(\sin(xL_1)\cosh(nL_1)-\cos(xL_1)\sinh(xL_1)) \\ -(1-\cos(nL_1)\cosh(nL_1))(\sin(xL')\cosh(xL')-\cos(xL')\sinh(xL'))] \end{aligned} \tag{3.52}$$

Again, the dispersion relationship of this third model has been shown (Figure 3.12). This model and the second model do not differ very much in their final frequency values, but this model has a slower frequency response at given contact stiffness values compared to the second model in Figure 3.10 [5].

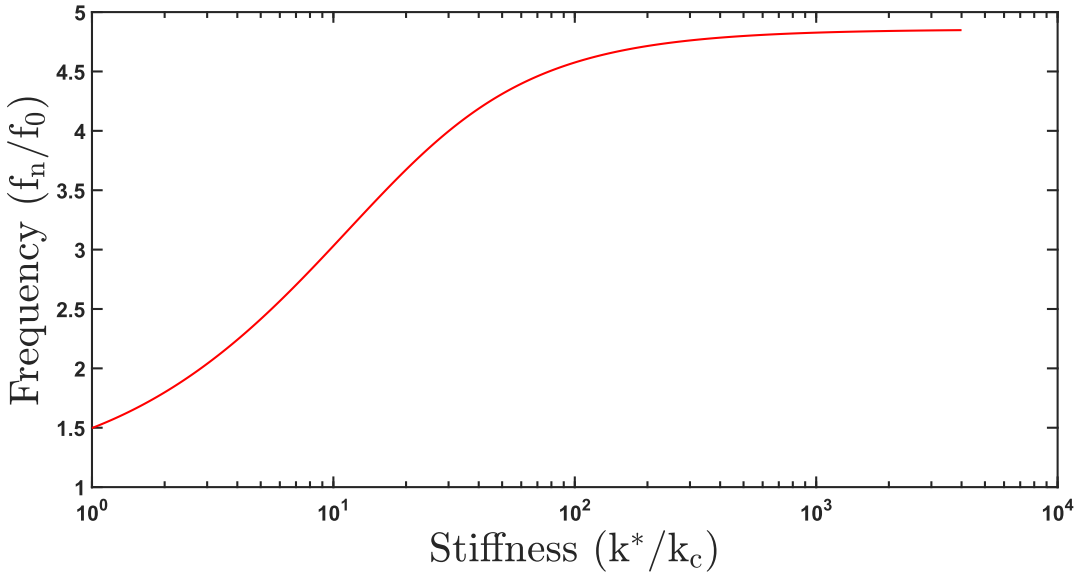


Figure 3.12: Dispersion relation of normalized frequency (f/f_0) vs normalized stiffness (k^*/k_c) for the 1st mode in Model 3 (Figure 3.11).

Damped Models

The models discussed thus far have not considered damping; however, each of the three models considered can include damping. For the purposes of this study, only one damped model was incorporated for the analysis, that being a damped version of the model discussed in (3.2).

The change in adding damping to the cantilever models has the consequence of introducing complex variables to account for the time-varying response of the cantilever. In the damping models considered, this shows up in the cantilever wave-number. Where in the undamped models the wave-number was used to determine the dimensionless stiffness ratio given a known frequency ratio in the damped models the wave-number is complex and relates to the damping of the cantilever. From [52] the real component is determined from the quality factor of the cantilever when out of contact, and the imaginary component is derived from the quality factor when in contact with the surface.

To find the dimensionless stiffness and finally contact stiffness, the quality factors of the cantilever must be known first. The quality factors can then be used to find the complex wave-number and from that the dimensionless stiffness can be solved numerically. In this process, three different damped models have been considered, which are those from [53, 52, 54] where each model has differences in the cantilever geometry and forces. The simplest model from Turner [53] (Figure 3.6) describes a simplified cantilever with the probe tip at the end of the cantilever. The cantilever is modelled through the stiffness of the cantilever (k_c), the vertical contact stiffness, and the damping of the system by a dash-pot (κ and

σ_{int} in the model).

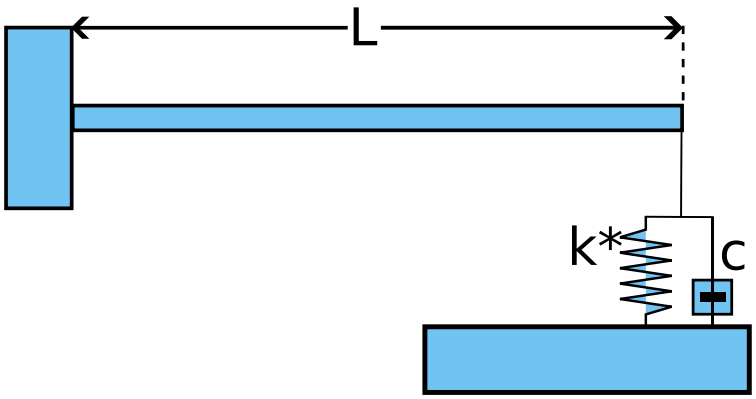


Figure 3.13: Schematic of simple damped cantilever model adding a dash pot alongside the spring in the contact.

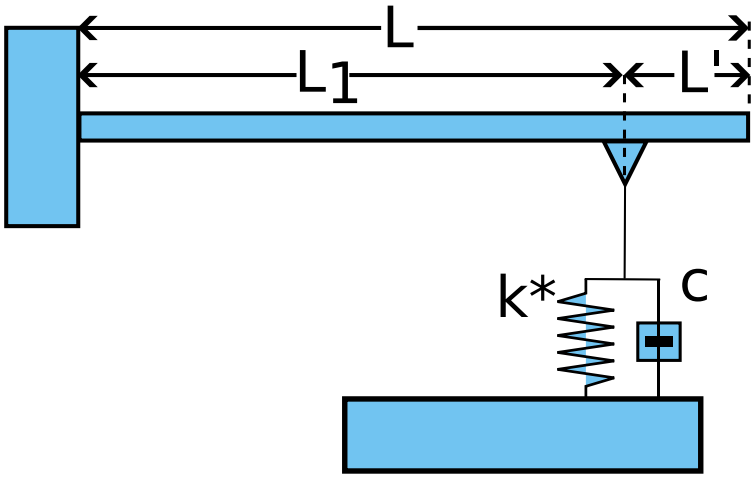


Figure 3.14: Schematic of damped cantilever model incorporating the tip position and lateral force.

In the following equations from Killgore et al. [6] the complex wave number ($\lambda_n L$) and dimensionless cantilever damping (χ) are derived in terms of the quality factor (Q_n^0, Q_n^0) and the resonant frequencies (f_n^0, f_n^c) when out of and in contact. The process to determine the contact stiffness begins with calculating the complex wave number and cantilever damping using equations 3.53 and 3.56. The wave number values are then used in the characteristic equation for the Kelvin-Voigt cantilever model (Equation 3.57) to solve for the dimensionless contact stiffness ($\alpha = k^*/k_c$) and damping (β).

$$\lambda_n L = a_n + i\, b_n \tag{3.53}$$

$$a_n = x_n^0 L \left(\frac{f_n^c}{f_n^0}\right)^{1/2} \tag{3.54}$$

$$b_n = a_n \left[\frac{(2\pi f_n^c - \chi Q_n^c)}{8\pi f_n^c Q_n^c}\right] \tag{3.55}$$

$$\chi = 2\pi\left(\frac{f_n^0}{Q_n^0}\right) \tag{3.56}$$

$$\begin{aligned}((\sinh(\lambda_n L_1)\cos(\lambda_n L_1) - \sin(\lambda_n L_1)\cosh(\lambda_n L_1) \\ (1+\cos(\lambda_n L')\cosh(\lambda_n L'))) + ((1-\cos(\lambda_n L_1)\cosh(\lambda_n L_1)) \\ (\sin(\lambda_n L')\cosh(\lambda_n L') - \cos(\lambda_n L')\sinh(\lambda_n L')))) \\ = \left(\frac{2}{3}\right)(\lambda_n L_1)^3[1+\cos(\lambda_n L)\cosh(\lambda_n L)]\end{aligned} \tag{3.57}$$

The contact stiffness (k^*) is then calculated and fed into the contact mechanics models to determine the contact area and the radius of the cantilever tip. The dispersion curve for these damped models follows closely with their undamped cases, but differs in that the quality factor changes along with the frequency. This gives insights into the viscoelastic behaviour of the contact, but adds more potential errors in estimating the quality factor value. The results along with the dispersion curves for the damped models are shown in Chapter 6.1.

Chapter 4

Methods

This chapter provides a comprehensive overview of the complete experimental setup, processes, and related analysis procedure. It encapsulates the fundamental AFM techniques and assessments that have been discussed, integrating them into the experimental procedure used in this project.

Furthermore, this chapter sets the groundwork for the specific outcomes and interpretations derived from the methods and analyses. These results are discussed in upcoming chapters, specifically Chapters 5,6, and 7. Each of these chapters delves deeper into the findings, providing a greater understanding of the interplay of key components of the experimental setup and analysis techniques.

4.1 AFM System

The AFM experiments were conducted in air on the Agilent Keysight 5500 and Asylum MFP-3D AFM systems under standard conditions. Due to the dry climate of Calgary, the relative humidity during the experiments varies within the range of $(20-40\%)$ relative humidity. Images of the Agilent system and Asylum system can be seen in Figures 4.1 and 4.2. The Agilent system is suspended by bungee cords and suspended on an air table. The cantilever probe is held in place by a spring, and the sample platform is mounted using magnetic legs.

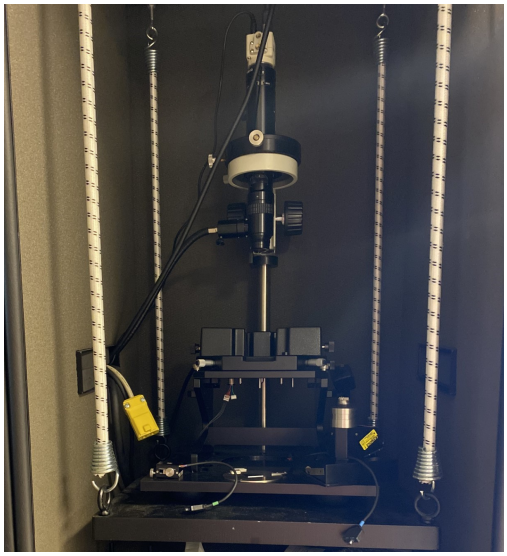


Figure 4.1: Image of Agilent Keysight 5500 Air AFM scanner and platform. The scanner is suspended on bungee cords and its locked in a steel box.

Differing slightly from the Agilent system, the Asylum system is also on an air table but the cantilever is constrained by a small screw and the sample platform is fixed in place.



Figure 4.2: Image of the Asylum MFP-3D Air AFM scanner (left) and sample platform (right).

The major difference between the systems is that the Agilent system has an open-loop scanner while the Asylum system is closed-loop. For this reason, the Asylum AFM was used for the indentation tests discussed later, whereas the Agilent AFM was used primarily for the contact resonance observations.

System Calibration

Before starting any experiments, the AFM system must first be calibrated to determine the cantilever normal sensitivity for later analysis. As mentioned in Chapter 2.4, these calibrations are done by means of a force spectroscopy sweep, while to determine the lateral sensitivity, several scanning techniques can be utilised. The lateral sensitivity was not determined for the tests in this thesis, as the normal force is dominant in the contact resonance behaviour during the force spectroscopy tests.

Static AFM experiments are the most commonly applied and simplest to operate, with surface topography and friction tests being the common tests. By calibrating the cantilevers, the normal deflection sensitivity can be accurately measured and the corresponding forces can be determined. The deflection sensitivity is determined by calculating the linear slope (Equation 4.1) when the cantilever is brought into contact during a force spectroscopy sweep (Figure 4.3).

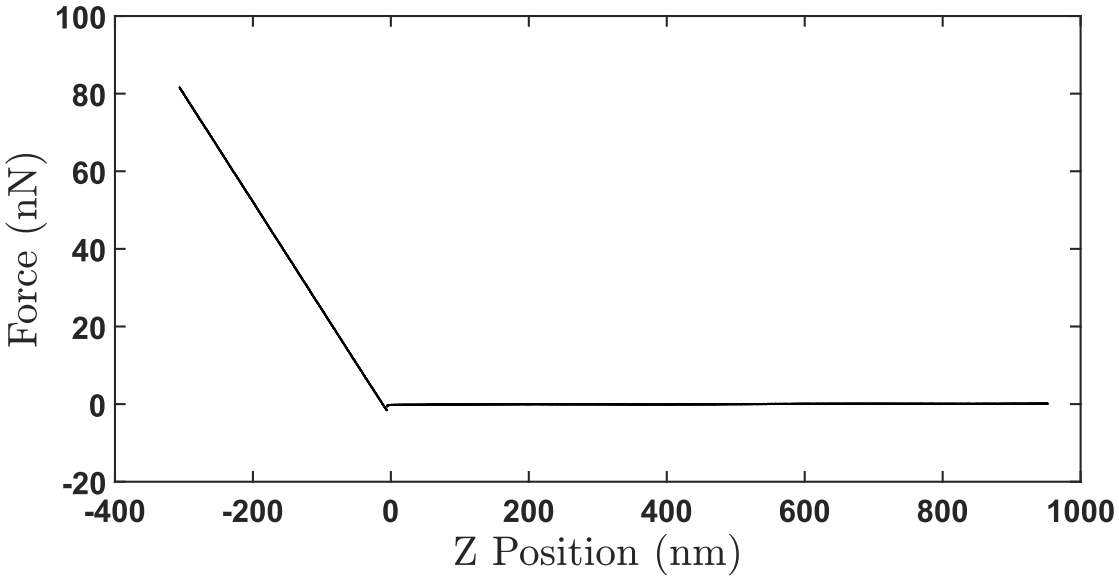


Figure 4.3: Example plot showing a approach portion of a force distance curve.

$$S = \frac{\Delta V}{\Delta Z} \tag{4.1}$$

This cantilever sensitivity has units of deflection in Volts per metre of sample Z height. During each force spectroscopy sweep the sensitivity must be determined although the range of values is fairly constant for a given AFM machine and cantilever setup. Now in order to covert the deflection into meters from the measured volts simply multiply the deflection voltage by the cantilever sensitivity (equation 4.2)

$$q = V * S \tag{4.2}$$

With the cantilever deflection now known in meters, results from scanning or other tests can be quantified in real terms such as the topography of the surface or indentation during force spectroscopy tests. In the case of indentation, discussed more in Section (7.1), the tip indentation into the sample surface

is found to be the difference between the cantilever deflection (q) and the sample Z-piezo height (Z) (Equation 4.3).

$$D = Z - q \tag{4.3}$$

The final quantity to determine in the case of the normal deflection is the normal force (F_N). The normal force is simply the cantilever normal deflection (q) multiplied by the cantilever stiffness (k_c) (Equation 4.4). The cantilever stiffness is unique to each probe and can be determined through a variety of methods (Section 2.3) with each method having advantages in different applications.

$$F_N = q * k_c \tag{4.4}$$

4.2 Sample Preparation

The samples tested on include cleaved graphite, silicon dioxide, and soft polymer materials including polyethyleneoxide (PEO) and polydimethylsiloxane (PDMS).

Table 4.1: Overview of sample materials used in testing. Silicon and HOPG values are taken from the literature [55, 56], while PEO and PDMS values were determined by nanoindentation testing (see Appendix 8.4).

Material	Young's Modulus	Poisson's Ratio
Silicon	160 GPa	0.3
HOPG	20 GPa	0.25
PEO	0.22 ± 0.03 GPa	0.5
PDMS	0.0025 ± 0.0002 GPa	0.45

For the HOPG samples they were cleaved using scotch tape prior to testing, while the silicon wafers and polymer samples were cleaned with ethanol and deionised water. Before performing the force spectroscopy tests, the sample was first scanned and the tip was placed over a flat section with no evident debris or scratch marks. Both polymer samples were fabricated using a spin-coating procedure with thickness values of roughly one millimetre.

4.3 Cantilever Preparation

Contact Probes

Most of the tests were conducted using standard silicon dioxide contact probes (PPP-CONT-50), although several different contact probes were tested, including platinum-coated and diamond-coated contact probes. The effect of the coating largely changed the hardness, with the diamond coating being the hardest, while platinum and silicon have very similar Young's moduli. The contact probes did not require any preparation, as they are ready-made and able to be tested right out of the box. The only calibration required was to determine the stiffness of the cantilever, which was done by measuring the thermal resonance spectrum along with confirming the length and width using an optical microscope.

Colloid Probes

The preparation of the colloid probes requires the application of gluing a small colloid particle onto the end of a tipless cantilever in an optical microscope. After the glue is applied, an isolated colloid particle is located, and the cantilever slowly approaches and then contacts the colloid particle. The cantilever is then left to dry and cure for up to one day.

Some problems and difficulties with this method revolve around the trouble of applying the correct amount of glue and attaching the colloid quickly enough before the glue begins to cure. Additionally, precisely positioning the colloid particle has proven to be difficult, with many probes having an off-centre colloid that can alter results when in the AFM.

Table 4.2: Overview of Cantilever Probes Used in Testing.

Material	Length (μm)	Width (μm)	Frequency (kHz)	Stiffness (N/m)
Silicon	450	50	12.5	0.067
Diamond	451	48	14	0.503
Platinum	449.5	49	13.5	0.0874
Glass Colloid	450	48.8	14.5	0.1134

4.4 Data Acquisition

In the force spectroscopy tests completed, two external data acquisition setups were used. External data loggers were required because the internal AFM data loggers did not record sufficiently fast to perform spectral analysis. The data loggers were run on a separate computer using a LabVIEW script that can control the recording speed, recording time, and voltage range. An overview of the data loggers used is given below in Table 4.3. Both data loggers used were National Instruments (NI) models which easily integrate with LabVIEW.

Table 4.3: Overview of Data loggers used in testing.

Data logger (μm)	Max Sampling Rate (MHz)	Bit Resolution
NI USB-6341	2.0 MHz	16-Bit
NI PCI-5122	100.0 MHz	14-Bit

Each data logger used has advantages and disadvantages with the USB model having a higher bit resolution and being able to record for longer periods of time while the internal PCI model having a much larger sampling rate. When conducting tests, the data loggers were triggered manually, although automatic triggering from the voltage input was experimented with. The data logger was triggered just before the jump-to-contact aiming so that the JTC is roughly in the middle of the data series (see Figure 4.4).

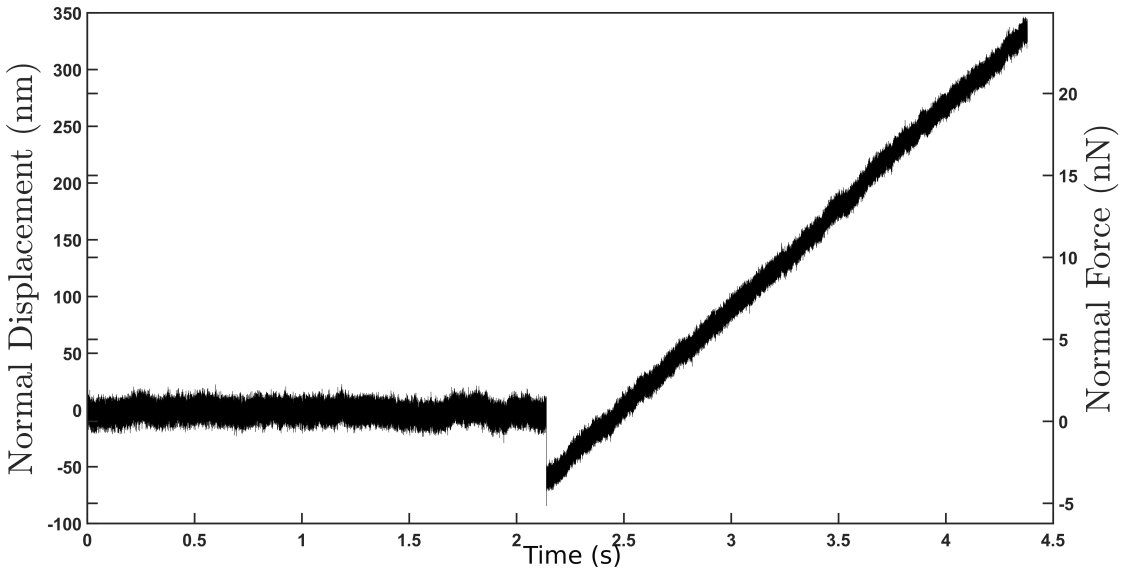


Figure 4.4: An example Force-Time series output from the external data logger. The raw signal is in Volts but is converted to Force from calibration.

During testing, the data logger was generally triggered at a consistent Z-piezo position during the sweep, as the JTC would occur regularly at a consistent Z position. As mentioned before, automatic triggering based on the recorded voltage was explored but due to the very consistent voltage range when the cantilever is in approach it is difficult to accurately predict when the JTC will happen purely based on deflection. Automated triggering based on the Z position would be ideal, but the AFM setup did not allow this signal to be fed into the data logger.

Test Procedure

The test procedure is quite simple and simply consists of standard force spectroscopy sweeps, as discussed earlier in the calibration section. As mentioned, the only change to the force spectroscopy tests was to slow down the Z travel speed to obtain a better time resolution for the AFM Z position. Generally, the whole sweep was roughly 60 seconds long, meaning the approach and retraction portions were 30 seconds each. Longer and shorter sweep times were tested, but it was found that one minute is a good balance between time resolution and measured force range. Because the data logger system was restricted to recording for up to roughly 10 seconds due to data storage limitations, a very long test meant that the range of force values recorded was small. This means that for the Fourier analysis and cantilever dynamics models, the amount of frequency dispersion is quite small, which introduces much more uncertainty into the results.

4.5 Analysis Procedure

With the force spectroscopy tests completed, the analysis procedure begins (Figure 4.5) which consists of three steps, those being:

1. Spectral Analysis (Fourier)
2. Cantilever Dynamics
3. Contact Mechanics

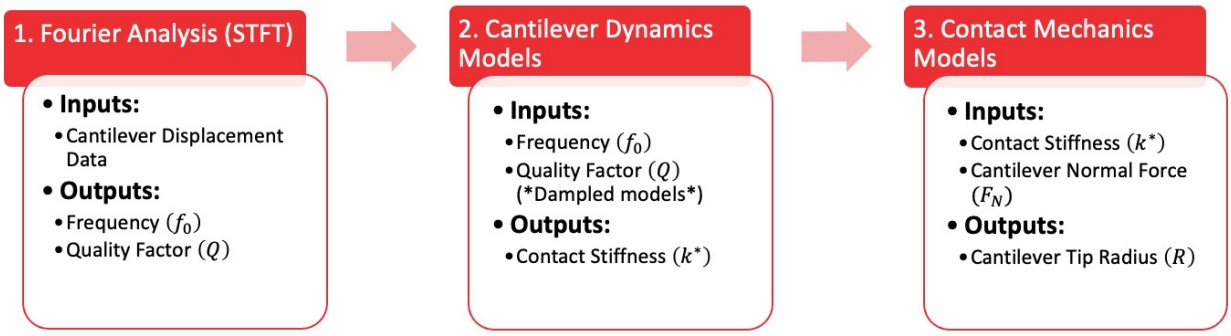


Figure 4.5: Flow diagram showing the primary analysis procedure for estimating the cantilever tip radius.

Spectral Analysis

From the output of the data logger, as visualised in Figure 4.4, the analysis begins with the spectral analysis, more specifically the short-time Fourier transform (STFT). As discussed in Chapter 3.1, the STFT performs a Fourier transform on specified Hanning time windows. This window of time (Figure 4.6) has been chosen in intervals of (2^N), and many of the results are generated with a window size of (2^{16}). More details on window sizing are discussed later in the Chapter 5.1.

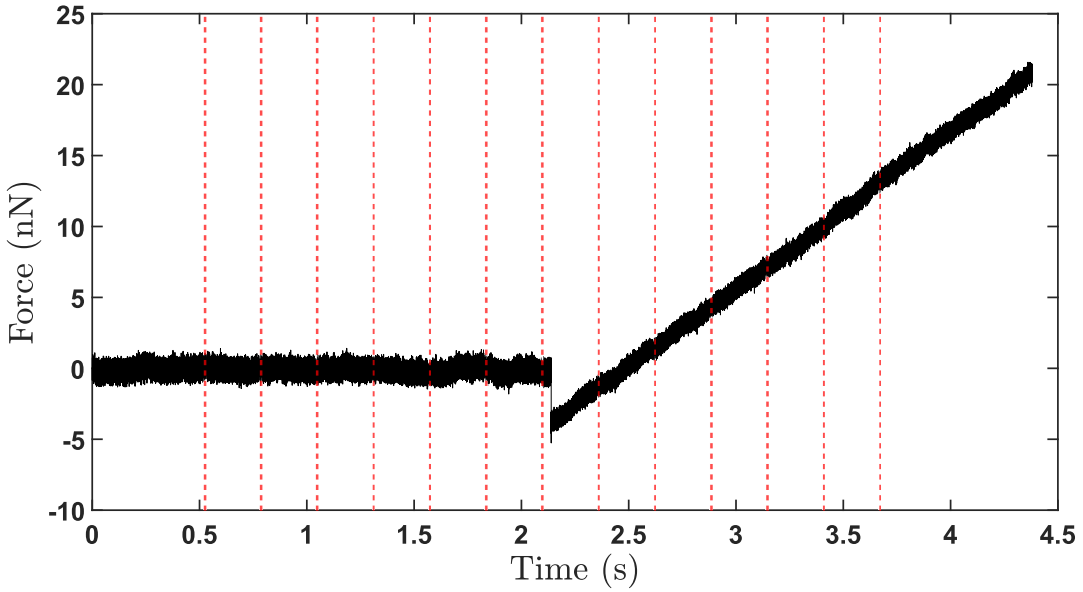


Figure 4.6: Visualization of the time windowing process done during the STFT analysis. Each dashed red line indicates the boundary between one window and another. The window sizing in this figure is (2^{20}) to emphasize the boundary between time windows.

With this time window now completed, the individual Fourier transforms can be performed on each window. More specifically, the Fourier transform generates the frequency spectrum of the cantilever within the time window. In Figure 4.7 the frequency spectrum of the first time window is shown of that in Figure 4.6.

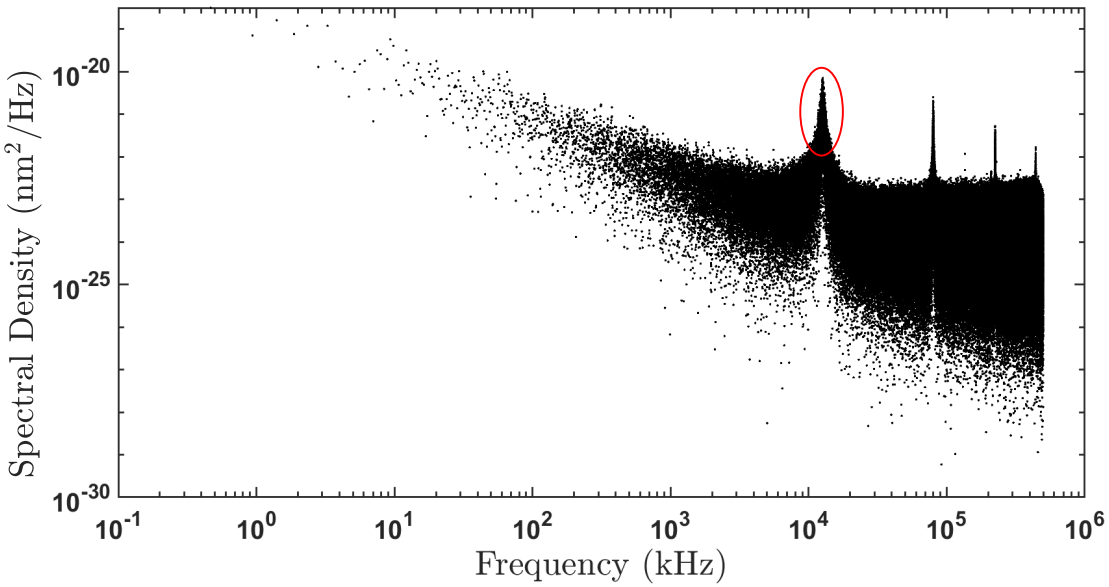


Figure 4.7: Example frequency spectrum of the cantilever when out of contact. The first mode to be fit is circled in red with subsequent modes at higher frequencies and lower amplitudes.

This frequency spectrum is then fit for the first mode, the largest and most prominent peak, using the Lorentz distribution (Equation 3.1) with a non-linear least squares fitting algorithm. The subsequent output of the first mode fitting of the frequency spectrum in Figure 4.7 is shown in Figure 4.8. The fitting outputs of the Lorentz distribution are the cantilever frequency (f) and the quality factor (Q) which are then used as the primary input into the cantilever dynamics.

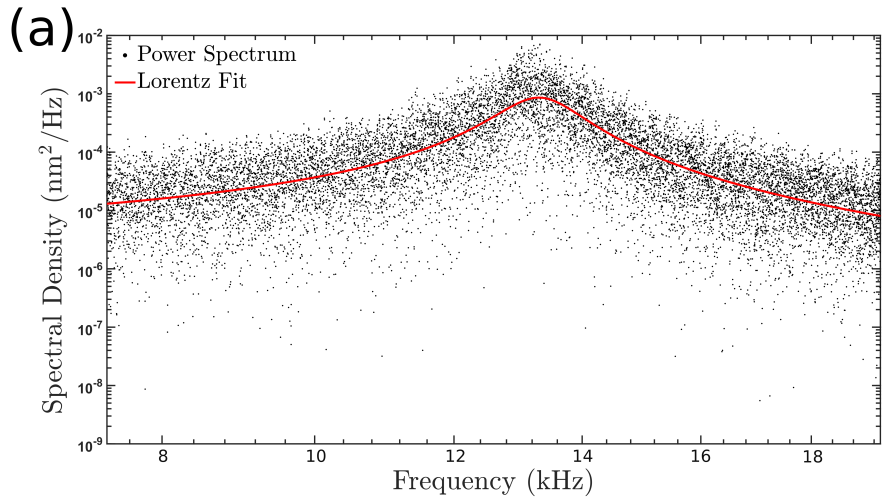


Figure 4.8: An example resonance peak fit using the according to the Lorentz distribution (Equation 3.1).

This fitting procedure is then performed in every time window, with the net result being the change in frequency and quality factor as a function of the measured normal force.

Cantilever Dynamics

The process for the cantilever dynamics portion of the analysis is actually quite simple. Contact stiffness (k^*) is calculated using the different cantilever models discussed in Chapter 3.2 with frequency (f), quality factor (Q), and cantilever stiffness (k_c) as input. The results of the cantilever dynamics can be seen in Chapter 6.1.

Contact Mechanics

The final step in the analysis process is to incorporate contact mechanics models to estimate the radius of the cantilever tip. This is done by taking the calculated contact stiffness (k^*) from the cantilever dynamics models and plotting those values against the normal force averaged over time (F_N). The tip radius is then estimated by fitting the data with the contact mechanics models using a non-linear least squares fitting algorithm. The choice of contact model to fit (Hertz, DMT, JKR) is based on the calculated Tabor parameter (μ_T) with a more rigid contact that favours the DMT model and a softer contact that favours the JKR model.

In the upcoming chapters, the results of the conducted procedures and tests will be laid out and discussed, categorising the material and cantilever combinations. Each analysis segment has been sep-

arated into different chapters, given their ability to stand independently. This organisational approach was done to show the relative independence of each analysis section from the other.

Chapter 5

Results - Spectral Analysis

The presentation of the results from spectral analysis details the successes and shortcomings of the Fourier and wavelet techniques in defining the cantilever frequency spectrum with precision. This section examines both of these techniques, assessing their performance in light of the experimental force spectroscopy data. Each technique, with its unique advantages and limitations, will be discussed, providing insight into its operational characteristics and suitability for this specific project. This exploration forms an integral part of the objective of a more refined understanding of the interplay between these spectral analysis techniques and the cantilever dynamics.

5.1 Short Time Fourier Transform

As discussed in section 3.1 the STFT allows for the normally stationary Fourier transform to be applied to time-varying signals over short time periods. This is particularly useful for the AFM field, as rapid changes in AFM cantilever frequencies can be used to determine changes in contact stiffness (k^*), tip-sample forces (F_{ts}), and cantilever properties such as quality factor (Q). In the process of this project, the STFT was applied to investigate the changes in cantilever dynamics during the jump-to-contact (JTC) portion of the force spectroscopy curve. From the quality factor and frequency shift of the cantilever, the interaction force between the tip and the sample can be accurately determined.

For all tests conducted, the STFT worked well in estimating the frequency once the correct window size was used. The result of this frequency adjustment gives a relationship between the changing cantilever frequency and the time averaged normal force (Figure 5.1). This frequency shift occurs when the cantilever jumps into contact and then increases very slightly until it plateaus when the cantilever is pressed further into the sample. This small change in frequency when in contact is the range of values taken further into consideration in the next stage of analysis.

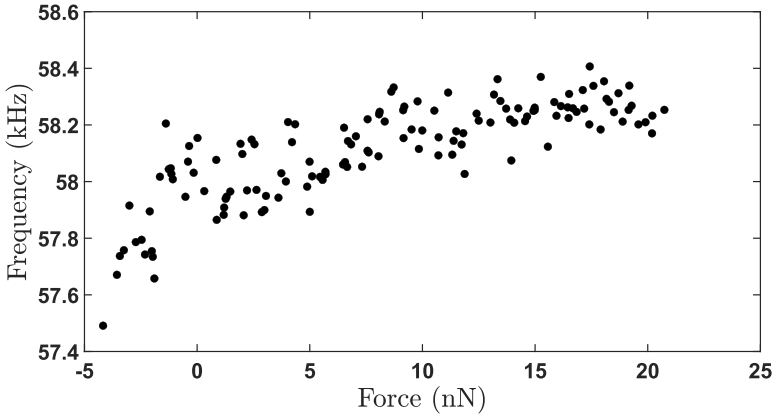


Figure 5.1: Cantilever Frequency (f) vs Normal Force (F_N) during the contact portion of a force-distance curve on a HOPG sample. After the large frequency change during the cantilever jump into contact the frequency slightly increases before plateauing with increasing force.

The other major parameter in fitting the Lorentz distribution (Equation 3.1) is the quality factor, which is a measure of the level of damping in the cantilever. For some tests such as the HOPG tests (Figure 5.2), the quality factor can be accurately measured and displays a similar increase and plateauing as the normal force increases. These quality factor results can then be incorporated into damping cantilever models in the next section of the analysis.

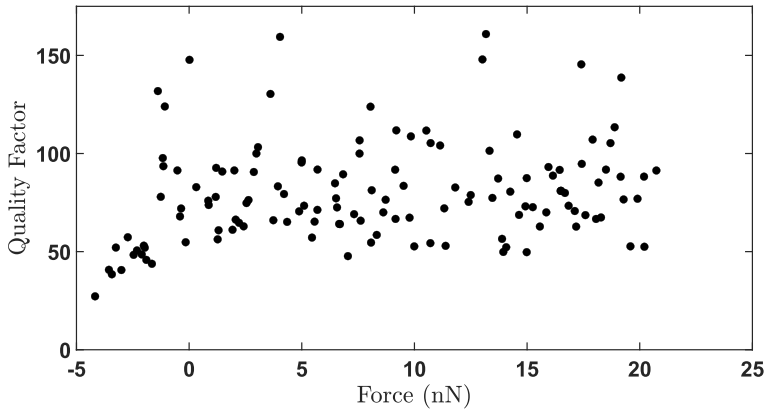


Figure 5.2: Cantilever Quality Factor (Q) vs Normal Force (F_N) during the contact portion of a force-distance curve on a HOPG sample. The plateauing phenomenon observed with the frequency is seen as well with the quality factor.

However, for many of the tip-sample combinations used, the frequency peak widths vary wildly between time windows, leading to the quality factor as a function of force appearing more random. In Figure 5.3 for a PDMS sample, this relationship is seen with no trend or repeatability of quality factor estimates between time windows.

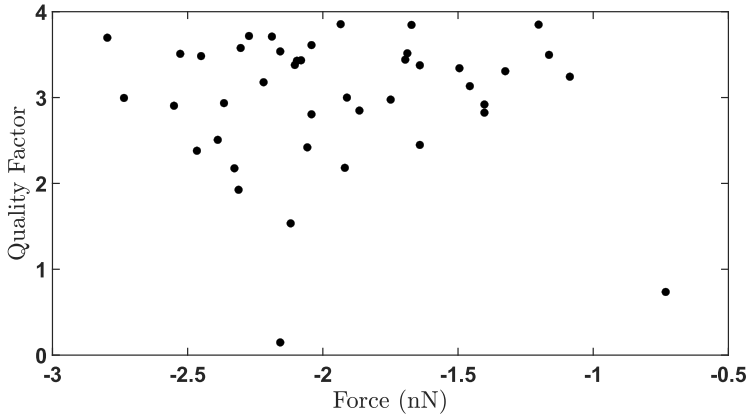


Figure 5.3: Cantilever Quality Factor (Q) vs Normal Force (F_N) during the contact portion of a force-distance curve on a PDMS sample. When compared to more rigid samples this material does not show any consistent trend in quality factor due to the large variability in the frequency peak width.

This difference between the more rigid samples and the very soft samples can be seen from the full frequency spectrum when comparing free (out of contact) and in contact. In the frequency spectrum for these rigid samples (Figure 5.4) the peaks of both free and in contact are sharp with the frequency shifts following the shift predicted by the cantilever models. However for the soft PDMS sample (Figure 5.5) when the cantilever jumps into contact the frequency shift is quite small and the first mode peak becomes much broader and damped out.

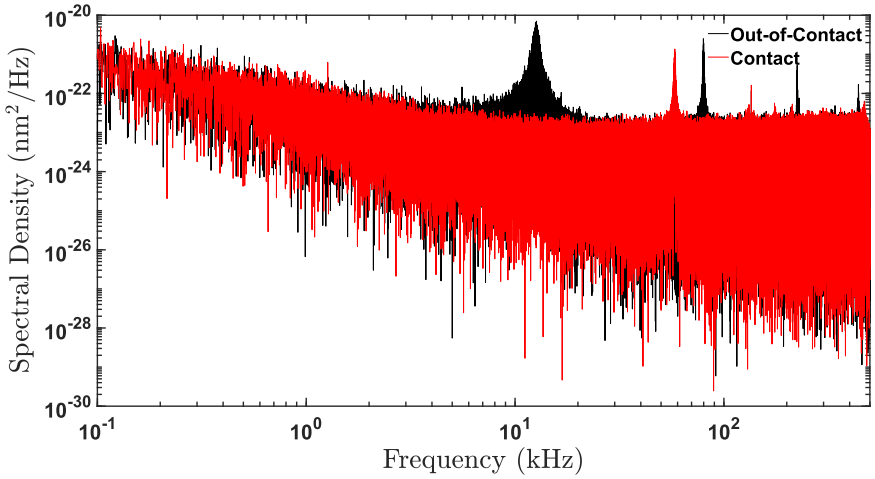


Figure 5.4: Example full frequency spectrum of a HOPG sample when the cantilever is out of contact (black) and in contact (red). When in contact the frequency modes shift to a higher frequency, modeled by the cantilever dynamics models, along with a change in the peak shape. In the case of HOPG and other stiff samples the peak becomes sharper resulting in a higher cantilever quality factor.

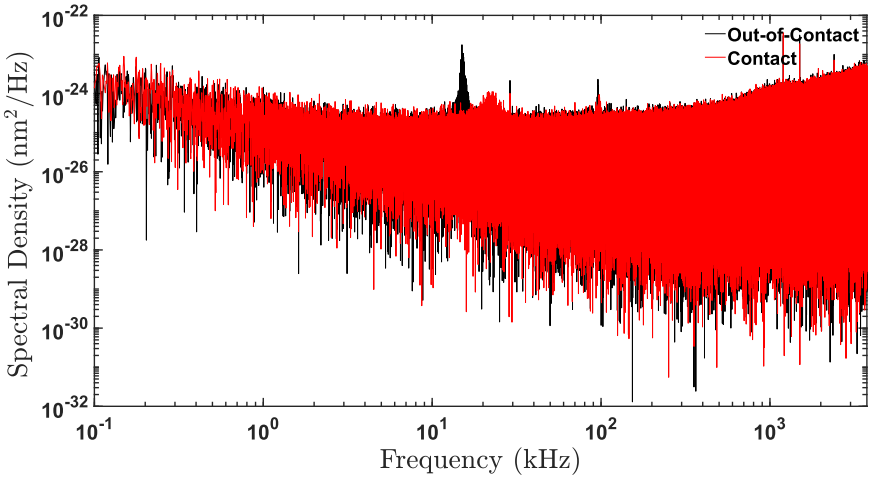


Figure 5.5: Example full frequency spectrum of a PDMS sample when the cantilever is out of contact (black) and in contact (red). When in contact the frequency modes shift to a higher frequency, modeled by the cantilever dynamics models, along with a change in the peak shape. In the case of PDMS the peak becomes much more broad along with a lower amplitude. This indicates higher damping and a smaller quality factor.

This broadening changes over the time of the force-distance curve, meaning that the fitting of the quality factor is very erratic as seen in Figure 5.3.

5.2 Comparison of CWT and STFT

In the process of fitting the resonant curves, various parameters of the wavelet transform were modified to improve the accuracy of the results. One of such parameters is the time bandwidth of the wavelet. The time bandwidth of the wavelet describes the decay time in the time domain and the energy spread (i.e., bandwidth) in the frequency domain [57]. In general, larger time-bandwidth values give greater precision in the wavelet transform (Figure 5.7), although there are diminishing changes and the values saturate at very large time-bandwidth values.

When tested with the CWT the frequency could be fit, but there would be periodic jumps in frequency and the frequency resolution was generally poor (Figure 5.6). These large jumps are likely due to erroneous data not being averaged out as the CWT acts on every data point in the time series. Additionally, the wavelet transform has a varying frequency resolution and at the low frequency of the contact probes ($10-15\ kHz$) the CWT gives large digitisation errors. This poor resolution is quantified in Equation 3.6 previously.

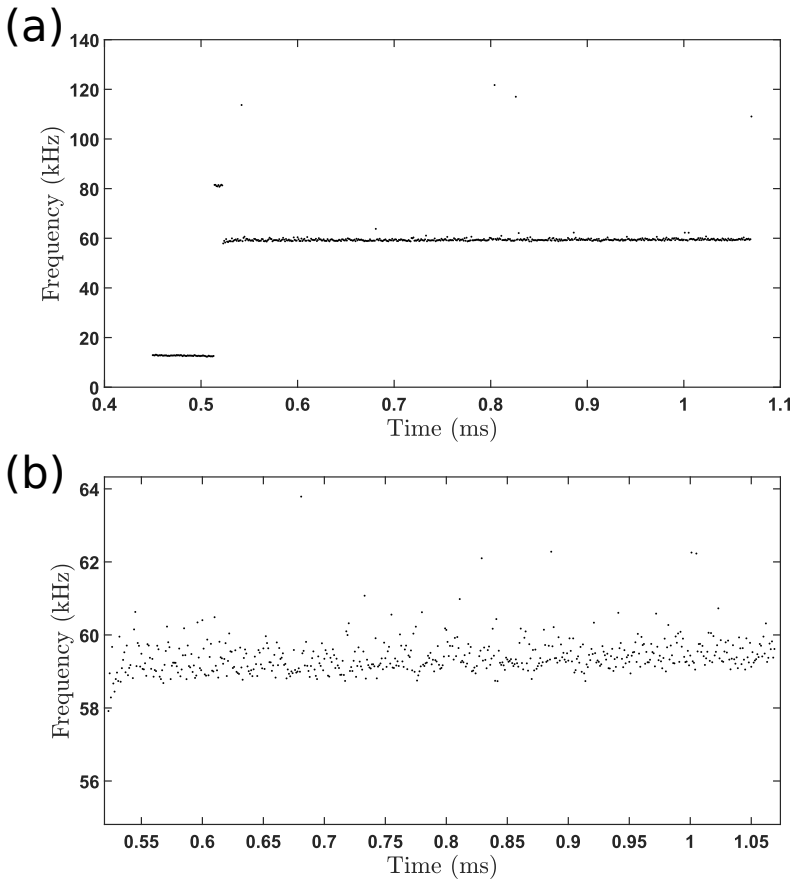


Figure 5.6: Frequency fitting results for a force spectroscopy sweep on a HOPG sample. (a) The large erroneous frequency jumps at the jump to contact can be seen along with the steps changes in frequency due to the poor frequency resolution of the CWT at the low frequency of the 1st mode of oscillation. (b) This is a zoomed in image just on the in contact portion. Note that this frequency shift in contact is barely noticeable as this wavelet data set covers just over one millisecond.

This poor frequency resolution also leads to the underestimation of quality factor when compared to the Fourier transform (Figure 5.8). Because the frequency peak for the CWT only has a few data points the true shape (i.e. magnitude) of the peak is missed and so the CWT consistently underestimates the quality factor. In Figure 5.7 this is visualized with the estimates for quality factor being compared between the STFT and CWT with increased wavelet time bandwidth. Even as the time bandwidth reaches its max value the quality factor plateaus well below the STFT.

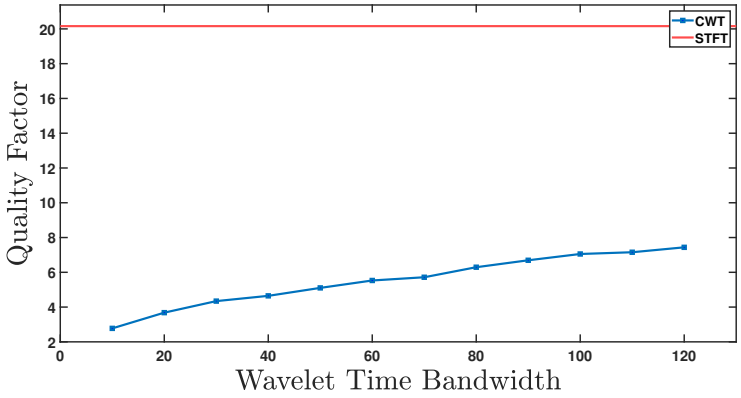


Figure 5.7: Comparison between Fourier (STFT) and wavelet (CWT) transform quality factor (Q) fitting at different wavelet time-bandwidth values. Note the STFT value is constant for a given window size.

The conclusion of wavelet analysis is that it can determine the changing frequency, but the quality factor and stiffness values vary greatly between the FFT and STFT methods. This result means that the CWT analysis is unsuitable for calculating contact mechanical properties, such as the contact stiffness. The STFT performed as expected when fitting the Lorentz distribution (Equation 3.1) to determine the frequency (f), but the estimates of the quality factor (Q) had a very large variance depending on the sample tested. Despite the success, there were some challenges that had to be overcome for the STFT to have repeatable results, namely the effect of changing window size. When testing with the STFT, the window size was changed from the smallest of (2^{12}) to the largest of (2^{21}). It was found that the window sizes smaller than (2^{16}) were too small and caused digitisation errors due to the poor frequency resolution, while the windows larger than (2^{20}) were so large that the STFT output had so few data points that it could not be fitted effectively in later analysis. An example table of an STFT using a 1,000,000 data point set with frequency resolution at various window sizes is summarised in Table 5.1.

Table 5.1: Example of STFT frequency resolution at different window sizes. The values at 2^{16} and 2^{20} are highlighted,, as these were the lower and upper bounds of the window sizes used with the STFT.

Window Size (2^N)	Window Size	Frequency Resolution	Windows
1	2	3000000	14999998
2	4	1500000	14999996
3	8	750000	7499996
4	16	375000	3749996
5	32	187500	1874996
6	64	93750	937496
7	128	46875	468746
8	256	23437.5	234371
9	512	11718.75	117184
10	1024	5859.375	58590
11	2048	2929.6875	29293
12	4096	1464.84375	14645
13	8192	732.421875	7321
14	16384	366.2109375	3659
15	32768	183.1054688	1828
16	65536	**91.55273438**	912
17	131072	45.77636719	454
18	262144	22.88818359	225
19	524288	11.4440918	111
20	1048576	**5.722045898**	54
21	2097152	2.861022949	25
22	4194304	1.430511475	11

In all analysis using the STFT the output was checked to ensure that the transformed spectrum did not have excessive spectral leakage. This was done using the equation introduced in Chapter 3.1 from Labuda (Equation 3.6). For a standard contact probe recorded at 1 MHz for one second with a first mode frequency of ($f_0 \approx 12.5kHz$) and a quality factor of ($Q \approx 20$) the lowest window size of (2^{12}) gives too small of a alpha parameter ($\alpha \approx 4.02$) while the common window size of (2^{16}) gives a sufficient parameter value of ($\alpha \approx 64.34$). When using other cantilevers with different frequency and quality factors, this parameter changes slightly, but in general, window sizes of (2^{16}) and larger give adequate (α) values.

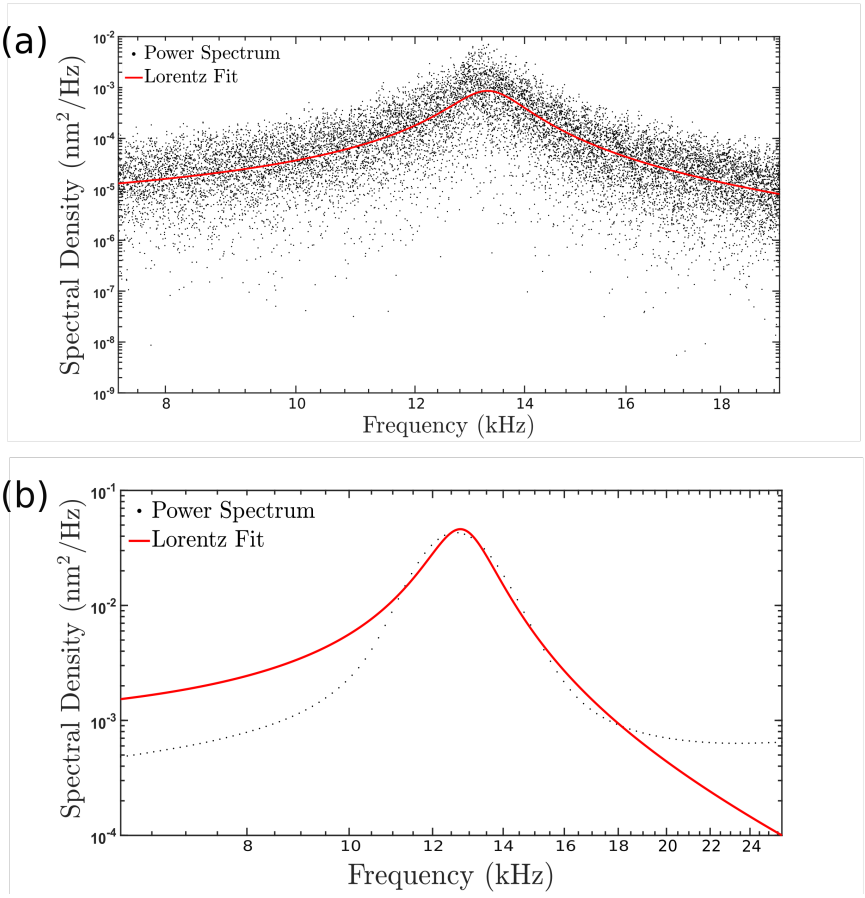


Figure 5.8: Comparison between 1st mode resonance peak for the STFT (Fourier) and CWT (wavelet) transforms. (a) Fitting result from the STFT at a (2^{16}) window size with the fitting outputs being ($f_{STFT} \approx 12.465 kHz$, $Q_{STFT} \approx 20.158$). (b) Fitting result for the wavelet transform with a time bandwidth of 120 and 48 voices per octave. The fitting outputs are ($f_{CWT} \approx 12.81 kHz$, $Q_{CWT} \approx 7.0265$).

Lastly, as discussed in Section 3.1, the computational requirements of the CWT limit its use to small data sets, while the STFT can be used in much larger data sets. In effect this means that computation time increases with greater time resolution for the STFT while for the CWT the computation time scales with increasing frequency resolution (i.e. number of scales). This relationship can be seen in Figure 5.9 where the number of convolutions increases logarithmically with the number of scales in the CWT.

At low frequencies there is not much difference between the two techniques as the frequency resolution required to capture signals is quite low, but at high frequencies the wavelet transform requires a much higher number of frequency scales to capture details in a signal. For the STFT to achieve higher frequency resolution you simply need to make the time window longer, as the resolution is dependent on the number of samples (N) and the sampling frequency (f_n) (Equation). This change reduces the computation time for the STFT, increases frequency resolution, but also reduces time resolution, and will average out transient behaviour in the signal.

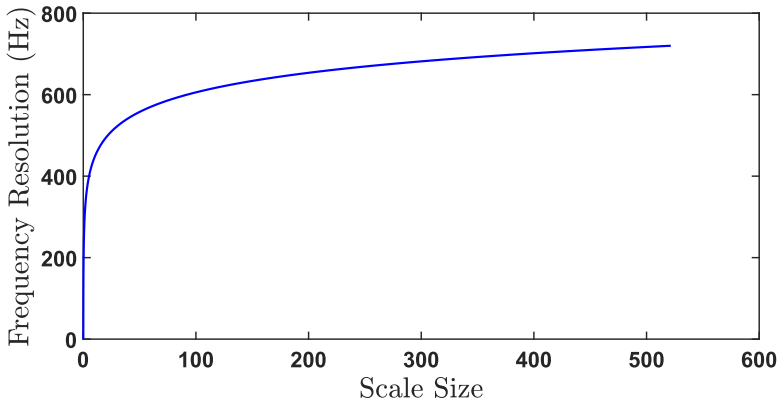


Figure 5.9: Frequency resolution of CWT as a function of scale size. The CWT frequency resolution has log_2 scaling dependent on (NV) (voices per octave) while the STFT has a constant resolution for a given window size.

5.3 Summary

As mentioned in this section and in Chapter 3.1, the significant results of the spectral analysis include the successful use of the Short-Time Fourier Transform (STFT) and the unsuccessful implementation of the Continuous Wavelet Transform (CWT). The STFT facilitated a precise identification of the cantilever's first mode resonant frequency and quality factor for the more rigid samples. However, when applied to softer samples, the determination of the Quality factor suffered a marked decrease in accuracy.

Despite digitisation errors, the wavelet transform demonstrated its effectiveness in determining the cantilever frequency in a majority of instances. Nevertheless, the determination of the quality factor was rendered unachievable, chiefly owing to the scarcity of data points at the lower end of the frequency spectrum.

In the process of defining the transform parameters, window sizes ranging from (2^{16}) to (2^{20}) were deemed optimal for the STFT, although with compromises between frequency and time resolution. Despite adjustments to the major parameters for the CWT, no significant enhancements were observed in fitting the the frequency spectrum. Moreover, the considerable computational demands of the CWT allowed for the transformation of only exceptionally short data sets. These computational limitations, along with the poor accuracy when fitting the frequency spectrum, led to the STFT being the primary technique used in the spectral analysis of the cantilevers motion.

Chapter 6

Results - Cantilever Dynamics

The results of the cantilever dynamics analysis seek to establish a relationship between alterations in cantilever frequency and the corresponding contact stiffness, as well as the mechanical attributes of the contact. Discussion here covers an array of tested sample materials, each paired with a distinct cantilever, with the intent of navigating through the broad spectrum of potential mechanical properties inherent in these contacts.

As discussed in Chapter 5.1, accurate determination of changes in resonant frequencies allows for greater insight into the changing contact stiffness of the tip-sample system. During the jump-to-contact period, the cantilever goes from experiencing no external forces while being fully out of contact to having both adhesive and repulsive contact forces when the jump occurs. These external forces have the effect of changing the model by which the cantilever oscillates. It transitions from an unsupported cantilever when out of contact to a pin-supported cantilever when with very high tip-sample forces [4]. Refer to Figure 3.7 for visualising the free and pinned boundary conditions.

6.1 Cantilever Dynamics

The major result from the cantilever dynamics models is the effect on contact stiffness of incorporating more and more geometric complexity into the cantilever model. In Figure 6.1 for the HOPG sample as seen in Chapter 4.5 the three different undamped models from section 3.2 give varying contact stiffness estimates. To simplify the discussion of these results, the three different undamped models will be shown as models 1, 2 and 3, with model 1 being the cantilever tip at the end (Figure 3.6), model 2 having the accurate tip position (Figure 3.9), and model 3 incorporating the lateral forces (Figure 3.11).

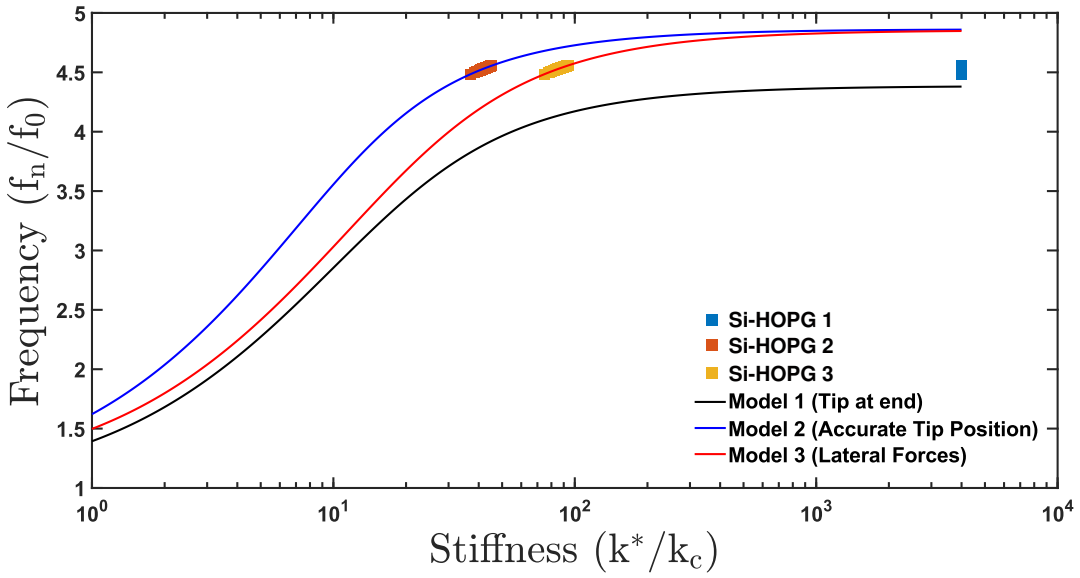


Figure 6.1: Dispersion relation of experimental frequency results laid over analytical models for model 1 (3.6), model 2 (3.9), and model 3 3.11 for a Silicon contact probe on a HOPG sample.

Given that the frequency inputs into these models is the exact same the differing contact stiffness values results from the changes made to the setup of the model. For example between model 1 (tip at cantilever end) and model 2 (accurate tip position) the second model has a larger contact stiffness at a given frequency shift. This is due to the tip position in model 2 effectively reducing the length of the cantilever resulting in a relatively stiffer contact. The small change in the tip positioning also allows for more reliable matching of the theoretical cantilever frequency and the measured frequency. In Figure 6.1 the frequency data does not map onto the models values due to effect of the tip positioning.

This result is seen reliably with other tests (Figure 6.5) where the cantilever tip position makes model 1 largely unusable to estimate contact stiffness. Now, while model 1 has proven to be unable to accurately model the frequency data, models 2 and 3 both give consistent results. However, there is a large gap in the contact stiffness estimates between models 2 and 3.

The next test was performed on a diamond-coated silicon probe on a silicon surface (Figure 6.2). This tip-sample configuration gave a larger frequency shift in comparison to the HOPG sample, which then led to much larger contact stiffness values. With these dispersion curves being on logarithmic scale, it may be hard to notice, but even this small change in frequency values gives a disproportionate change in contact stiffness.

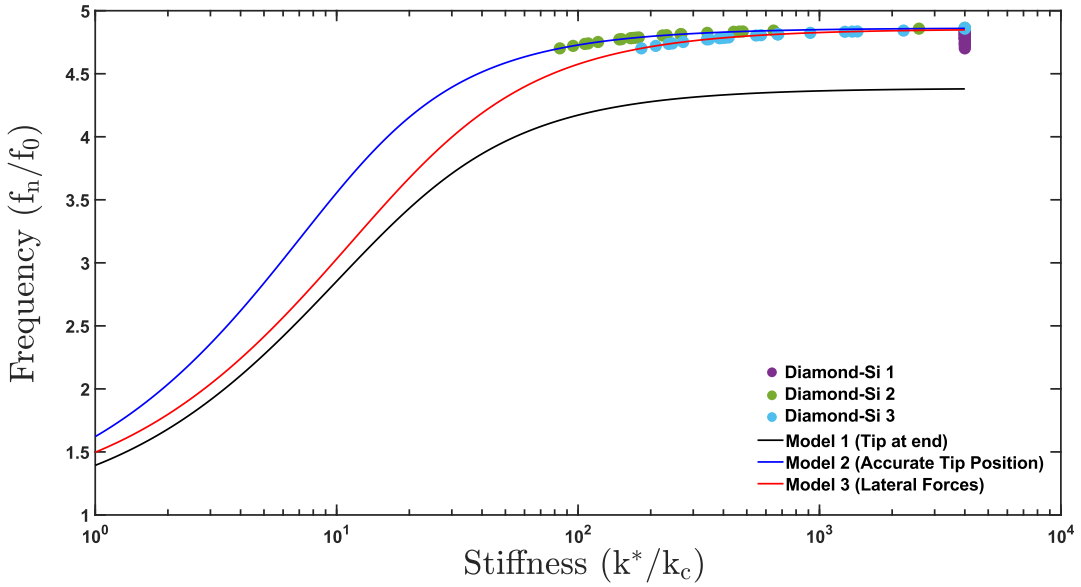


Figure 6.2: Dispersion relation of experimental frequency results laid over analytical models for model 1 (3.6), model 2 (3.9), and model 3 3.11 for a Diamond coated Silicon contact probe on a Silicon sample.

The next set of figures are the polymer samples of PEO (Figure 6.3) and PDMS (Figure 6.4). First, the PEO test shows a frequency shift in between that of the HOPG and Diamond tests with the corresponding intermediate contact stiffness values. This was somewhat unexpected given that the PEO sample is softer than the HOPG and Silicon samples, although this sample of PEO is stiff for a polymer, so the contact is not showing signs of greatly increased damping.

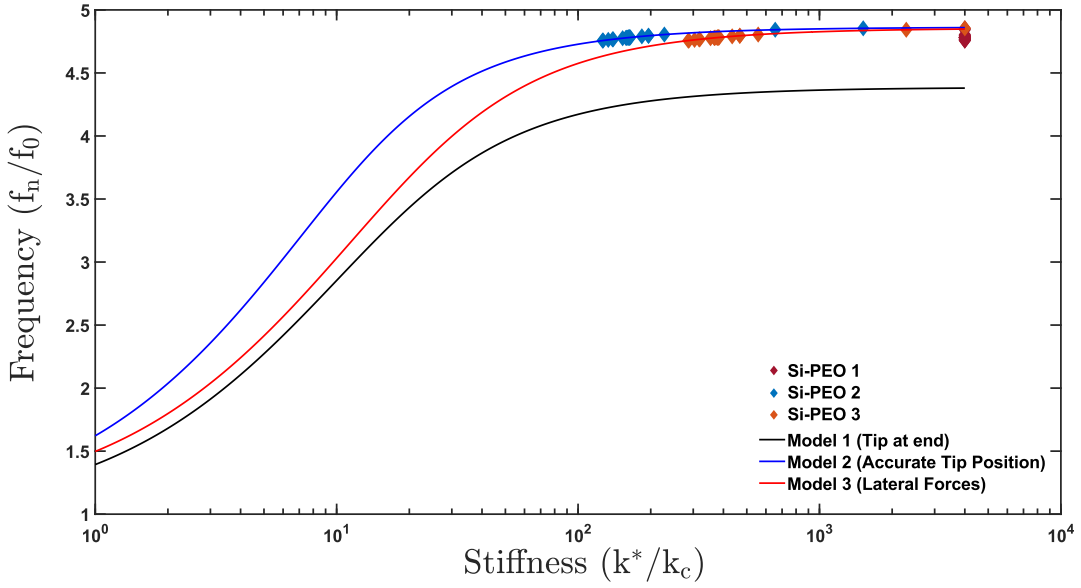


Figure 6.3: Dispersion relation of experimental frequency results laid over analytical models for model 1 (3.6), model 2 (3.9), and model 3 3.11 for a Silicon contact probe on a PEO sample.

Changing from PEO, the PDMS sample response is very different, with the observed frequency shift being very small in comparison. This small frequency shift for the PDMS sample corresponds to the change in frequency peaks becoming very flattened indicating much higher damping. This high damping makes the contact more viscoelastic, which explains why the frequency shift is much lower than expected by the models and confirmed by the previous tests with harder and more elastic contacts. Because of these reasons, this sample was also analysed using the damping model, but due to very high variance when estimating the quality factor there is low confidence in that set of estimates.

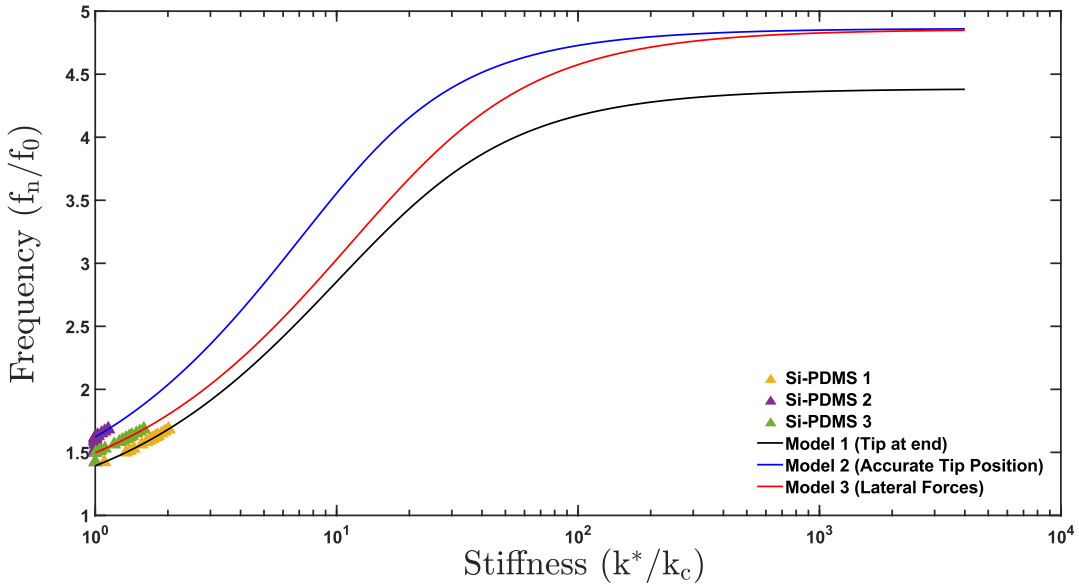


Figure 6.4: Dispersion relation of experimental frequency results laid over analytical models for model 1 (3.6), model 2 (3.9), and model 3 3.11 for a Silicon contact probe on a PDMS sample.

A summary of these four tip-sample configurations are displayed in Figure 6.5 where the results discussed in the previous plots are shown. These sets of tests cover a large portion of the frequency dispersion area but the middle portion has not been accessible as this is the jump-to-contact region where the cantilever frequency shifts within a few data points on the data logger.

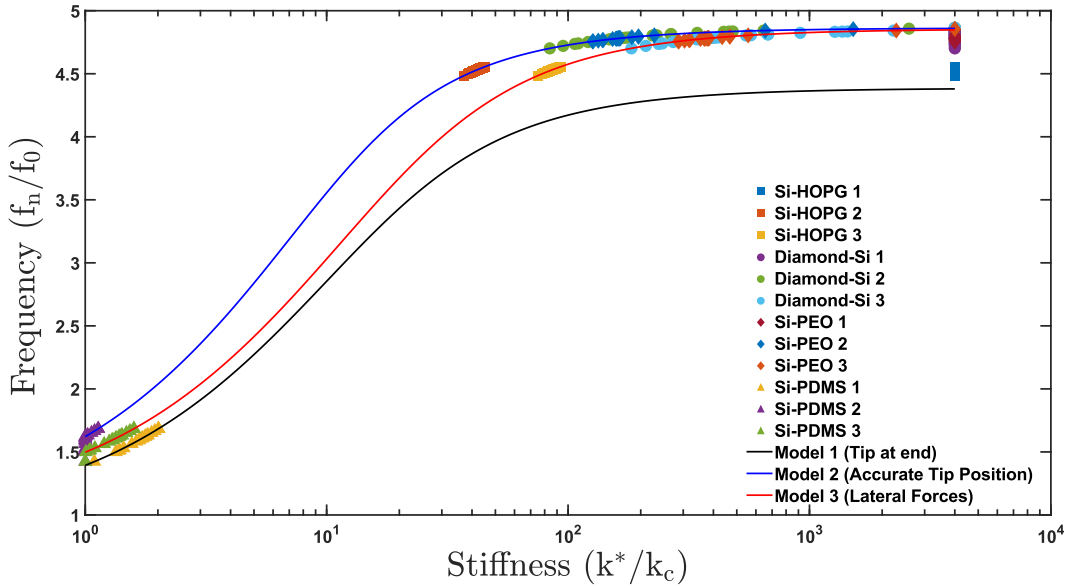


Figure 6.5: Dispersion relation plotting experimental frequency results laid over analytical models for model 1 (3.6), model 2 (3.9), and model 3 (3.11).

In addition to these undamped models, the damped model described in Section 3.2 was tested as well, giving very similar results to the undamped models. As seen in Figure 6.6 for a test on HOPG the damping model gives intermediate results between model 2 (accurate tip position) and model 3 (includes lateral forces). As mentioned above, this model was tested on the much softer PDMS sample as well as the others, but the high variance when fitting the quality factor the damping models lead to significantly differing results for many of the samples.

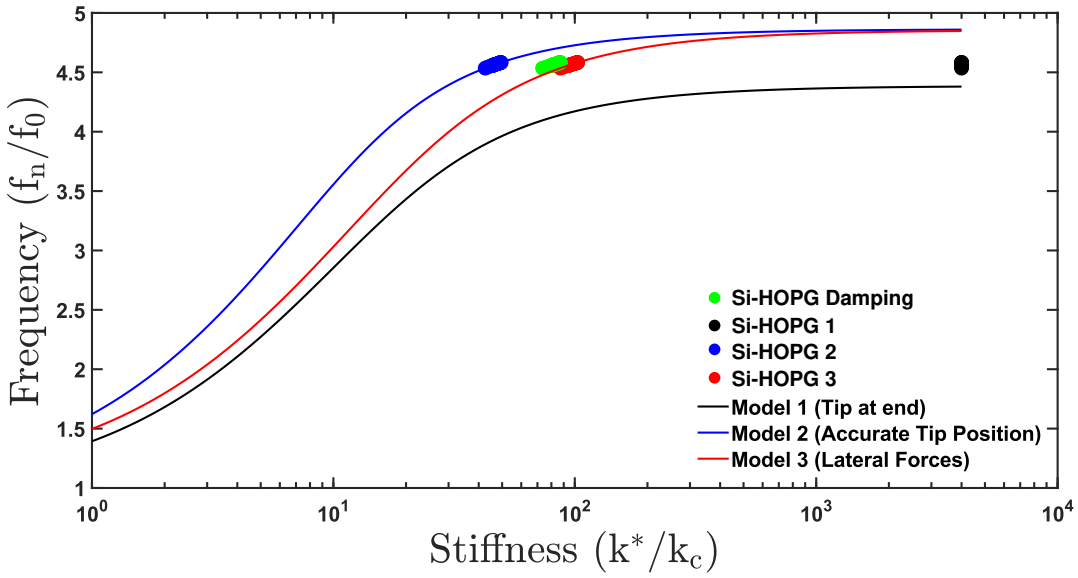


Figure 6.6: Dispersion results of the damped model illustrating the difference between the damping model used (Figure 3.57) and the undamped models.

6.2 Summary

In the realm of cantilever dynamics, the results suggest that only the more geometrically nuanced models, specifically model 2 (which accounts for accurate tip position) and model 3 (which includes lateral forces), hold general validity. The rudimentary first model tends to underestimate the frequency shift for the cantilever, rendering it ineffective for most of the tests conducted. When comparing the normalised stiffness values across all tests, model 2 consistently registers lower figures than model 3. This divergence arises mainly from the consideration of lateral forces in model 3, but other variances, such as cantilever tilt and height, also come into play. Although more sophisticated models were explored, they were ultimately excluded from the study as the marginal impact on contact stiffness estimates did not justify the introduction of new potential error sources. One example is Mahdavi's [54] model, which, despite generating a slightly more precise dispersion curve between frequency and stiffness, demands more model inputs and sophisticated analysis, which may pose trade-offs in terms of complexity and accuracy [54].

A unique observation was made with the extremely soft PDMS sample, which exhibited a frequency behaviour markedly lower than what the cantilever models predicted. This discrepancy is believed to stem from the highly soft nature of the sample, which causes the contact to display a more viscoelastic behaviour, contradicting the purely elastic assumptions underpinning the cantilever models.

Chapter 7

Results - Cantilever Effective Tip Radius Estimation

In the concluding section of the results, contact stiffness estimations derived from cantilever dynamics are used to extrapolate the effective radius of the cantilever tip using contact mechanics models. Two primary models, DMT and JKR, are selectively used based on contact properties, namely the Tabor parameter. The choice between these models is guided by the Tabor parameter, a concept explored in Chapter 2.4. This approach allows leveraging the most suitable model for the given set of contact properties, thereby producing more accurate and reliable findings.

7.1 Contact Mechanics

In the cantilever dynamics models the normalised stiffness (k^*/k_c) (contact stiffness to cantilever stiffness) was found given a known normalised frequency (f_n/f_0) (frequency in contact to frequency out of contact). After applying the cantilever dynamics models to determine the contact stiffness (k^*), the radius of the cantilever tip was estimated using the DMT and JKR contact mechanics models. These models take the calculated contact stiffness and convert it into the radius of the cantilever tip. Note, though, that this procedure can be generalised with other properties that can be fitted for.

Model Fitting

When applying the contact mechanics models, the effective radius of the probe tip (R_{tip}) is fitted given the experimentally measured normal force (F_N) and the estimated contact stiffness calculated from the cantilever models discussed in Chapter 6.1. The contact mechanics models that are fitted are the Hertz, DMT, and JKR models found in equations (2.21,2.22,2.23). The following are several plots of the fitting results for different cantilever-sample combinations with their corresponding estimated radii. The exact radius values vary, and softer samples generally give larger radius values. Despite this, each test shows that the radius estimates are far too small and gives non-physical values.

As discussed in Chapter 6 the first tip-sample combination tested on was a Silicon contact probe on a cleaved HOPG sample. Taking the contact stiffness values from Figure 6.1 and plotting them against the normal force averaged over time, the DMT models were fit to estimate the radius of the tip. The DMT model was chosen as the calculated Tabor parameter indicates that the DMT model more accurately fits this contact. A summary table of the Tabor parameters for different combinations of tip samples is shown in Table 7.1.

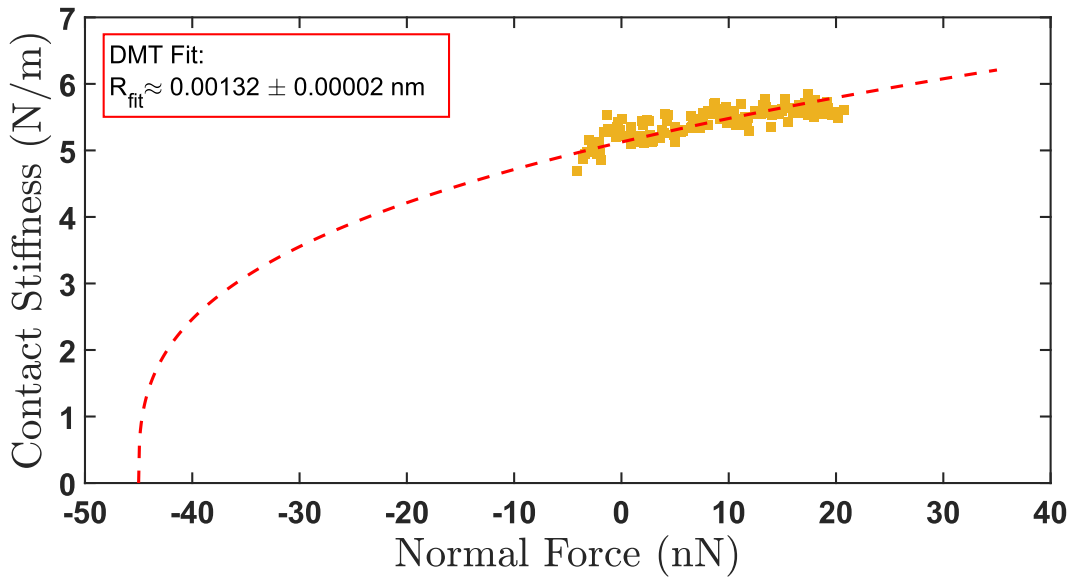


Figure 7.1: DMT model fitting results of Silicon Contact Probe on HOPG sample. The Young's modulus used for this fitting was taken to be 20 GPa [55].

As can be seen in Figure 7.1 the estimated radius value is far too small although the DMT model does closely fit to the data. This seems to indicate that the model scaling is broadly accurate, but there is something missing in the model that may explain the large difference.

Moving from this HOPG sample, subsequent tests aimed to explore the range of contact stiffness values by testing both very hard and very soft tip-sample combinations. On the harder end of the spectrum is the diamond probe on a silicon sample (Figure 7.2). The results of this figure show that the contact stiffness calculations from the cantilever dynamics do not fit according to the DMT model and instead look to diverge. The reason for this result is the very high frequency shift as shown in Figure 6.5, where the frequency shift is approaching the limits of the cantilever model.

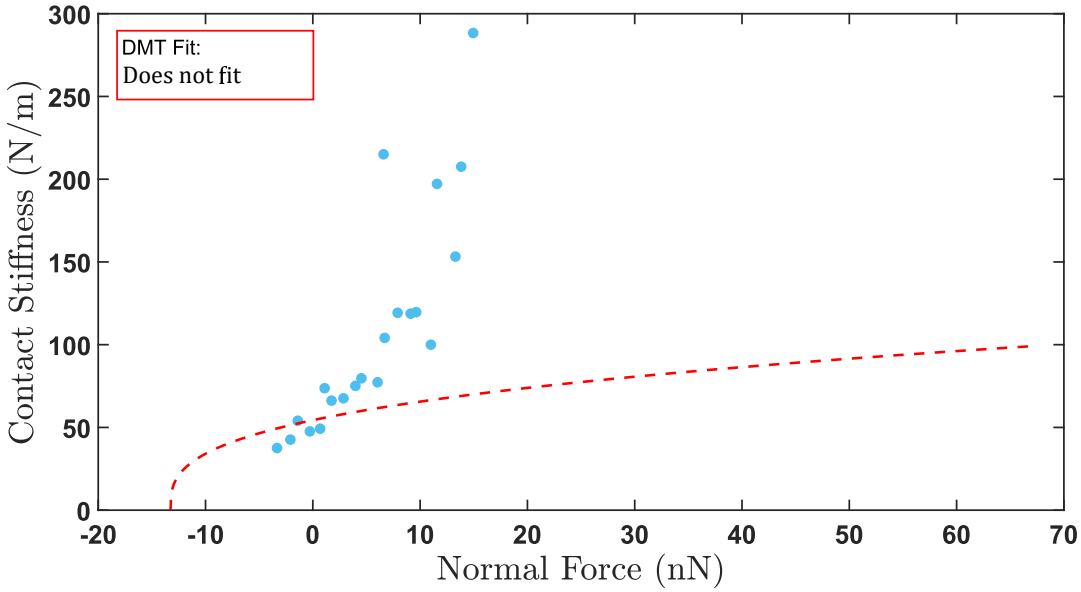


Figure 7.2: DMT model fitting results of Diamond coated Silicon Contact Probe on Silicon sample. Young's modulus for the silicon sample was taken to be 160 GPa [55, 56].

Moving to more comprehensive cantilever models may allow for these very stiff tests to be better analysed, but for the case of the cantilever models explored in this thesis it appears there is an upper limit to the physical system that can be analysed on.

Moving to the softer end of the spectrum, these third and fourth sets of tests use PEO polymer samples (Figure 7.3) and PDMS (Figure 7.4) using a silicon contact probe. The contact model used to fit was changed to the JKR model, as the Tabor parameters calculated were far higher pointing to the JKR model being more applicable to these softer samples. The radius estimates themselves are larger than the harder samples, although in absolute terms they are still smaller than the real cantilever tip radius.

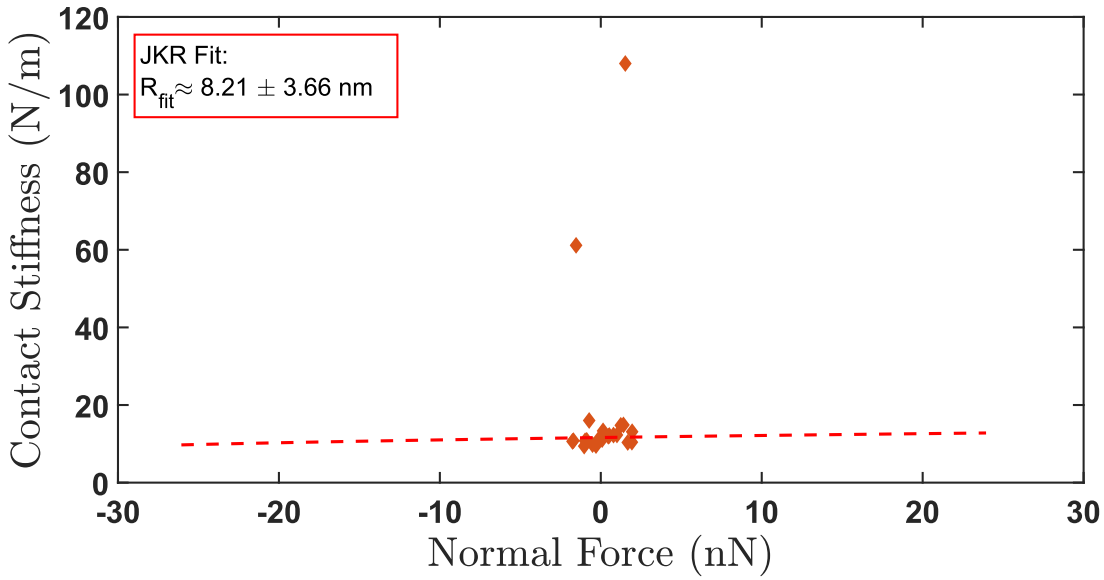


Figure 7.3: JKR model fitting results of Silicon Contact Probe on Polyehtylenoxide (PEO) sample. Young's modulus of the PEO sample was determined to be $0.22 \pm 0.03\ GPa$ by nanoindentation testing (Appendix 2).

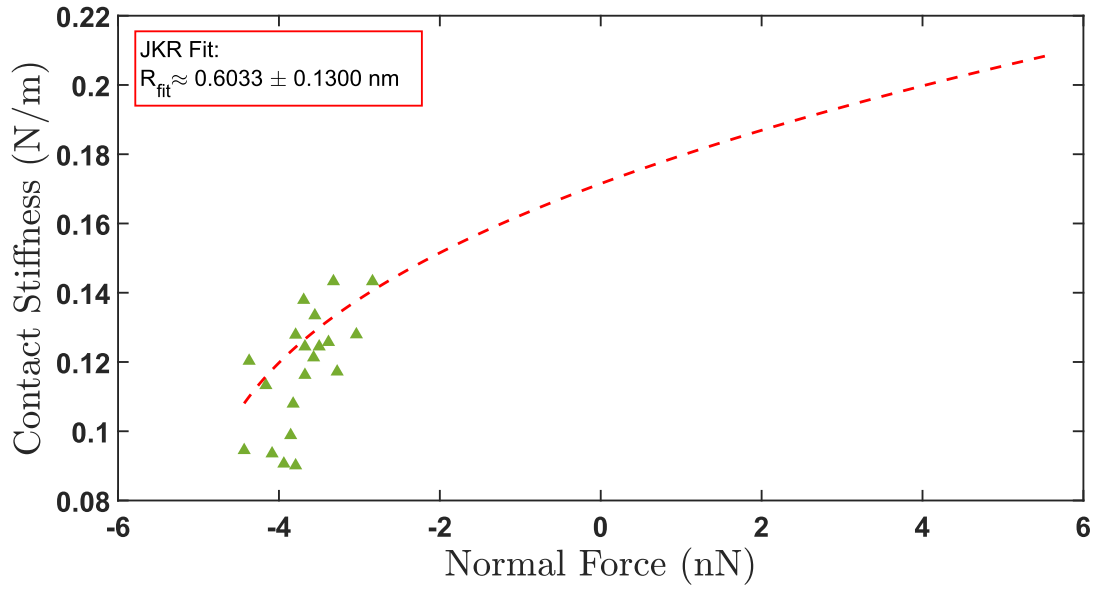


Figure 7.4: JKR model fitting results of Silicon Contact Probe on Polydimethylsiloxane (PDMS) sample. Young's modulus of the PDMS sample was determined to be $0.025 \pm 0.002\ GPa$ by nanoindentation testing (Appendix 1).

The results of these polymer tests indicate that the softer samples approach the applicable range of the contact mechanics models because of the much higher sample indentation, although the estimates are still too small. The PEO sample gave the best results, which the radius being within the same order

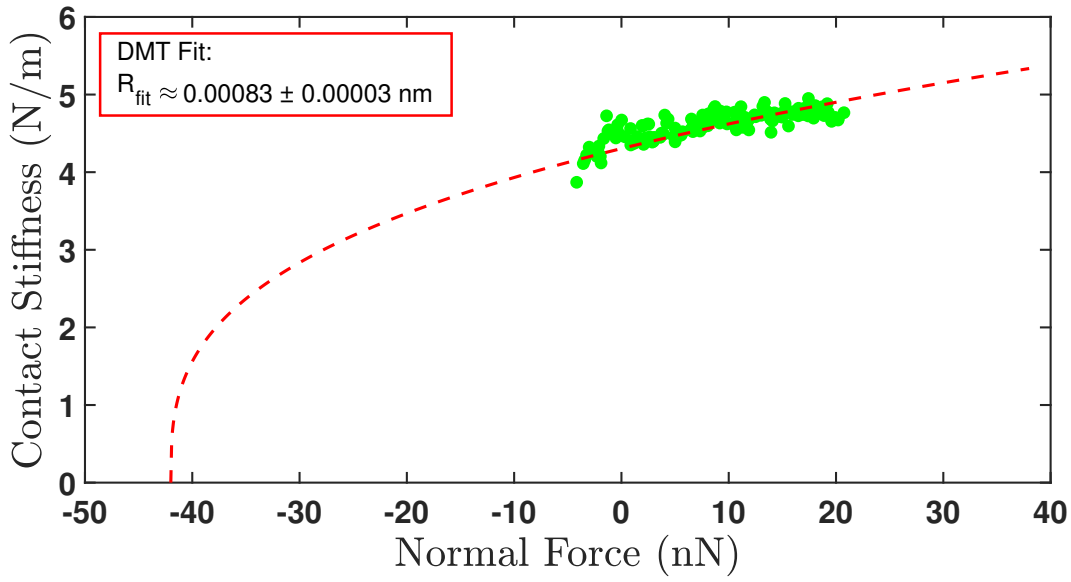


Figure 7.5: DMT fit of contact stiffness vs normal force for a Silicon probe on a HOPG sample using the damping model shown in Figure 3.57.

of magnitude as the real tip radius, but this data has large variance and poor confidence. Additionally, the soft polymer samples have much higher damping, which makes the spectral analysis less reliable because of the broadening of the frequency peaks and the introduction of viscoelastic behaviour of the sample. The aim of incorporating this damping through the quality factor was done using the model described in Figure 3.57 however, due to the problems with accurately fitting the quality factor for the polymer tests, only the more consistent HOPG and silicon samples are included.

In Figure 7.5 this damping model is run through the procedure and a DMT fit is performed to estimate the radius of the tip. The fitting result is similar to that of the undamped models with the specific values lying between model 2 (accurate tip position) and model 3 (including lateral forces). However, this result is only applicable for harder samples such as HOPG and Silicon, while softer samples may show a large difference between damped and undamped models.

Finally, after varying the sample materials, the colloid probes were also tested. Figure 7.6 is an example fit result for a glass colloid probe showing the problems of adapting cantilever models to work with colloid probe cantilevers.

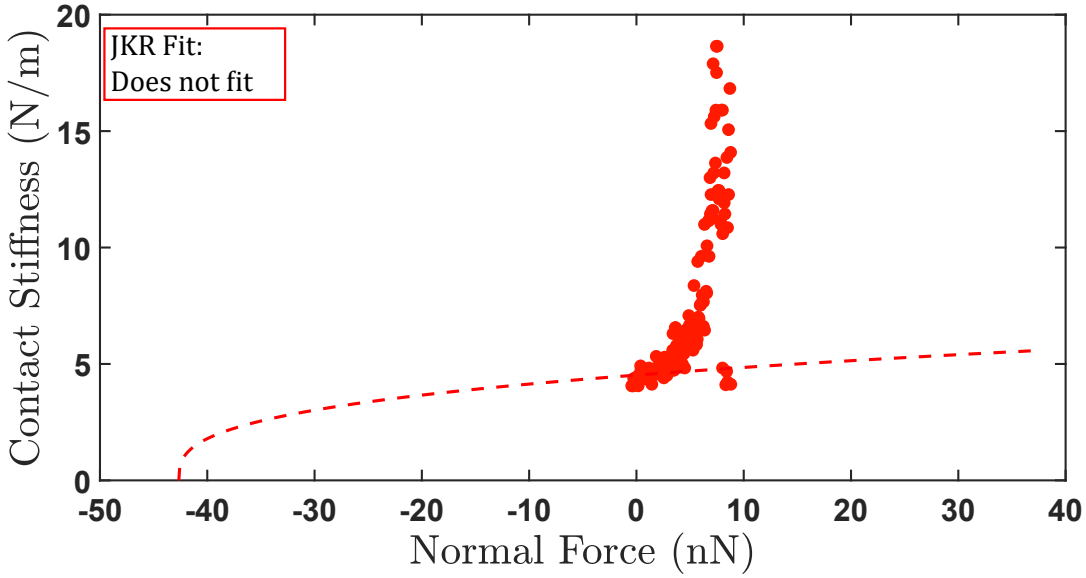


Figure 7.6: Contact mechanics fitting results for a test using a Borosilicate glass colloid probe on a HOPG sample.

This inability to fit is due to the contact stiffness values given from the cantilever dynamics approaching the upper limit of the model. This result is the same as the Diamond-on-Silicon test (Figure 7.2) with the corresponding high-frequency values in Figure 6.5. Although this issue was only found for very stiff contacts for the colloid tests, this result is very common. The likely result of this is added the mass of the colloid and glue forcing the cantilever to behave differently from the theoretical models, where the tip is assumed to be massless. A correction factor can be applied to correct for the stiffness of the cantilever but to address the dynamics of added mass to the cantilever the model described by Mahdavi [54] must be introduced [58]. As mentioned above, this more comprehensive model was not included in this study, but in future work it would be necessary.

A general summary in Table 7.1 presents the results in a variety of tests. As mentioned in Chapter 2.4 Tabor parameter values less than 0.5 favour the DMT model, while values above 5 favour the JKR model. Intermediate values generally favour the JKR model since the scaling of the Tabor model follows a logarithmic distribution (see Figure 2.12).

Table 7.1: Summary table of tip radius estimates from contact mechanics fitting. *NA* indicates the fitting did not converge or the fit was very poor.

Probe Material	Sample Material	Radius Estimate	Tabor Parameter
Silicon	HOPG	0.00132 ± 0.00002 nm	0.4567
Diamond	Silicon	NA	0.16
Glass Colloid	HOPG	NA	7.1923
Steel Colloid	Silicon	NA	1.8955
Silicon	PEO	8.21 ± 3.66 nm	3.1962
Silicon	PDMS	0.6033 ± 0.1300 nm	283.961

Tip-Sample Indentation

In addition to the estimate of the radius of the cantilever tip using the cantilever dynamics method, a second method was also used to compare and contrast the results. This method involves measuring the normal force (F_N) as the tip of the cantilever pushes into the surface.

Figure 7.7 shows the fitting result for a test using a silicon contact probe on a HOPG sample surface. The fitting result, although generally a poor fit, turned out to be ($R = 4.33 \pm 0.02 p\,m$), which is a major underestimation of the radius of the tip. This result is similar to the radius estimates from the cantilever dynamics method, but in both cases the estimated radius is far too small. Other radius estimates are shown in Table 7.2.

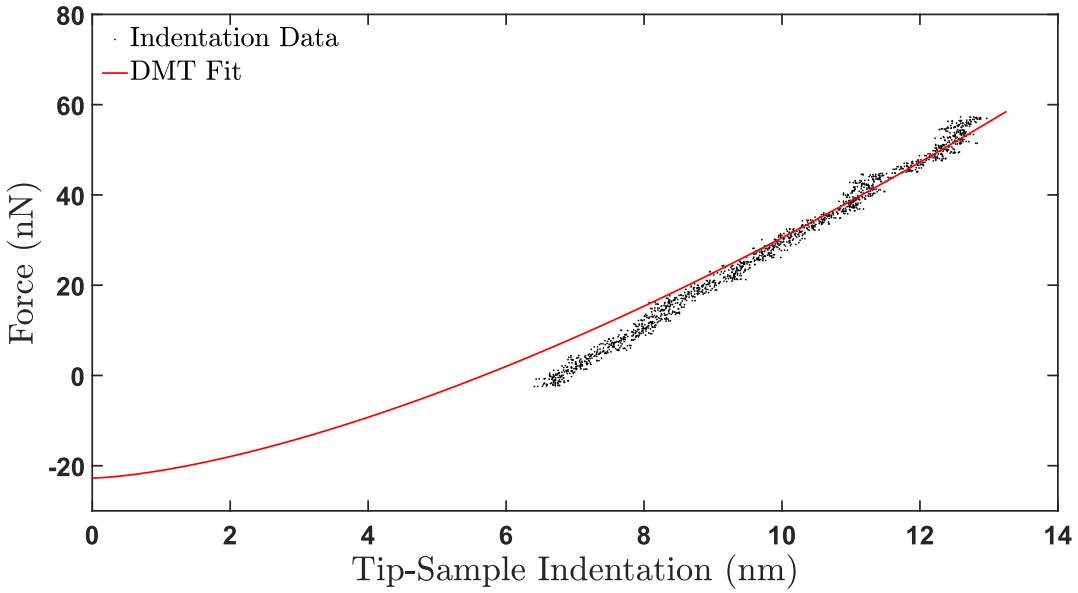


Figure 7.7: Fitting Result from force (F_N) vs sample indentation (D) using the DMT contact mechanics model. Fitting results in a tip radius estimate of ($R \approx 4.33 \pm 0.02\ p\,m$). Test was conducted using a Silicon contact probe on a freshly cleaved HOPG sample at standard atmospheric conditions.

Another indentation test conducted was done on the same PEO sample used in the force spectroscopy experiments. In this case, due to the greater indentation and from the soft sample, the JKR fit was much better, with the radius estimated being higher, despite still being too small.

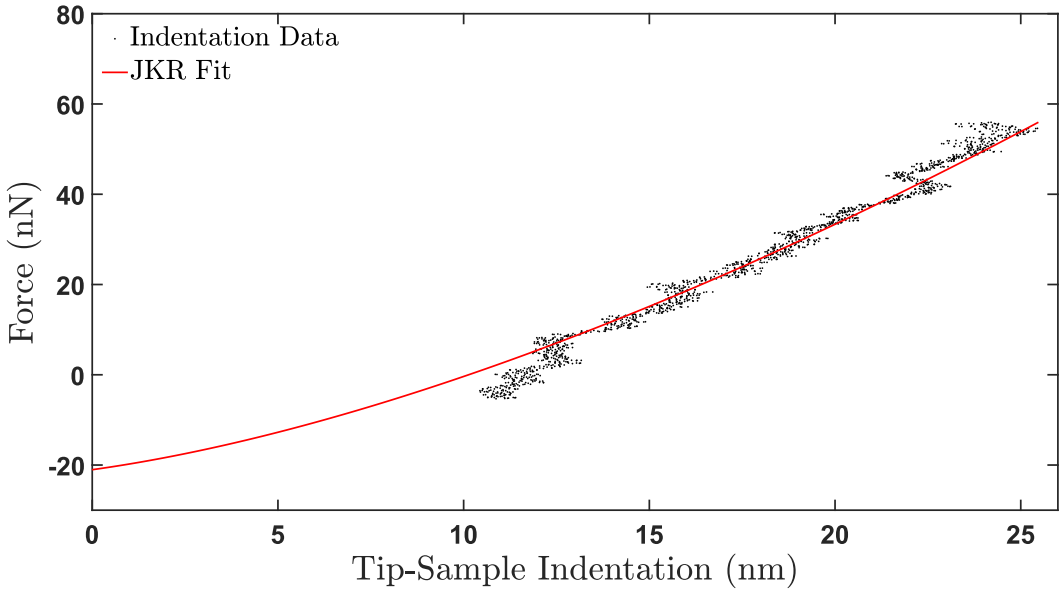


Figure 7.8: Fitting Result from force (F_N) vs sample indentation (D) using the JKR contact mechanics model. Fitting results in a tip radius estimate of ($R \approx 47.6 \pm 0.3\ pm$). Test was conducted using a Silicon contact probe on a PEO sample at standard atmospheric conditions.

Table 7.2: Summary table showing cantilever radii estimates from the tip-sample indentation tests.

Material	Jump-to-Contact	Pull-Off
HOPG	4.33 ± 0.02 pm	14.03 ± 0.2 pm
PEO	47.6 ± 0.3 pm	54.4 ± 0.4 pm
Silicon	0.1080 ± 0.0004 pm	0.198 ± 0.002 pm

These results indicate that the contact mechanics models are breaking down at this level and something unforeseen is taking place in the models. In these tests, the Young's modulus is assumed to be constant, but in other research conducted, this is not always true, and the Young modulus can vary [21].

As can be seen in the fit curves the indentation data do not exactly follow scaling of the DMT and JKR models and instead are more linear. One change to the contact models aiming to better capture this linear relationship is the move from a spherical indenter shape to a flat punch. As discussed in Chapter 2.4, when the indenter is a flat circular punch, the contact area does not change at very small deformations, resulting in a linear model (Equation 2.28) [22]. When fitting the data to this flat-punch case, the resulting tip-radius estimates better approaches the actual tip radii. This is shown for the HOPG sample (Figure 7.9) and the PEO polymer sample (Figure 7.10).

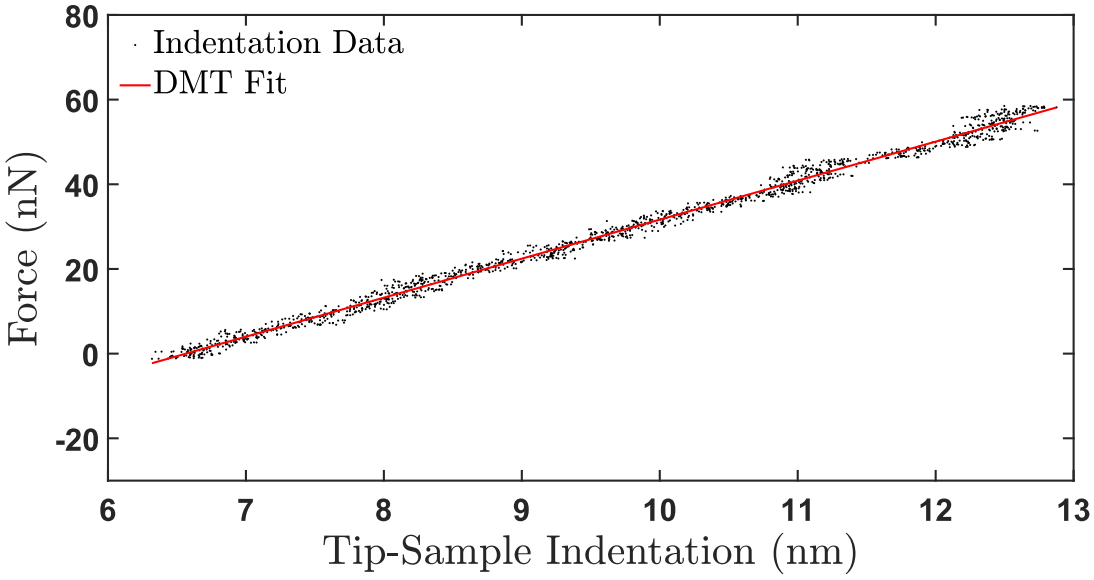


Figure 7.9: Fitting Result from force (F_N) vs sample indentation (D) using the flat punch contact model. Fitting results in a tip radius estimate of ($R \approx 0.210 \pm 0.001\ nm$). Test was conducted using a Silicon contact probe on a freshly cleaved HOPG sample at standard atmospheric conditions.

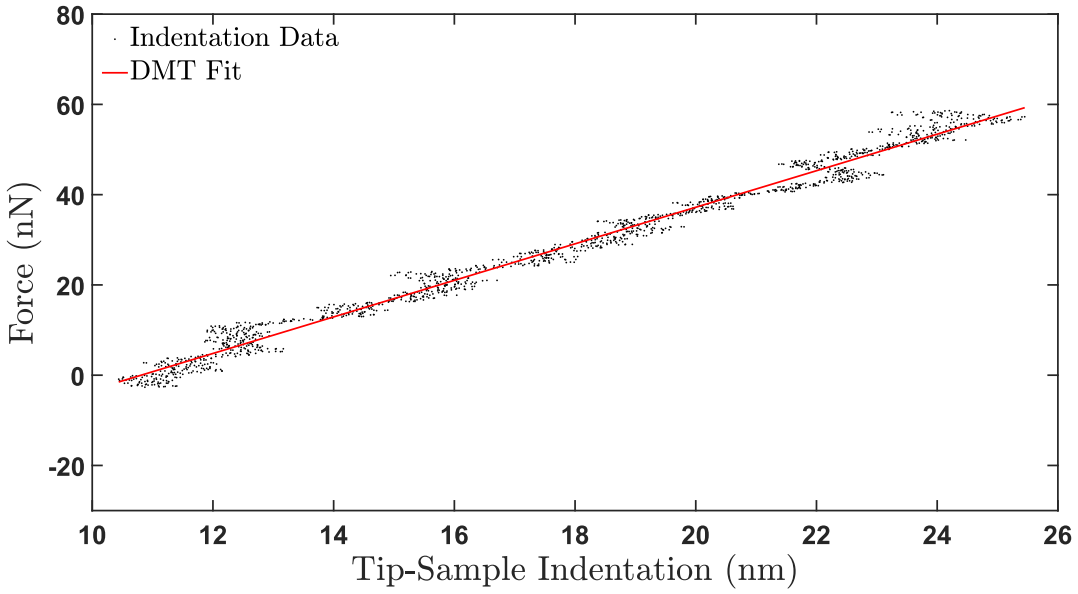


Figure 7.10: Fitting Result from force (F_N) vs sample indentation (D) using the flat punch contact model. Fitting results in a tip radius estimate of ($R \approx 6.75 \pm 0.04\ nm$). Test was conducted using a Silicon contact probe on a PEO sample at standard atmospheric conditions.

Table 7.3: Summary table showing cantilever radii estimates from the tip-sample indentation tests for the flat punch assumption.

Material	Jump-to-Contact	Pull-Off
HOPG	0.210 ± 0.001 nm	0.1903 ± 0.0004 nm
PEO	6.75 ± 0.04 nm	5.45 ± 0.03 nm
Silicon	0.0177 ± 0.0009 nm	0.0163 ± 0.0009 nm

The other parameter determined from the indentation of the sample is the contact stiffness, which is calculated from the change in normal force given a change in indentation (Equation 7.1). Contact stiffness estimates for the tests conducted take the simple linear relationship between force and indentation, although the instantaneous change can also be used to calculate the stiffness.

$$k^* = \frac{\Delta F}{\Delta D} \tag{7.1}$$

The contact stiffness estimates from indentation tests are shown below in Table 7.4

Table 7.4: Contact stiffness estimates from the tip-sample indentation tests. Values found from indentation are consistently higher than those from the cantilever dynamics estimates, although only slightly.

Material	Jump-to-Contact	Pull-Off
HOPG	8.976 ± 0.019 (N/m)	8.358 ± 0.01 (N/m)
PEO	4.165 ± 0.013 (N/m)	2.939 ± 0.011 (N/m)
Silicon	5.678 ± 0.017 (N/m)	5.30 ± 0.015 (N/m)

As seen in Table 7.4 the contact stiffness estimates are all in the range from 1-10 (N/m), with the jump-to-contact estimates always being slightly larger than the pull-off. When comparing the indentation contact stiffness estimates to those from the cantilever dynamics models, it can be seen that some results align while others do not. The HOPG results in Figure 7.1 have contact stiffness values ranging from 4-6 (N/m) while the indentation tests have a higher contact stiffness of 8-9 (N/m). Although the indentation tests have a higher contact stiffness, this may be a result of the indentation test recording over a larger range of force values. A result from high-speed recording means that the external data logger system cannot capture the entire force distance curve, whereas for the indentation tests the AFM internal data logger records the entire curve.

7.2 Cantilever Probe Verification

When force spectroscopy experiments were conducted, several special probes were utilised, colloid probes being one such example. A colloid probe is a special case where a cantilever without a tip has a small colloid particle glued to the end. Several sizes ($5-40\ \mu m$) and compositions (Borosilicate glass, Copper, Alumina, etc.) were tested. The major effect of adding the colloid particles was the extra mass at the end of the cantilever. This extra mass resulted in a lower resonant frequency and a greatly increased quality factor when out of contact. However, when the colloid probe came into contact, both the frequency and the quality factor showed a very large drop.

Probe Imaging

In order to verify the accuracy of the contact resonance calculations, the colloid probe tips needed to be imaged precisely. Two different methods were utilised to image the colloid probes in order to check both the size of the colloid probe and any imperfections on the surface of the colloid. The two methods used are scanning electron microscopy (SEM) and reverse tip AFM imaging using the TGT1 calibration grating made by TipsNano [59].

Scanning Electron Microscopy

The primary verification method used is the scanning electron microscope (SEM), which is the standard method of directly measuring the tip size of the cantilever probe. This was carried out to compare the estimated radius of the cantilever tip with the measured value in the SEM.

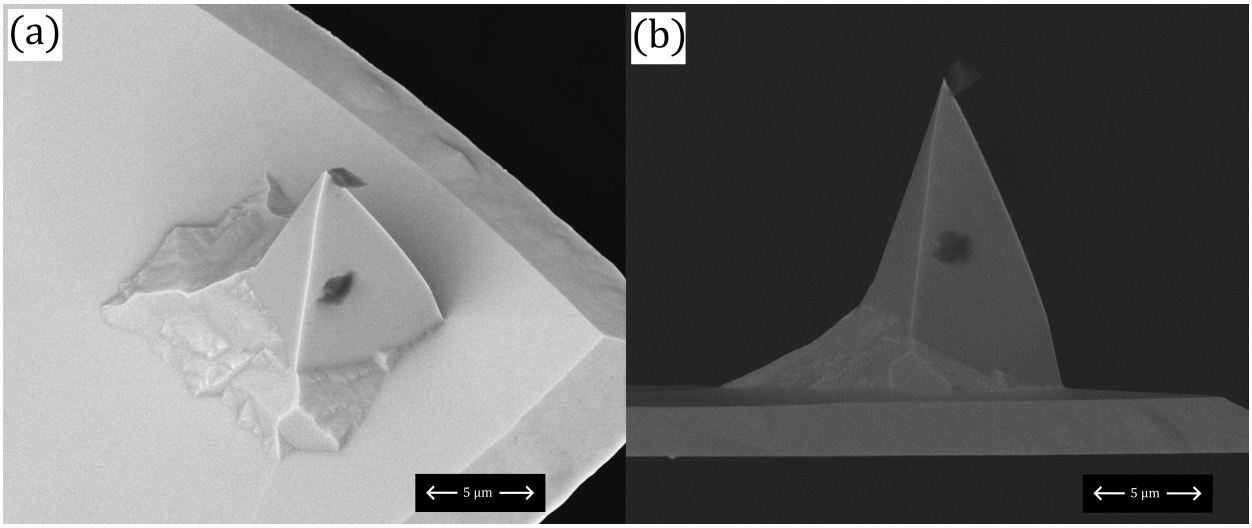


Figure 7.11: Scanning Electron Microscope (SEM) images of a Platinum coated Silicon contact probe. This probe along with other contact probes was utilised for the force spectroscopy experiments. The radii of the tip for these contact probes are in the range of $(5-25\ nm)$ depending on the use of the tip. (a) shows a top view, while (b) is a side view used to calculate the radius.

The SEM has the benefits of high resolution, direct measurement from multiple views, and being able to image the entire cantilever, not only the tip.

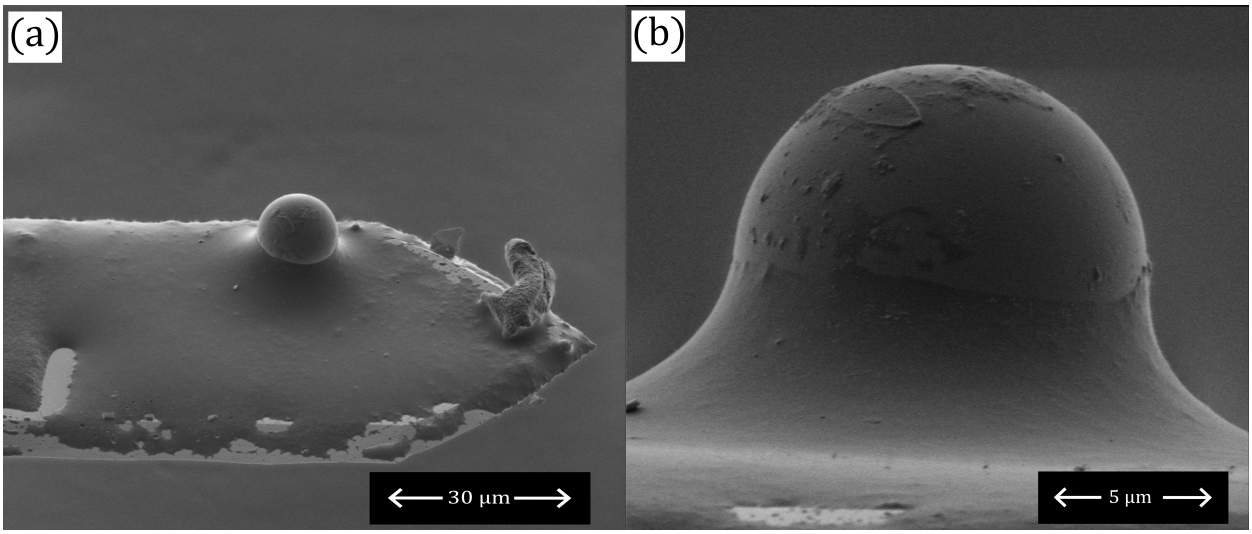


Figure 7.12: Scanning Electron Microscope (SEM) images of a Borosilicate Glass colloid probe. Note that the colloid is the large spherical object, while the grey material surrounding it is excess glue from its application. This colloid probe has a radius of ($\approx 9\ \mu m$), and many of the other glass colloids used are close in size to this one shown. (a) is a top view of the colloid, and (b) is a side view.

Reverse Tip Imaging

The TipsNano TGT1 test grating consists of a series of sharp AFM cantilever tips on a silicon substrate (Figure 7.13). By moving the colloid probe over the grating, contact with the reverse cantilever tips gives an image of the portion of the colloid probe in contact with the inverse tips.

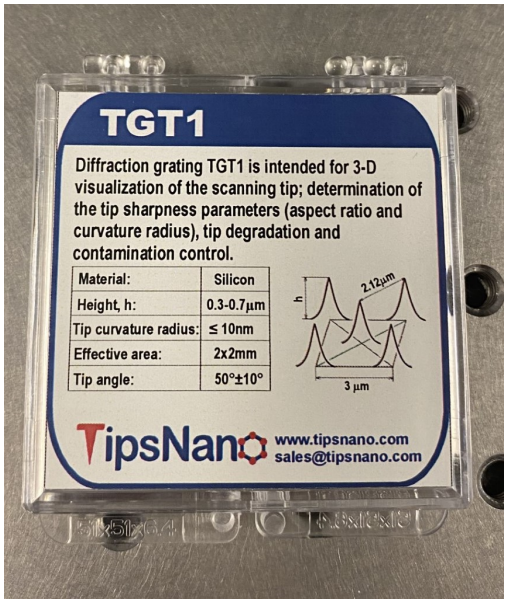


Figure 7.13: Calibration grating TGT1 from TipsNano. Spacing of tips is 2.12 μm diagonally and 3.0 μm laterally.

From this reverse image of the cantilever (Figure 7.14) height profiles are extracted which can then

be used to determine the radius of curvature of the colloid probe. This is done by measuring the height (h) and width (w) of the height profile of the colloid and using Equation 7.2 [60].

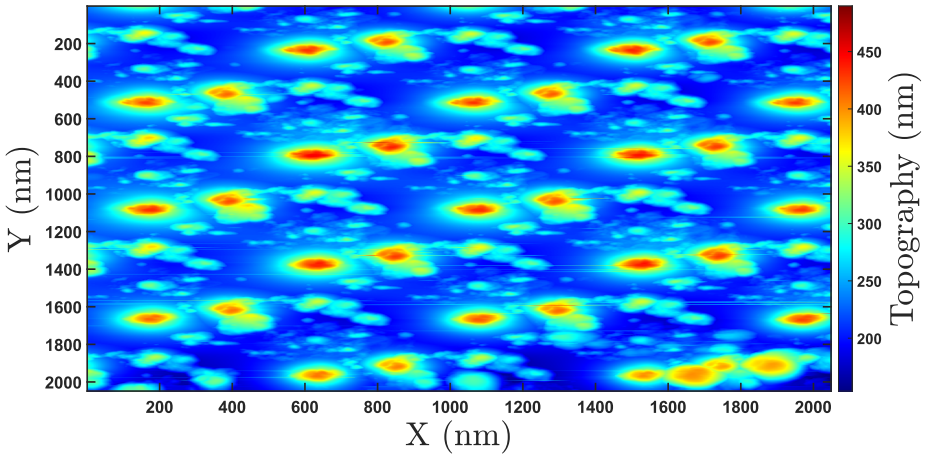


Figure 7.14: Topography scan of a Borosilicate glass colloid probe on the TGT1 calibration grating.

$$R = \frac{h^2 + (w/2)^2}{2h} \tag{7.2}$$

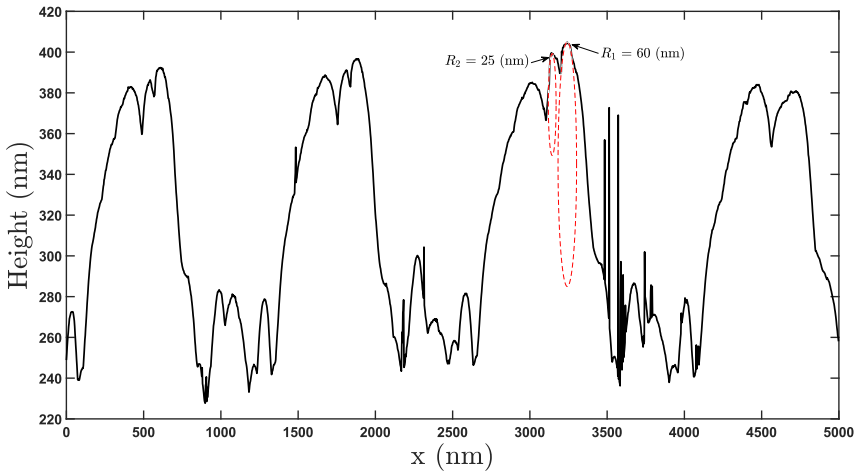


Figure 7.15: Average row height profiles from the scan shown in Figure 7.14.

Using Equation 7.2 one can determine not only the overall size of the colloid but also the size of any defects on the contact surface. The radius value does vary somewhat over the scan on the diffraction grating, so the values are averaged across the scan. The two verification methods gave matching results for the bulk colloid radius ($R \approx 9\,\mu m$) however, the reverse image was found to give more precise results in the contact area itself, as can be seen in Figure 7.15. The small peaks of ($25-60\,nm$) are the main contact points, which are what the contact mechanics models attempt to fit.

As can be seen in the reverse imaging scan (Figure 7.14) and the SEM image (Figure 7.12), the colloid probe (the bright repeating regions) is covered by a lot of excess glue which complicates the way the colloid contacts the surface. Many of these small pieces of glue end up being the material in contact, meaning that the results of the tip radius estimation gives not the overall size of the colloid, but instead the small imperfections of the surface that make contact first.

7.3 Summary

This final analysis phase, which focuses on the fitting of contact mechanics, shows some existing constraints in the current methodology and models used. Principally, the computed radii are consistently underestimated, or in certain cases, the results are altogether unattainable. The performance of the fitting procedure varies with the stiffness of the sample, with softer samples generally producing superior results. However, these also tend to undervalue the tip radius. Furthermore, any inaccuracies or discrepancies originating from the preceding cantilever dynamics procedures are propagated, becoming more noticeable when the contact stiffness values deviate significantly. This reveals the intertwined nature of these analysis steps, underscoring the need for precision and accuracy at each step.

Chapter 8

Conclusions and Future Work

On the basis of the findings and experimentation presented in this thesis, numerous possibilities can be explored in order to enhance the existing procedure and more effectively accomplish the objectives of using contact resonance to directly ascertain the physical and mechanical properties within the contact. Consistent with the results discussed above, the conclusions and prospects for future work can be categorised into the three distinct sections of the analysis along with the experimental design.

8.1 Spectral Analysis

In the spectral analysis section, distinct results emerged, each contributing to a deeper understanding of the contact resonance procedure. First, the previous work on using the Short-Time Fourier Transform (STFT) to fit peaks during the contact phase of the force-distance curve was successfully validated, aligning with previous findings. However, it became evident that the STFT's time windowing feature limited access to the transient behaviour observed in the Jump-to-Contact phase.

To address this limitation, the wavelet transform was introduced, providing an enhanced time resolution in the signal. However, this improvement came at the expense of frequency resolution and fitting accuracy for the cantilever's first resonance mode. Consequently, the wavelet transform was not included in the final analysis. Nevertheless, it showed potential at higher frequencies, where the resolution reached a finer level and proved more useful.

Although the continuous wavelet transform (CWT) demonstrated high accuracy in determining frequency, its computational requirements restricted its application to very small data sets. On the contrary, the STFT successfully processed larger time series, allowing a broader view of the force-distance curve and yielding valuable insights.

Looking ahead, one of the promising future directions in the spectral analysis is to extend the STFT analysis to cover the entire force-distance curve, rather than focusing on just a few seconds, as was done in this study. Overcoming hardware limitations to record the complete sweep, which may span several minutes, would allow for a comprehensive analysis of the frequency shift throughout the entire process. This expanded data set would enhance the accuracy of estimating the changing contact stiffness, leading to increased confidence in the final estimates.

Additionally, longer recordings would offer a unique opportunity to delve deeper into the higher modes of oscillation. By leveraging increased time averaging, a more precise investigation could be conducted, enabling better fitting of the peaks associated with these higher modes.

8.2 Cantilever Dynamics

The results obtained from the different cantilever models in the context of cantilever dynamics indicate a significant improvement in contact stiffness estimates when incorporating parameters such as tip position, cantilever tilt, and lateral forces. These enhanced models outperform the basic models by showcasing a notable increase in accuracy and reliability.

However, incorporation of damping to account for viscoelastic effects introduces additional challenges. Fitting the quality factor becomes less reliable compared to fitting the frequency, leading to increased error in the estimation process. It is crucial to acknowledge this limitation and its potential impact on the accuracy of the contact stiffness estimates derived from the cantilever dynamics models.

Moreover, it is observed that in very stiff contacts, when the frequency shift approaches the limit of the model (referred to as the pinned condition), the contact stiffness diverges. Even minor frequency shifts can cause the contact stiffness estimates to diverge to infinity, rendering subsequent contact mechanics fitting useless. This sensitivity is compounded by the increasing order power law scaling of the cantilever models, amplifying the sensitivity to frequency changes. Consequently, errors in frequency fitting result in a greater variability of contact stiffness values.

To address this issue, future work in cantilever dynamics analysis could explore averaging the frequency shifts over multiple force spectroscopy sweeps. By considering trends across multiple tests, this approach aims to mitigate the impact of individual test variability, thus improving the accuracy and robustness of the contact stiffness estimates derived from the cantilever dynamics models.

Furthermore, future work in this procedure could focus on incorporating more recent and comprehensive models, such as the one proposed by Malegori [50]. These advanced models account for factors such as tip shape and mass distribution, which have been shown to have a significant influence on the accuracy of contact stiffness estimation. Furthermore, when dealing with very massive colloid probes, adjusting the models to account for their specific characteristics is necessary, as their behaviour deviates from the assumptions of the massless models considered in this thesis [58].

8.3 Contact Mechanics

The primary conclusion drawn from the contact mechanics section is the significant underestimation of the effective tip radius when in contact. This finding serves as an indicator of potential inaccuracies in other mechanical property estimations, such as the Young's modulus. In the estimation process, a trade-off is often made between accurately estimating the tip radius and other mechanical properties by assuming one term to be constant while fitting the other. Thus, the underestimation of the effective tip radius highlights the limitations of the continuum contact mechanics models used and raises concerns about the accuracy of related mechanical property estimates.

To improve the accuracy of mechanical property estimations, further exploration of alternative contact mechanics models is warranted. It should be noted that prior research has already observed the breakdown of contact mechanics at the nanoscale, emphasising the need for refined models and approaches. Although the intermediate model described by Tabor and Maugis presents a promising avenue, there is a broader scope for exploring numerical modelling techniques, such as finite element analysis and molecular dynamics simulations. These techniques provide a more comprehensive understanding of real-world contact scenarios and can help overcome the limitations of analytical continuum models.

Furthermore, connecting the estimation method used in indentation calculations with spectral analysis and contact resonance models offers a holistic approach to characterising the contact system. By integrating information from multiple sources, a more accurate estimation of mechanical properties, including the tip radius and the Young's modulus, can be achieved. This integrated approach recognises the interdependencies between these properties and provides a more comprehensive understanding of the material's behaviour.

It is crucial to note that the estimate of the radius of the tip is not an isolated aspect, but serves as a benchmark for the accuracy and reliability of other estimates of mechanical properties. Addressing the underestimation of the tip radius is a vital step towards refining the estimation of key mechanical properties such as the hardness or elastic modulus.

8.4 Experimental

Regarding the experimental materials used, further investigation is warranted on the array of cantilever probes, specifically focusing on the enhancement of shorter non-contact probes and a broader selection of colloid probes. During the initial project, these probes were considered, but a significant portion of the findings were omitted due to challenges such as fitting the resonance peaks for the short non-contact probes and determining the mass and position of the colloid on the cantilever. Addressing these issues will enhance the measurement range since stiffer cantilevers permit a substantially larger normal force during experimentation.

Furthermore, a comprehensive testing regime can be developed using samples of varying stiffness values. Selecting a polymer material with progressive increments in Young's moduli could provide improved resolution between samples. Previous tests showed large changes in sample moduli, but incorporating finer variations may allow exploration of the intermediate sections of the frequency-stiffness dispersion curve, thus expanding our understanding of material behaviour under different stress conditions.

For indentation calculations, an additional experimental comparison is proposed between sharp cantilever probes and blunt tips. Although direct measurements may not produce precise results, a comparative analysis could yield valuable data. This involves the use of colloid probes, where the probe size can be varied from a single micrometre to fifty micrometres. The potential implications of these comparisons could greatly contribute to the knowledge base of material science, providing insights into tip-sample interactions, and enhancing prediction models.

Potential challenges to these modifications include accurate control of the colloid probe size and obtaining reliable measurements of the Young's modulus of the polymer materials, especially with incremental variations. In addition, potential errors in indentation calculations may present an obstacle that requires meticulous verification processes. However, overcoming these challenges and advancing in this direction is expected to further the field of cantilever probe technology and applications, leading to more robust and precise scientific experiments and greater performance of complex engineering materials.

Bibliography

[1] G. Binnig, C. Gerber, E. Stoll, T. R. Albrecht, and C. F. Quate, "Atomic Resolution with Atomic Force Microscope," *EPL (Europhysics Letters)*, vol. 3, p. 1281, jun 1987.

[2] R. W. Carpick, D. F. Ogletree, and M. Salmeron, "A general equation for fitting contact area and friction vs load measurements," *Journal of colloid and interface science*, vol. 211, no. 2, pp. 395–400, 1999.

[3] D. C. Hurley and J. A. Turner, "Measurement of poisson's ratio with contact-resonance atomic force microscopy," *Journal of Applied Physics*, vol. 102, 2007.

[4] U. Rabe, K. Janser, and W. Arnold, "Vibrations of free and surface-coupled atomic force microscope cantilevers: Theory and experiment," *Review of Scientific Instruments*, vol. 67, p. 3281, 1996.

[5] D. C. Hurley, "Contact Resonance Force Microscopy Techniques for Nanomechanical Measurements," *Applied Scanning Probe Methods XI*, vol. XI, pp. 97–138, 2008.

[6] J. P. Killgore, D. G. Yablon, A. H. Tsou, A. Gannepalli, P. A. Yuya, J. A. Turner, R. Proksch, and D. C. Hurley, "Viscoelastic property mapping with contact resonance force microscopy," *Langmuir*, vol. 27, pp. 13983–13987, dec 2011.

[7] E. Meyer, "Atomic force microscopy," *Progress in surface science*, vol. 41, no. 1, pp. 3–49, 1992.

[8] B. Bhushan and H. Fuchs, *Atomic Force Acoustic Microscopy*. Springer, 2006.

[9] A. Gujrati, A. Sanner, S. R. Khanal, N. Moldovan, H. Zeng, L. Pastewka, and T. D. Jacobs, "Comprehensive topography characterization of polycrystalline diamond coatings," *Surface Topography: Metrology and Properties*, vol. 9, no. 1, p. 014003, 2021.

[10] J. Liu, J. K. Notbohm, R. W. Carpick, and K. T. Turner, "Method for characterizing nanoscale wear of atomic force microscope tips," *ACS nano*, vol. 4, no. 7, pp. 3763–3772, 2010.

[11] C. Ma, W. Wang, Y. Chen, W. Arnold, and J. Chu, "Depth-sensing using afm contact-resonance imaging and spectroscopy at the nanoscale," *Journal of Applied Physics*, vol. 126, no. 12, 2019.

[12] S. Benaglia, C. A. Amo, and R. Garcia, "Fast, quantitative and high resolution mapping of viscoelastic properties with bimodal afm," *Nanoscale*, vol. 11, no. 32, pp. 15289–15297, 2019.

[13] A. Gannepalli, D. Yablon, A. Tsou, and R. Proksch, "Mapping nanoscale elasticity and dissipation using dual frequency contact resonance afm," *Nanotechnology*, vol. 22, no. 35, p. 355705, 2011.

[14] R. Wagner, R. J. Moon, and A. Raman, "Mechanical properties of cellulose nanomaterials studied by contact resonance atomic force microscopy," *Cellulose*, vol. 23, pp. 1031–1041, 2016.

[15] A. Labuda, M. Lysy, W. Paul, Y. Miyahara, P. Grütter, R. Bennewitz, and M. Sutton, "Stochastic noise in atomic force microscopy," *Physical Review E*, vol. 86, no. 3, p. 031104, 2012.

[16] J. Drelich and K. L. Mittal, *Atomic force microscopy in adhesion studies*. CRC Press, 2005.

[17] E. M. Puchner and H. E. Gaub, "Force and function: probing proteins with afm-based force spectroscopy," *Current opinion in structural biology*, vol. 19, no. 5, pp. 605–614, 2009.

[18] J. Zlatanova, S. M. Lindsay, and S. H. Leuba, "Single molecule force spectroscopy in biology using the atomic force microscope," *Progress in biophysics and molecular biology*, vol. 74, no. 1-2, pp. 37–61, 2000.

[19] K. Mishra, L. K. Babu, and R. Singh, "Characterization of uv degraded carbon fiber-matrix interphase using afm indentation," pp. 175–178, 2018.

[20] J.-J. Wu, "The jump-to-contact distance in atomic force microscopy measurement," *The Journal of Adhesion*, vol. 86, no. 11, pp. 1071–1085, 2010.

[21] Y. Ding, J. Wang, G.-K. Xu, and G.-F. Wang, "Are elastic moduli of biological cells depth dependent or not? another explanation using a contact mechanics model with surface tension," *Soft Matter*, vol. 14, no. 36, pp. 7534–7541, 2018.

[22] G. Pharr, W. C. Oliver, and F. Brotzen, "On the generality of the relationship among contact stiffness, contact area, and elastic modulus during indentation," *Journal of materials research*, vol. 7, no. 3, pp. 613–617, 1992.

[23] Y. Javadi and J. M. Fernandez, "Atomic Force Spectroscopy," *Encyclopedia of Biophysics*, pp. 116–122, 2013.

[24] J. L. Hutter and J. Bechhoefer, "Calibration of atomic-force microscope tips," *Review of Scientific Instruments*, vol. 64, pp. 1868–1873, 1993.

[25] J. E. Sader, "Frequency response of cantilever beams immersed in viscous fluids with applications to the atomic force microscope," *Journal of Applied Physics*, vol. 84, pp. 64–76, 7 1998.

[26] J. E. Sader, J. W. M. Chon, and P. Mulvaney, "Calibration of rectangular atomic force microscope cantilevers," 1999.

[27] T. Albrecht, S. Akamine, T. Carver, and C. Quate, "Microfabrication of cantilever styli for the atomic force microscope," *Journal of Vacuum Science & Technology A: Vacuum, Surfaces, and Films*, vol. 8, no. 4, pp. 3386–3396, 1990.

[28] A. Labuda, "Daniell method for power spectral density estimation in atomic force microscopy," *Review of Scientific Instruments*, vol. 87, no. 3, p. 033704, 2016.

[29] D. Cole and R. Clark, "Fluid-structure interaction in atomic force microscope cantilever dynamics and thermal response," *Journal of applied physics*, vol. 101, no. 3, p. 034303, 2007.

[30] T. D. Jacobs, C. M. Mate, K. T. Turner, and R. W. Carpick, *Understanding the tip-sample contact: An overview of contact mechanics from the macro- to the nanoscale*. wiley, 11 2013.

[31] H. Hertz, "The contact of elastic solids," *J Reine Angew, Math*, vol. 92, pp. 156–171, 1881.

[32] B. V. Derjaguin, V. M. Muller, and Y. P. Toporov, "Effect of contact deformations on the adhesion of particles," *Journal of Colloid and interface science*, vol. 53, no. 2, pp. 314–326, 1975.

[33] D. TABOR, *Surface Forces and Surface Interactions*. Elsevier, 1977.

[34] D. Maugis, "Adhesion of spheres: the jkr-dmt transition using a dugdale model," *Journal of colloid and interface science*, vol. 150, no. 1, pp. 243–269, 1992.

[35] I. N. Sneddon, "The relation between load and penetration in the axisymmetric boussinesq problem for a punch of arbitrary profile," *International journal of engineering science*, vol. 3, no. 1, pp. 47–57, 1965.

[36] W. C. Oliver and G. M. Pharr, "Measurement of hardness and elastic modulus by instrumented indentation: Advances in understanding and refinements to methodology," *Journal of materials research*, vol. 19, no. 1, pp. 3–20, 2004.

[37] H.-J. Butt, "Measuring electrostatic, van der waals, and hydration forces in electrolyte solutions with an atomic force microscope," *Biophysical journal*, vol. 60, no. 6, pp. 1438–1444, 1991.

[38] W. A. Ducker, T. J. Senden, and R. M. Pashley, "Direct measurement of colloidal forces using an atomic force microscope," *Nature*, vol. 353, no. 6341, pp. 239–241, 1991.

[39] M. Kappl and H.-J. Butt, "The colloidal probe technique and its application to adhesion force measurements," *Particle & Particle Systems Characterization: Measurement and Description of Particle Properties and Behavior in Powders and Other Disperse Systems*, vol. 19, no. 3, pp. 129–143, 2002.

[40] J. Colchero, M. Cuenca, J. G. Martínez, J. Abad, B. P. García, E. Palacios-Lidón, and J. Abellán, "Thermal frequency noise in dynamic scanning force microscopy," *Journal of Applied Physics*, vol. 109, no. 2, p. 024310, 2011.

[41] I. Grattan-Guinness, "Joseph fourier, théorie analytique de la chaleur (1822)," in *Landmark Writings in Western Mathematics 1640-1940*, pp. 354–365, Elsevier, 2005.

[42] M. T. Heideman, D. H. Johnson, and C. S. Burrus, "Gauss and the history of the fast fourier transform," *Archive for history of exact sciences*, pp. 265–277, 1985.

[43] M. Dct, "Wavelet Theory and Application," *Wavelet Theory and Application*, 1993.

[44] A. V. Oppenheim, *Discrete-time signal processing*. Pearson Education India, 1999.

[45] V. Pukhova, F. Banfi, and G. Ferrini, "Transient eigenmodes analysis of single-impact cantilever dynamics combining Fourier and wavelet transforms," *Nanotechnology*, vol. 26, no. 17, pp. 1–10, 2015.

[46] P. Klapetek and I. Oldidal, "Applications of the wavelet transform in afm data analysis," *Acta Physica Slovaca*, vol. 55, no. 3, pp. 295–303, 2005.

[47] M. R. Portnoff, "Time-Frequency Representation of . Digital Signals," *IEEE Transactions on Acoustics, Speech and Signal Processing ASSP*, vol. 28, no. 1, pp. 55–69, 1980.

[48] O. Rioul and M. Vetterli, "Wavelets and Signal Processing," *IEEE Signal Processing Magazine*, vol. 8, no. 4, pp. 14–38, 1991.

[49] Y. Deng, C. Wang, L. Chai, and Z. Zhang, "Determination of Gabor wavelet shaping factor for accurate phase retrieval with wavelet-transform," *Applied Physics B: Lasers and Optics*, vol. 81, no. 8, pp. 1107–1111, 2005.

[50] G. Malegori and G. Ferrini, "Tip-sample interactions on graphite studied using the wavelet transform," *Beilstein Journal of Nanotechnology*, vol. 1, no. 1, pp. 172–181, 2010.

[51] C. Truesdell, "The rational mechanics of flexible or elastic bodies: 1638-1788," *Leonhardi Euleri Opera Omnia, Ser. 2*, 1960.

[52] P. A. Yuya, D. C. Hurley, and J. A. Turner, "Relationship between Q-factor and sample damping for contact resonance atomic force microscope measurement of viscoelastic properties," *Journal of Applied Physics*, vol. 109, no. 11, 2011.

[53] J. A. Turner, S. Hirsekorn, U. Rabe, and W. Arnold, "High-frequency response of atomic-force microscope cantilevers," *Journal of Applied Physics*, vol. 82, no. 3, pp. 966–979, 1997.

[54] M. H. Mahdavi, A. Farshidianfar, M. Tahani, S. Mahdavi, and H. Dalir, "A more comprehensive modeling of atomic force microscope cantilever," *Ultramicroscopy*, vol. 109, no. 1, pp. 54–60, 2008.

[55] J. W. Suk, S. R. Na, R. J. Stromberg, D. Stauffer, J. Lee, R. S. Ruoff, and K. M. Liechti, "Probing the adhesion interactions of graphene on silicon oxide by nanoindentation," *Carbon*, vol. 103, pp. 63–72, 2016.

[56] R. Suriano, C. Credi, M. Levi, and S. Turri, "Afm nanoscale indentation in air of polymeric and hybrid materials with highly different stiffness," *Applied surface science*, vol. 311, pp. 558–566, 2014.

[57] C. Torrence and G. P. Compo, "A Practical Guide to Wavelet Analysis," *Bulletin of the American Meteorological Society*, vol. 79, no. 1, pp. 61–78, 1998.

[58] M. Chighizola, L. Puricelli, L. Bellon, and A. Podestà, "Large colloidal probes for atomic force microscopy: Fabrication and calibration issues," *Journal of Molecular Recognition*, vol. 34, no. 1, p. e2879, 2021.

[59] "TGT1 Calibration Grating." "https://tipsnano.com/catalog/calibration/tgt1/".

[60] C. Neto and V. S. Craig, "Colloid probe characterization: Radius and roughness determination," *Langmuir*, vol. 17, pp. 2097–2099, 4 2001.

Appendix

CR-AFM Reference Method

The current CR-AFM technique is to calibrate the system using a reference sample with known properties, specifically the Young's modulus (E^*_{ref}). By then testing with the same cantilever probe on a test sample the ratio of the two samples contact stiffness values allows for the estimation of the test samples Young's modulus (E^*_{test}) (Equation 1) [6]. These contact stiffness values are calculated from the analytical cantilever models discussed in Chapter 3.2.

$$E^* = E^*_{ref} = E^*_{ref}\left(\frac{k^*_{test}}{k^*_{ref}}\right)^m \tag{1}$$

Indentation and Flat Punch Model

The applications of the flat punch case are in nanoindentation experiments where a Berkovich identer is commonly pressed into the sample surface. These nanoindenters can achieve forces much larger than those of a given AFM probe resulting in indentation values in the micrometre range [36]. Equation 2.27 is then applied to the slope of the unloading portion of the indentation curve to determine the mechanical properties of the sample as seen in figure 1.

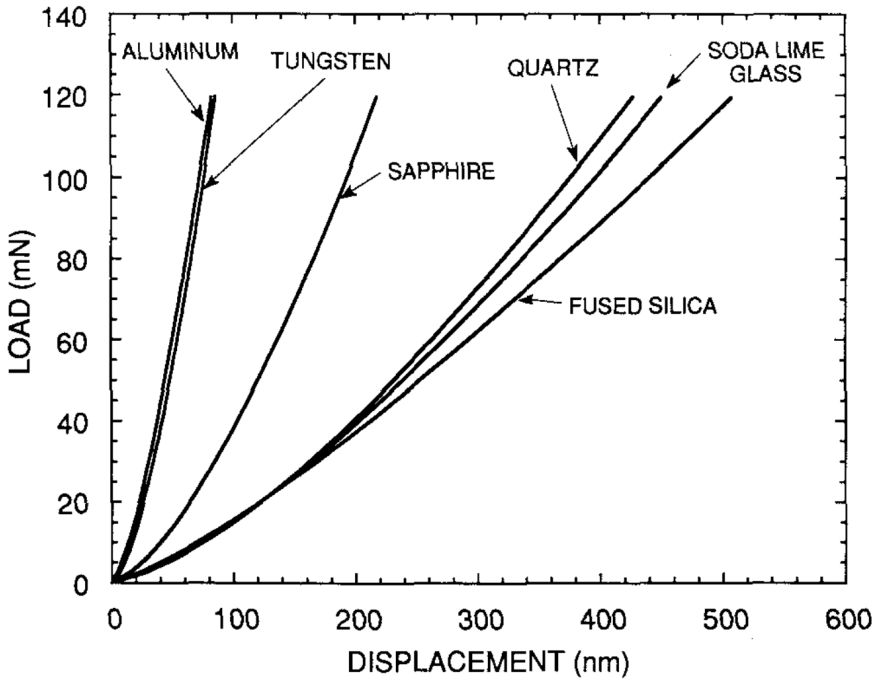


Figure 1: Elastic unloading curves for several materials obtained in nanoindentation experiments with a Berkovich indenter plotted on linear axes with displacements shifted to a common origin. From Oliver and Pharr [36]

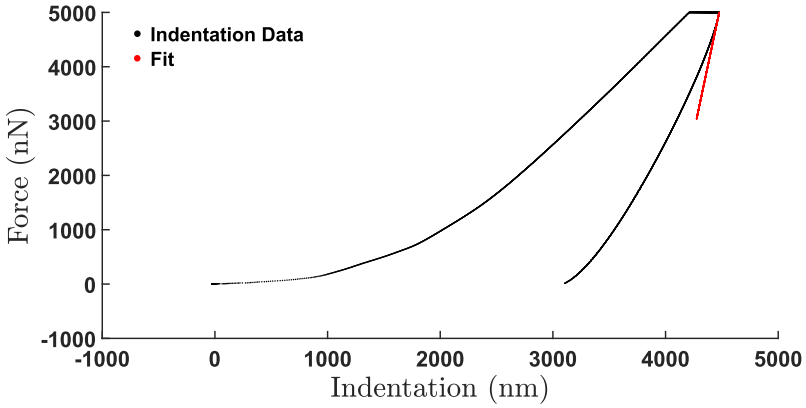


Figure 2: Example Elastic unloading curves for the PEO sample obtained from nanoindentation experiments with a Berkovich indenter. Slope of curve in red is the linear fit used to determine the Young's modulus of the sample from equation 2.28.

Table 1: Summary table of Young's modulus calculations for the PDMS sample. The table shows the max force (F_{max}), indentation (D_{max}) and calculated Young's modulus. The mean Young's modulus was determined to be $0.025 \pm 0.002\ GPa$.

$F_{max}\ (nN)$	$D_{max}\ (nm)$	Young's Modulus (GPa)
4999.23415	4475.872681	0.0279568704374955
4999.029217	4700.856503	0.0249700954199971
4973.315016	5182.045563	0.0228406330429461
4999.402312	3927.239944	0.0319513504102104
4999.531197	4742.582371	0.0257200448571903
4999.393564	4841.493	0.0242662502264934
4994.998312	5232.55674	0.0222540406494333
4999.037748	5059.120262	0.0229475587611845
4999.176877	4235.515565	0.0291741595285398
4999.572559	4567.090563	0.0267328452472476
4999.148232	4903.686774	0.0238693434851094
4999.021779	4903.755965	0.0237059055009386
4999.404217	4988.094705	0.0230140411638618
4951.697296	5176.002587	0.0237172076395190
4999.015157	4311.431835	0.0291063408968211
4999.413141	4863.607088	0.0244330138496768
4999.256194	4973.859163	0.0234436299679544
4999.280155	4600.026782	0.0255285675627537
4999.614213	4847.333029	0.0247637722325296
4998.866111	4739.091539	0.0248186217792158
4999.071425	4944.087781	0.0235790335932099
4999.340128	4820.333979	0.0246151800623741

Table 2: Summary table of Young's modulus calculations for the PEO sample. The table shows the max force (F_{max}), indentation (D_{max}) and calculated Young's modulus. The mean Young's modulus was determined to be $0.22 \pm 0.03\ GPa$.

$F_{max}\ (nN)$	$D_{max}\ (nm)$	Young's Modulus (GPa)
4999.898524	5198.221473	0.204567684192819
4999.121015	4579.246705	0.263221098262001
4999.591057	5119.692616	0.211774174256549
4999.050672	4172.278919	0.265872479891373
4999.782607	5173.711066	0.200591560279923
4994.880335	5158.694254	0.203257562682396